



HAL
open science

Debonding mechanisms of soft adhesives : toward adhesives with a gradient in viscoelasticity

Francois Tanguy

► **To cite this version:**

Francois Tanguy. Debonding mechanisms of soft adhesives : toward adhesives with a gradient in viscoelasticity. Polymers. Université Pierre et Marie Curie - Paris VI, 2014. English. NNT : 2014PA066079 . tel-01021169

HAL Id: tel-01021169

<https://theses.hal.science/tel-01021169v1>

Submitted on 9 Jul 2014

HAL is a multi-disciplinary open access archive for the deposit and dissemination of scientific research documents, whether they are published or not. The documents may come from teaching and research institutions in France or abroad, or from public or private research centers.

L'archive ouverte pluridisciplinaire **HAL**, est destinée au dépôt et à la diffusion de documents scientifiques de niveau recherche, publiés ou non, émanant des établissements d'enseignement et de recherche français ou étrangers, des laboratoires publics ou privés.

THESE DE DOCTORAT DE
L'UNIVERSITE PIERRE ET MARIE CURIE

Spécialité

Chimie et Physico-Chimie des Polymères
(ED 397, Physique et Chimie des Matériaux)

Présentée par

M. François TANGUY

Pour obtenir le grade de

DOCTEUR DE L'UNIVERSITE PIERRE ET MARIE CURIE

Sujet de la thèse :

**Debonding Mechanisms of Soft Adhesives: Toward
Adhesives with a Gradient in Viscoelasticity**

Soutenance prévue le 02 Juin 2014 devant le jury composé de :

M. Frédéric Restagno	Chargé de Recherches, Université d'Orsay	Rapporteur
M. Loïc Vanel	Professeur, Université Claude Bernard Lyon-1	Rapporteur
M. Laurent Corté	Chargé de Recherches, Ecole des Mines ParisTech	Examineur
M. Alain Fradet	Professeur, UPMC	Examineur
M. Norbert Willenbacher	Professeur, Institut de Technologie de Karlsruhe	Examineur
M. Costantino Creton	Directeur de Recherche CNRS, ESPCI ParisTech	Directeur de thèse
Mme Anke Lindner	Professeur, Université Diderot Paris 7-ESPCI ParisTech	Encadrante de thèse

List of abbreviations

AA	Acrylic acid
AFM	Atomic force microscope or microscopy
BA	Butyl Acrylate
CTA	Chain Transfer Agent
GPC	Gel Permeation Chromatography
M_n	Number Average Molar Mass
M_w	Weight Average Molar Mass
NMR	Nuclear magnetic resonance
PAM	Poly(acrylamide)
PDI	Polydispersity index
PDMS	Poly(dimethylsiloxane)
PE	Polyethylene
Poly(BA-co-AA)	Poly(butyl acrylate – co – acrylic acid)
PSA	Pressure-Sensitive Adhesive
PSTC	Pressure Sensitive Tape Council
PTT	Phant-Thien and Tanner
SAOS	Small Amplitude Oscillatory Shear
SFA	Surface force apparatus
SS	Stainless Steel
THF	Tetrahydrofuran
UCM	Upper-Convected Maxwell
VOC	Volatile Organic Component

Table des matières

General Introduction	1
1 State Of The Art	5
1.1 Adhesion and Adhesives	6
1.1.1 Adhesion	6
1.1.2 Pressure-sensitive Adhesives (PSAs)	7
1.2 Acrylic Polymers as PSAs	9
1.2.1 Synthesis of acrylic polymers by free radical polymerization	9
1.2.2 Film formation	17
1.3 Mechanical characterization and properties of PSAs	18
1.3.1 Linear Viscoelastic properties	19
1.3.2 Non-linear viscoelastic properties	21
1.4 Adhesive characterization and debonding mechanisms of PSA	28
1.4.1 Characterisation of adhesive properties of PSA	28
1.4.2 Debonding mechanisms	31
1.4.3 Limits of actual PSA systems	35
1.5 Modeling elastic solids, viscous fluids and viscoelastic materials	36
1.5.1 Elastic solids and elastomers	38
1.5.2 Viscous fluids	42
1.5.3 Viscoelasticity	44
2 Acrylic polymers as model materials	55
2.1 Introduction	57
2.2 Specifications of the model materials	57
2.3 Characterization of the polymers synthesized	59
2.3.1 Molecular weight and gel content	59
2.3.2 Architecture characterization	61
2.4 Mechanical characterization	62
2.4.1 Sample preparation	62
2.4.2 Linear viscoelastic characterization	62
2.4.3 Characterization of the non-linear properties	63
2.5 Adhesive Characterization	65
2.5.1 Sample preparation	65
2.5.2 Probe-tack test	66

2.6	Results and Discussions	69
2.6.1	Mechanical characterization	69
2.6.2	Adhesion characterization and debonding mechanisms	74
2.7	Conclusion	81
3	Analysis of the growth of cavities at the interface	85
3.1	Introduction	87
3.2	High resolution observation and numerical analysis	88
3.2.1	Probe-Tack tests coupled with microscope	88
3.2.2	Image Analysis	89
3.3	Material Properties	91
3.3.1	Mechanical properties	91
3.3.2	Adhesion properties	92
3.4	Analysis of the debonding structure	94
3.4.1	Evolution of the load-bearing area	94
3.4.2	Projected shape of cavities	97
3.4.3	Growth rate of individual cavities	97
3.4.4	Effective Normal Stress	100
3.4.5	Effective elongation	102
3.4.6	Effective stress versus effective elongation curves	103
3.5	Conclusions	104
4	Modeling viscoelastic materials used as PSAs	109
4.1	Introduction	111
4.2	Experimental section	111
4.3	Modeling uniaxial deformation of PSAs : choice of a convenient model	113
4.3.1	Choice of a convenient model for PSAs under uniaxial deformation	113
4.4	The PTT Model : Mathematical aspects	115
4.4.1	Application of the PTT model to the uniaxial flow	115
4.4.2	Asymptotic behavior	116
4.4.3	PTT model under constant $\dot{\epsilon}_H$ or varying $\dot{\epsilon}_H$	120
4.4.4	Influence of the parameters on the PTT Model	120
4.5	2-modes PTT model	123
4.5.1	Fitting strategy	124
4.5.2	Results and discussion	124
4.6	Prediction of the adhesive/cohesive debonding transition of PSAs	127
4.7	Conclusion	130
5	Multi-layer adhesives	133
5.1	Introduction	135
5.2	Making multi-layer adhesives	136
5.3	Experimental Techniques	137
5.3.1	Probe-tack Test	137
5.3.2	Shear test	137

5.4	Results and Discussions	137
5.4.1	Multi-layer materials on low adhesion surface	137
5.4.2	Multi-layer materials on high adhesion surface	140
5.4.3	Comparison with blend systems	142
5.4.4	Effect of the thickness of the layers	144
5.4.5	Shear properties	145
5.5	Conclusion	146
6	PSAs with a continuous gradient	149
6.1	Introduction	151
6.2	Preparation of Solvent-based model acrylic polymers	151
6.2.1	Synthesis	151
6.2.2	Chemical Characterization	154
6.3	Characterization of uncross-linked and cross-linked networks	156
6.3.1	Corss-linking reaction	156
6.3.2	Mechanical characterization	158
6.3.3	Adhesive properties	160
6.4	Making films with a continuous gradient in viscoelastic properties	161
6.4.1	Modus operandi to obtain films with continuous gradients	162
6.5	Adhesive properties of a films with a continuous gradient in vis- coelastic properties	163
6.6	Diffusion theory applied to our system	167
6.7	Conclusion	169
7	General Conclusion and Outlook	173
	General Conclusion and Outlook	173

General Introduction

The Pressure Sensitive Adhesives (PSAs) are thin films that adhere to a substrate by applying a light pressure and that can ideally be detached from the substrate without any residue. These adhesives have an important place in our daily life, as we find them in adhesive tapes, self-adhesive labels, bandages or in the famous Post It[®]. The adhesion properties are generated by van der Waals interactions at the interface coupled with a maximal dissipation of energy of the material under deformation. In order to create enough adhesion at the interface while dissipating maximal energy, soft viscoelastic solids are used : viscoelasticity is needed to relax stresses, create easily a molecular contact and dissipate energy upon debonding and a non zero elastic modulus at $t = \infty$ is needed to resist shear forces over long times. This combination of apparently incompatible properties should be especially fine tuned when the adhesive is applied on rough surfaces and low energy surfaces. Moreover, the mechanisms occurring during the debonding of a PSA are very complex and heterogeneous : two main mechanisms compete with each other : propagation of cavities along the interface as cracks (normal to the pulling direction) and the bulk expansion of the same cavities parallel to the pulling direction. This competition dictates the performances of the adhesive, but the two mechanisms do not occur in the same location (one at the interface, the other in the bulk). It is therefore reasonable to think that a homogeneous layer of adhesive is not the best solution to reach the combination of macroscopic properties that are needed.

There are several ways to introduce heterogeneities in an adhesive. It can be done at the level of the polymer structure (block copolymers) at the particle structure (films made from latex particles) and at the layer structure (multi-layer structures). In this work, we explore a different strategy, which is to create a 1-D gradient in viscoelastic properties along the thickness of the adhesive layer. We will show that it is possible to find a way to optimize a PSA and especially control the debonding mechanism, depending on the targeted substrate, by using such structured materials. Two approaches will be studied : one by making multi-layer adhesives, and the other by introducing a continuous gradient along the thickness of the adhesive. Carelli et al. led in 2007 preliminary studies that showed the potential interest of bi-layer systems, but the complexity of the materials used limited the understanding of the phenomena in play

The adhesives studied in this thesis are acrylic adhesives made from butyl acrylate and acrylic acid. The composition was selected to obtain a model system

simple enough to model and to relate its properties with its structure, while being a realistic model of industrial PSAs. The synthesis was carried out by emulsion polymerization, leading to particles dispersed in water, or by solution polymerization in an organic solvent. Films of adhesives were obtained by drying the solution, leading to films with a thickness from 25 to 150 μm . Materials were characterized in the linear regime by standard small angle oscillatory shear rheology, and at large deformation by tensile tests and extensional rheology. The adhesive properties were studied in details using probe-tack test devices.

Soft viscoelastic materials used as PSAs show a complex mechanical behavior that is not easy to model, especially because of their strong rate dependence when they are uncross-linked or weakly cross-linked. Recently, Deplace et al. developed in 2009 a simple model coupling a nonlinear viscoelastic model with a hyperelastic model containing the effect of the finite extensibility of the chains. This model could fit uniaxial deformation for differently cross-linked PSAs, but was not robust when strain rate was changed. More robust models have been developed, especially in the Computational Fluid Dynamics field, to simulate complex flows and departure from linear viscoelastic behavior. Nevertheless, these models require numerous parameters that are correlated in a complex way to the polymer architecture and are of limited help to synthetic chemists trying to optimize a material. Conversely, hyperelastic models catch well the strong strain hardening at large strain that is observed in crosslinked PSA but do not predict any strain rate dependence.

In this thesis, we will show that it is possible to apply the viscoelastic model of Phan-Thien and Tanner to PSA and fit the behavior of model PSAs over a range of strain rate in uniaxial deformation. The parameters extracted from the fit have a physical meaning and will be linked to the adhesive properties of our materials.

This work was included in a European Union project MODIFY (Multi-scale modelling of interfacial phenomena in acrylic adhesives undergoing deformation) to understand the role of internal, external interfaces and gradient of properties in the debonding process by a multi-scale approach. This project gathered five universities, University of Patras (Greece), Ecole Polytechnique (France), UCL (Belgium), ETH-Zurich (Switzerland) and ESPCI (France), as well as two industrial partners, LyondellBasell Industries and DOW Chemical Company. The skills of the participating teams range from synthesis and characterization of complex systems to the modeling by macroscopic finite-element or phase-field calculations. The team of Ralph Even from DOW Chemical Company synthesized a family of model polymers that will be described in detail in Chapter 2 and will be used in Chapter 3, 4 and 5. We collaborated with UCL (with Lalaso Mohite, Dietmar Auhl and Prof. Christian Bailly) and DOW Chemical Company (with Isabelle Uhl) for the characterization of these acrylic adhesives. A close collaboration was also put in place with Matteo Nicoli from Ecole Polytechnique to develop a strong numerical analysis of probe-tack experiments discussed in Chapter 3. We also collaborated with Matteo Nicoli and with Vlasis Mavrantzas from University of Patras to develop a model to fit the uniaxial behavior of our materials which will be discussed in Chapter 4.

This manuscript is divided into six chapters. The first one is devoted to important background information on the physics and chemistry of pressure sensitive adhesives as well as models used to fit viscoelastic materials. The second chapter is dedicated to the mechanical and adhesive characterization of the model materials synthesized by DOW Chemical Company. The purpose is to show the large range of properties offered by the materials at our disposal especially in terms of debonding mechanisms. A comparison between two uniaxial tests at large deformation, tensile test and extensional rheology, further used in this thesis, is also presented. The third chapter presents probe-tack experiments synchronized with high capabilities in image analysis to obtain quantitative measurements of the growth dynamics of cavities, including the total projected area, the average cavity shape and their growth rate on three different viscoelastic materials. These materials give access to a corrected true stress and strain which can then be quantitatively compared with material properties in uniaxial extension.

In Chapter 4, we present a two-mode model derived from the Phan-Thien and Tanner model for uniaxial deformation. A discussion on the mathematical aspects of this model is carried out. Then this model is used to fit experimental data of tensile tests and extensional rheology. Finally, the model is used to simulate tensile tests over a range of strain rates and predict from these simulations how the transition between adhesive and cohesive debonding changes with material and strain rate.

In Chapter 5, we focus on the strategy to make PSA adhesive layers with a gradient in viscoelastic properties along their thickness by studying in a systematic way multi-layer adhesives and show how this strategy can be adapted to low or high energy surfaces to obtain better adhesive performances.

In Chapter 6, an innovative way to make adhesives with a continuous gradient in viscoelastic properties by using the diffusion of a cross-linker is presented. The synthesis of the polymer in solution and the characterization of homogeneously cross-linked materials obtained from these dried polymers is presented first, and then the methodology to obtain adhesive layers with a continuous gradient of crosslinking along their thickness is described and the properties of the films are investigated. Finally, the main contributions of this work are summarized in a conclusion along with outlooks.

Chapitre 1

State Of The Art

1.1 Adhesion and Adhesives

1.1.1 Adhesion

The science of adhesion is the study of interactions between two different surfaces, of the energy needed to separate both surfaces and of the deformation mechanisms occurring during the separation. We only consider solid materials, since liquid materials refer to wetting studies and gases to adsorption/desorption processes.

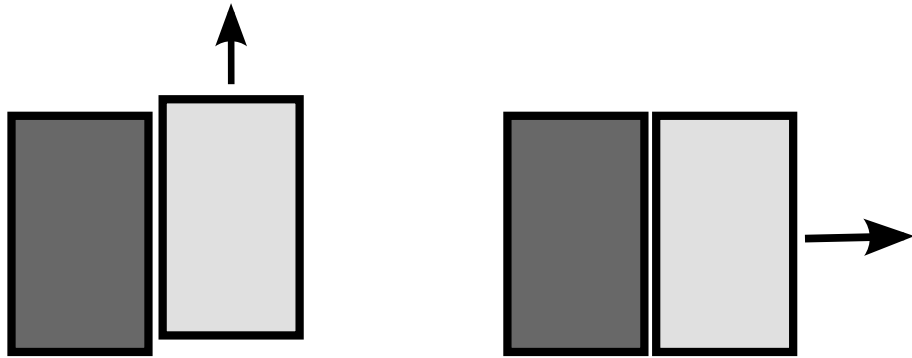


FIGURE 1.1 – Representation of an adhesion test, pulling either in the parallel direction of the interface or perpendicular to the interface.

An adhesion test consists of separating two materials and measuring the force applied and the work performed to obtain this process. It can be summarized by figure 1.1. Usually, a force or a displacement is applied in a parallel or perpendicular direction to the contact plane, until separation.

A first approach to study these mechanisms is to examine the interactions between the molecules of the two materials, responsible of cohesion of condensed matter. These interactions can be described by the potential energy between two molecules of the different materials. All intermolecular interactions behave in the same qualitative way, described by the curve drawn in Fig. 1.2. They lead to repulsive forces for very short intermolecular distances and attractive forces at longer distances, with an equilibrium at an intermediate distance. The most common interactions between two materials are the van der Waals interactions, which exist between all materials. These interactions are relatively weak, a few kJ/mol when compared with covalent bonds ($\approx 300kJ/mol$ for a C-C bond).

A simple model to study adhesion is the case of two undeformable materials. In that case, the process is reversible and the mechanical energy needed to break the interface is directly obtained by the thermodynamic work of adhesion given by :

$$W_{th} = \gamma_1 + \gamma_2 - \gamma_{12} \quad (1.1)$$

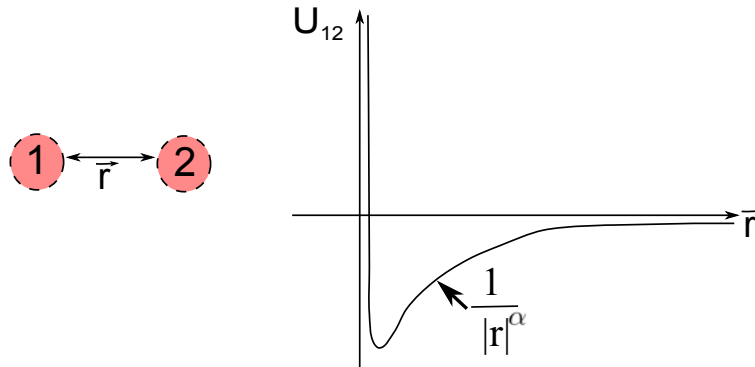


FIGURE 1.2 – interfacial forces energy between a particle 1 and 2. α depends on the interaction considered

where γ_1 and γ_2 are the surface tensions between the materials and the air and γ_{12} the surface tension of the interface 1-2. The higher the interaction between 1 and 2, the higher γ_{12} .

Eq. (1.1) does not usually represent the actual work done to separate two surfaces in practice, in particular for viscoelastic materials, which can deform a lot and dissipate much energy during the debonding.

Due to the surface roughness of most hard and solid materials, the effective contact area between two solids is low and leads to a low adhesion energy. One way to reach good adhesion between two surfaces is to introduce a soft material between them that will establish a molecular contact on both sides. This type of material is called an adhesive. This material will need to show a maximal contact with both surfaces, create strong interactions, dissipate energy upon debonding and have enough cohesion not to break or flow too easily under deformation. While industrial adhesives reach adhesion energy of $\approx 100 - 1000 \text{ kJ/mol}$, adhesion energy between a hard substrate and a soft elastic material reach only $\approx 0.1 \text{ J/m}^2$ up to 1 J/m^2 in case of strong molecular interactions. To attain these high values, dissipation phenomena are needed to consume energy during the debonding. Well chosen polymers can be used as good adhesives, as they are known to dissipate energy due to the entangled network that constitutes the material while showing good cohesion.

1.1.2 Pressure-sensitive Adhesives (PSAs)

Definition

Pressure-sensitive adhesives (PSAs) is the usual denomination of self-adhesive materials. They are designed to stick on almost any surface by simple contact under light pressure during a short time. Contrary to other adhesives, adhesion is reached without any physical transformation or chemical reaction during the

bonding process (Creton, 2003). Usually, no residue is left on the surface after debonding.

First developments of PSAs were aimed at medical and first aids applications in the middle of the nineteenth century. Applications in the automobile sector appeared at the beginning of the 1920s with masking tape for the automotive aftermarket with crimped paper as the backing. This started the development of saturated paper tapes which became the most important tape category (Satas, 1989). Among the industrial leaders in this area, we can cite 3M, Cytec, Dow Adhesives (formerly Rohm& Haas), Henkel and Tesa.

PSA are soft viscoelastic solids that obtain their unique properties simply from the fact that the energy gained in forming the interactions is way lower than the energy dissipated during the fracture of these same bonds. For short contact times, the only interface forces active in PSA adhesion are Van der Waals forces (Creton, 2003). Other interactions (hydrogen or electrostatic bondings especially) can take place for longer contact times and enhance the adhesion.

Specifications

PSAs are characterized by their properties in tack, peel and resistance to shear at long times (the way to measure these properties will be described in section 1.4). Viscoelastic materials are needed since viscosity leads to dissipation while elasticity enhances the resistance to shear. More specifically, PSAs must be based on polymers well above their glass transition temperature T_g . Typically, the usage temperature of a PSA should be 25-45°C above its T_g (Zosel, 1985) and its Young's modulus should be below 0.1 MPa (known as Dahlquist criterion, (Dahlquist, 1969)), thus being not too elastic to allow dissipation during the initial stage of the debonding (Creton, 2003). A fine tuning of the polymer network is needed to reach all these specifications.

A limited number of polymer classes can be used for PSA applications to fulfill these requirements. Among these, we can mention a few classes :

- Styrenic block copolymers, blend of triblocks (Styrene-Isoprene-Styrene, SIS) and diblocks (SI) or star-blocks mixed with a low molecular weight high Tg tackifying resin (Satas, 1989; Roos and Creton, 2005).
- Acrylic-based PSA (Satas, 1989; Tobing and Klein, 2001; Lindner et al., 2006; Deplace, 2008; Degrandi, 2009).
- Silicone adhesives, which can be useful at extreme temperatures or for reversible adhesion and biomedical applications (Nase et al., 2008).

Among these polymers, we will focus on acrylic adhesives, as they lead to interesting adhesive properties that can be easily tuned by cross-linking the system (Satas, 1989) and by varying the monomer composition or the molecular weight of the polymers used. Most of these polymers can be efficiently used without additives, contrary to SIS triblocks for example.

1.2 Acrylic Polymers as PSAs

Acrylic adhesives are usually composed of random copolymers. The main monomer typically has a long side-chain giving a homopolymer with a low T_g (typically butyl acrylate BA, 2 ethyl hexyl acrylate 2EHA or isooctyl acrylate IOA). A monomer offering a short side-chain can be added to adjust the T_g of the final copolymer (typically methyl methacrylate, MMA). Acrylic acid is added, as it has been shown that it improves cohesion and adhesion properties (Chan and Howard, 1978; Aubrey and Ginosatis, 1981; Gower and Shanks, 2004). Some typical monomer structures are represented in Fig. 1.3

One of the main advantages of acrylic PSAs is that they can be prepared by solution polymerization as well as by emulsion polymerization. We will discuss both synthesis methods and their respective advantages.

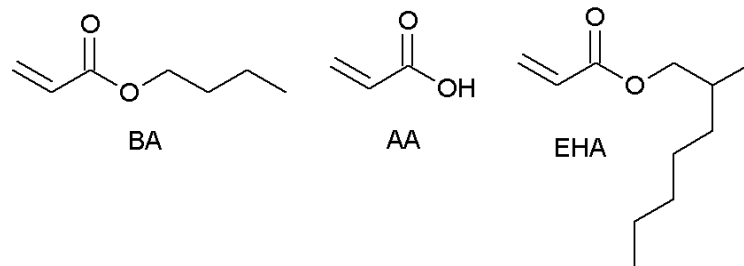
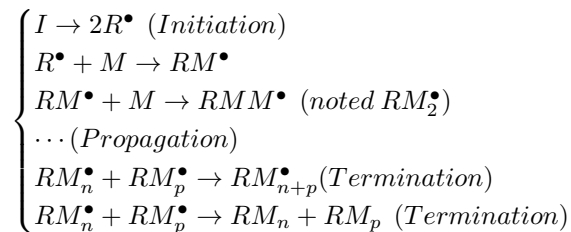


FIGURE 1.3 – Some classical acrylic monomers : Butyl Acrylate (BA), Acrylic Adid (AA) and 2 ethyl hexyl acrylate EHA

1.2.1 Synthesis of acrylic polymers by free radical polymerization

Acrylic polymers are usually synthesized by free radical polymerization. This way of synthesis is used by most of the high-volume production polymers, like polyethylene, polystyrene poly(vinyl chloride), poly(methyl methacrylate)... Free radical polymerization is based on a chain reaction process induced by a generation of radicals that will be regenerated until all the reactives are consumed. It can be separated in three main processes : initiation, propagation and termination. The process can be summarized as :



We will discuss the different steps in more details here.

Initiation

At first, generation of radicals is necessary to start the process. Different kinds of free radical initiators exist, such as peroxydes, hydroxoperoxydes, peresters and aliphatic azocompounds. Their common property is their ability to break a bond under a stimulus and break itself into two molecules bearing a radical, which will be stabilized by other chemical groups, usually by a mesomeric effect. The external stimulus can be UV or temperature. An example is given by the AIBN decomposition in Fig. 1.4. The radicals created are stabilized by the nitrile groups.

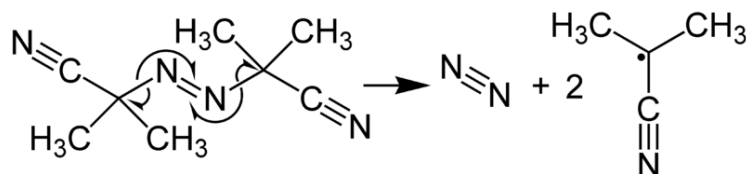


FIGURE 1.4 – Decomposition of AIBN to create free radicals. The reaction is activated by temperature.

Propagation

The radicals formed during initiation are highly reactive. Thus, they will react with active molecules around them, which, in the case of polymerization, will be monomers. For acrylic monomers, the radical will react with the vinyl group. The product will still be a radical, as shown on Fig. 1.5(a). This molecule will react with another monomer, setting up the process of propagation by adding more and more monomers.

The process is a bit more complex for copolymers, since two (or more) monomers will be in competition to react with the active radical (cf Fig. 1.5(b)). Depending on the respective activity of the monomers. The reactivity ratios characterize this competitive process, representing the reactivity of radicals ending with an A or B group with an A or B monomer. They are defined by :

$$r_A = \frac{k_{pAA}}{k_{pAB}} \quad (1.2)$$

$$r_B = \frac{k_{pBB}}{k_{pBA}} \quad (1.3)$$

where k_{pAB} is the kinetics constant of the propagation reaction from a chain ending with an A group on a B monomer. Depending on the values of these ratios, different types of copolymers are obtained :

- $r_A=r_B=0$: Monomers A prefer to react with B and monomers B prefer to react with A. If the same quantity of monomers is introduced, perfect alternating copolymers are obtained.

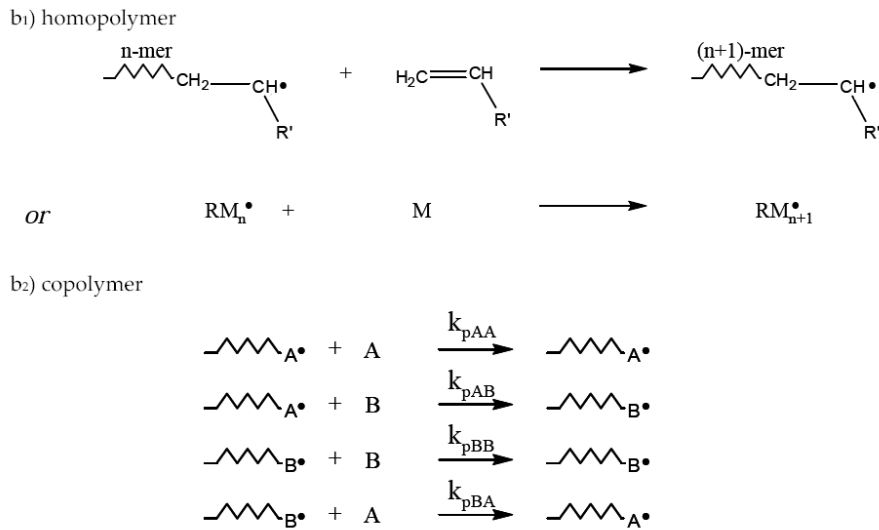


FIGURE 1.5 – Mechanism of propagation in radical chain polymerization.

- $r_A=r_B=\infty$: A prefers to react with A, B with B. Usually, homopolymers A and B will be formed in a mixture.
- $r_A=r_B=1$: The reactivity is perfectly equivalent. They are consumed randomly, leading to a random copolymer.
- $r_A<1$ and $r_B<1$ both polymers react together, creating imperfect alternating copolymers.
- $r_A \gg 1 \gg r_B$: In the beginning, a homopolymer A will be created. With the depletion of A, B will be more and more incorporated, creating a gradient in the composition of the chain, also called *composition drift* (Odian, 2004).

Termination

The longer the active chains, the harder it is for the radicals to react with monomers that will be less present around the active sites. Radicals can react with other radicals and kill the propagation process :

- By recombination : two active chains react together to create a longer dead chain.
- By disproportionation : a hydrogen atom is transferred from one chain to another, creating two dead chains, one bearing a double bond. These situations are summarized in Fig. 1.6

Branchings and cross-links formation

Free radicals, as they are very reactive, can transfer to other molecules present in the medium or move away from the end of the active chains. These

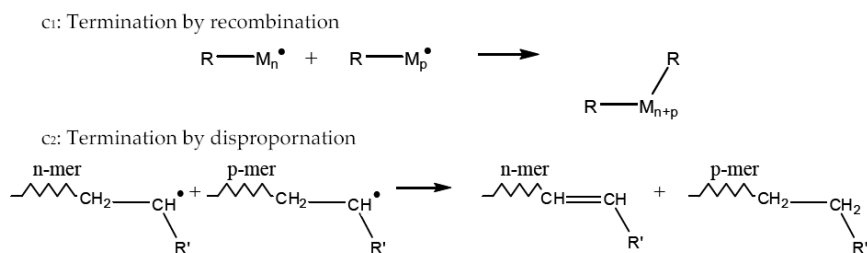


FIGURE 1.6 – Mechanisms of termination in radical chain polymerization.

transfer processes leads to a stop of the growth of the chain at its end, but can initiate a new monomer or a growing chain from the middle of a chain, leading to branchings. These transfers can either be intermolecular or intramolecular. Long or short branchings, respectively will be obtained. They are represented in Fig. 1.7 and 1.8.

Transfer processes strongly influence the length of the chains synthesized as a given initiator can produce several polymer molecules during its lifetime if transferred from one molecule to another. Specific chain transfer agents (CTA) can thus be used in order to initiate more chains and thus decrease and regulate the molecular weight.

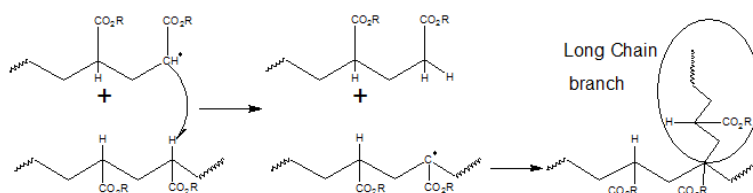


FIGURE 1.7 – Mechanisms of transfer reactions leading to a long chain branch.

The tendency to give rise to transfer reactions depends on the radicals of the monomers considered. The acrylate monomers are known to easily transfer and thus create highly branched systems. To avoid that, methacrylate monomers can be used as they do not offer a transfer site on the chain. However, poly(methyl methacrylate) is a glassy polymer that cannot be used for PSAs applications.

The transfer process is influenced by the concentration of polymers : under low concentration, propagation will less likely happen, leading to an increase in transfer.

In some cases, intermolecular chain transfer reactions can lead to long branches that will terminate with another active radical on a chain, creating a crosslinking point, even without any cross-linker added (see Fig. 1.9). This can lead to network structures that will be insoluble.

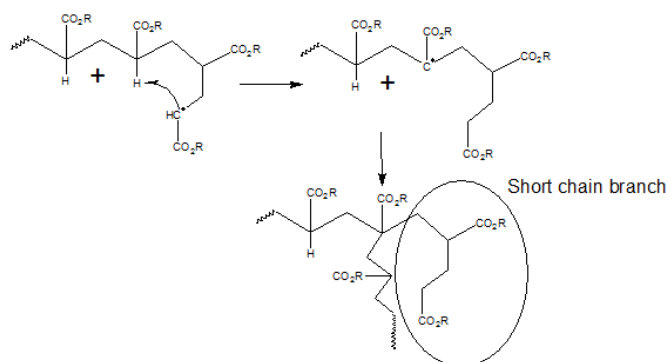


FIGURE 1.8 – Mechanism of transfer reaction leading to a short chain branch. The transfer is helped by a thermodynamically stable six member ring

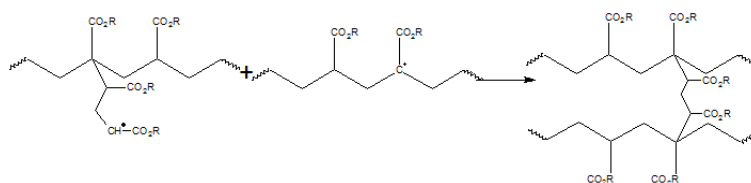


FIGURE 1.9 – Reaction between a growing branch and an activated chain to create partial networks

Free radical polymerization can be realized under different conditions : in bulk, in solution, in dispersion and in emulsion. We will focus on the solution and emulsion polymerization, mostly used for acrylate polymers and introduce these techniques by discussing the bulk polymerization.

Bulk polymerization

Bulk polymerization is the simplest technique since no solvent or dispersing agent is used : the pure monomer is the reacting medium. The initiator and the polymer synthesized must be soluble in the monomer. Organic peroxydes are usually chosen as the initiator. While this synthesis seems simple, it cannot reach a high degree of conversion (defined as the rate of monomers consumed) because of the gel effect, sometimes called *Trommsdorff effect*. This phenomenon consists in an auto-acceleration of the polymerization rate (which can lead to explosion), followed by a strong decrease of the process (See Fig. 1.10).

This process is due to two causes :

- High viscosity of the reacting phase due to the presence of chains of polymer creates a decrease in the termination rate. It leads to an increase in the free radicals concentration, increasing the polymerization rate and finally the temperature of the system as the polymerization reaction is

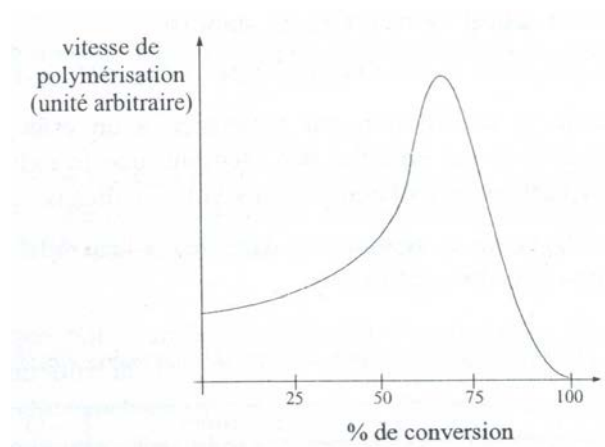


FIGURE 1.10 – Polymerization rate as a function of conversion rate in bulk polymerization.

highly exothermic.

- As the temperature increases, the decomposition of the initiator accelerates, creating more free radicals, also increasing the polymer rate.

Those two causes maintain and accelerate the polymerization process. The increase in viscosity creates strong difficulties in mixing the reacting medium and the evacuation of heat created, leading to a system out of control. Polymerization is stopped when the viscosity is so high that monomers cannot move any more in the reacting medium. Polymerization rate decreases dramatically, stopping the synthesis.

This technique is only used for photo-activated polymerizations, especially for thin film applications. In other situations, the gel effect will be avoided by different techniques. For the synthesis of PSAs, solution polymerization or emulsion polymerization are preferred.

Solution polymerization

This technique is often used in laboratories as it leads to high conversions without gel effect. The monomers and initiators are simply dissolved in a common solvent that will be able to dissolve the created polymer. For acrylate monomers, Toluene, Hexane, Cyclohexane, etc. can be chosen. It is important that the solvent does not react with the radicals in order to avoid transfer reactions between the active radicals and the solvent molecules.

The solvent dilutes the medium, which limits the increase of viscosity and plays the role of heat-transfer medium. Nevertheless, mixing issues can be encountered, as the viscosity starts at very low values ($\approx 1\text{cP}$) to gain several

orders of magnitude. High quantities of solvent can be used to limit the increase in viscosity but will cause the kinetics of the reaction to decrease. In order to get the pure polymer in the end of the reaction, high-temperature evaporation or precipitation in a non-solvent are used.

The advantages of this synthesis approach are that its implementation is quite easy and the system is easy to define, as only one phase constitutes the system. This is why this technique is mainly used in laboratories. However, the use of any volatile organic component (VOC), as solvents, is strongly limited in the European Union under the recent REACH regulation, limiting the application of this technique in industry. It can be used when high purity polymers are needed or when the solvent is water, as for polyacrylamide for example.

Emulsion polymerization

In most emulsion polymerizations, water is used as the dispersing medium, whereas the monomers and polymers are insoluble in it. This process is more environmental friendly as no VOCs are used. Latexes, *i.e.* solutions of polymer particles in water, are obtained, with a limited increase of viscosity during the synthesis. This allows the production of very long polymer chains without stirring issues. Moreover, the technique is very interesting as the low viscosity latexes obtained can be cast on substrates much faster than high viscosity solutions (Jovanovic and Dubé, 2004). For these reasons, acrylic adhesives synthesized by emulsion polymerization present a great interest in the field of PSA nowadays.

For this process, the mixture of insoluble monomers is dispersed in droplets stabilized by surfactants. The initiator has to be soluble in water : $S_2O_8K_2$, H_2O_2 or redox couples are mostly used. In most formulations, the amount of surfactants exceeds the amount needed to completely cover the droplets, leading to the formation of micelles in the water phase that are swollen by monomers. The growing chains will transform micelles into particles. The system is summarized in Fig. 1.11.

Conventional emulsion polymerization (the shorter term "emulsion polymerization" is preferred in the following) is based on free-radical polymerization. It is generally carried out in stirred tank reactors working in batch, semi-continuous or continuous modes. Smith and Ewart (1948) developed the first theory of emulsion polymerization and described it as a three-stage process. It is based on the following hypotheses :

- the initiation process takes place in the aqueous solution,
- the active oligomers, bearing radicals, enter inside the micelles and start the polymerization process there,
- the entrance of another radical in a particle results in a stop of the growth of the chain, due to termination of the two radicals.

Smith and Ewart described these three stages : particle nucleation, polymer particle growth and final stage, summarized in table 1.1.

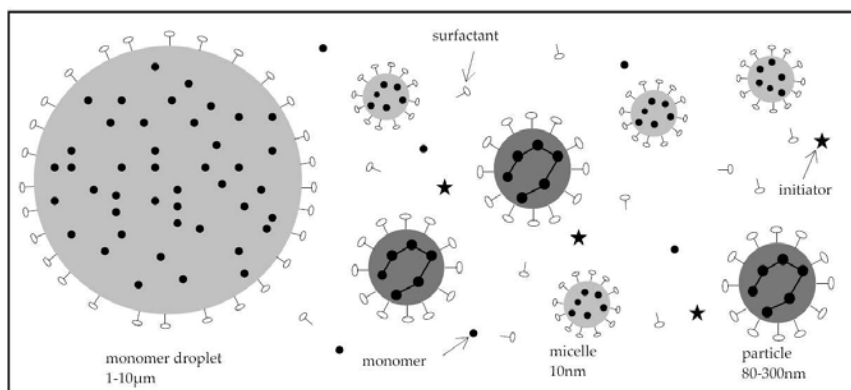


FIGURE 1.11 – Entities present in the reacting medium during an emulsion polymerization

Interval	Typical conv. range	Micelles	Monomer droplets	Particle number	Particle size
1	0-10%	Present	Present	Increases	Increases
2	10-40%	Absent	Present	Constant	Increases
3	40-100%	Absent	Absent	Constant	\approx Constant

TABLE 1.1 – Different intervals of an emulsion polymerization (Jovanovic and Dubé, 2004)

At the beginning, all the components are mixed together in the reactor. The organic phase contains monomers whereas the aqueous phase is made of deionized water and surfactant, stabilizing monomer droplets and forming micelles. Monomer droplets have an average size of 1-10 μm while micelles are much smaller (around 10 nm). The reaction starts with the formation of radicals in the aqueous phase from the initiator.

Particle nucleation refers to the initiation of polymerization and the appearance of the polymer chains. Due to the presence of monomers in monomer droplets, micelles and water, this step can take place in these three locations. Once particles are nucleated, initiators can enter inside and start new chains. Once they have been nucleated, particles continue their growth, fed by the monomer diffusion from the monomer droplet through water to the particles (interval 2). The end of this stage is characterized by a complete transformation of micelles into particles.

This last stage (interval 3) is characterized by a continuously decreasing monomer concentration. Indeed, the two first stages occur for low monomer conversion rate. All the remaining monomers polymerize during this stage. In

the end, only polymer particles are present in the aqueous phase and a latex with usually a high solid content ($\approx 50\text{-}65\%$) and sub micron polymer particles ($\approx 80\text{-}500\text{nm}$) is formed.

This three-step mechanism describes conventional emulsion polymerization in batch conditions. Due to the instantaneous initiation of polymerization, temperature increases a lot in a short span of time. A permanent strong cooling system is thus needed to control temperature of the system. These constraints can limit the scale-up of this process. In order to avoid that issue, monomers, surfactants and initiators can be fed continuously, leading to semi-continuous polymerization. Initiation processes are spread over time, which limits the increase in temperature and the stabilizez copolymer composition profile, leading to polymer particles more homogeneous (Laureau et al., 2001). This process also allows synthesizing particles under starved conditions. In that case, the feed rate of the monomers is adjusted in order to be constantly under the reaction rate. That means that the reaction environment is constant during the synthesis and, as a consequence, the monomer composition in the final copolymer is equal to the desired polymer composition. Under starved conditions, polymer chain transfer reactions are more likely to occur, due to a high ratio polymer/monomer in the particles.

1.2.2 Film formation

After having obtained a polymer in solution or in a latex, one wants to obtain it as a film to use it as a PSA. For solutions of polymers, the drying step is simply an evaporation of the solvent leading to a homogeneous film. As the polymers used are above their T_g , chains will move until reaching their equilibrium conformation in an entangled network. The viscosity of the initial solution, and thus the polymer concentration are vital parameters to obtain homogeneous films during the drying process.

One of the advantages of emulsion polymerization is that it can reach high solids contents with a low viscosity, allowing a high drying rate, contrary to polymers in solutions. However, the drying process of these latexes is more complex as polymers are concentrated in particles. Keddie summarized in details the important parameters in a review on film formation from latexes (Keddie, 1997).

The drying process is generally described by three steps (see Fig1.12). First, water evaporates, leading to a concentrated dispersion of particles. Latexes have to be dried at a temperature higher than the T_g of the polymer in the particle, called Minimal Film Formation Temperature (MFFT) to allow the next step : particles have to be soft enough to deform and fill the space between them, creating honeycomb structures. In the case of acrylic latexes used for PSAs, the MFFT is below the ambient temperature, allowing the film formation to occur without any heating. Finally, mobile polymer chains diffuse between particle interfaces leading first to mechanically strong interfaces between particles and finally to a homogeneous film.

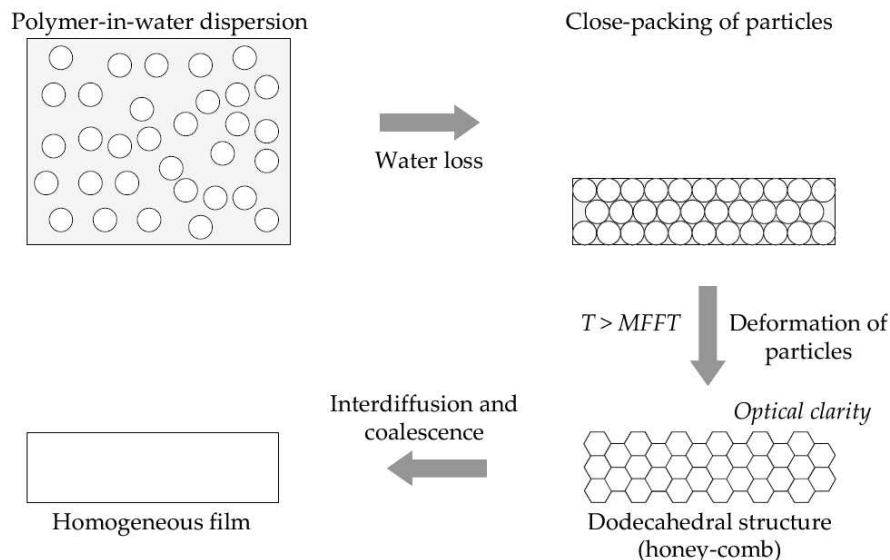


FIGURE 1.12 – Three steps of latex film formation (from Deplace, 2008).

The inter-diffusion is a process that is not always complete. Depending on this step, the memory of the particle interfaces can be retained or not in the final structure of the film. The mobility of the chains, their length and the level of cross-linking will impact the inter-diffusion of particles. Uncross-linked low M_w polymers are expected to create homogeneous films in a short time, while on the opposite, long chains with cross-links will lead to low inter-diffusion rates and in extreme cases even to weak interfaces and a more brittle material.

1.3 Mechanical characterization and properties of PSAs

In the last section, we presented the way to obtain acrylic polymers. The numerous molecular and formulation variables used to tune PSAs properties, molecular weight of the polymer, architecture of the polymer, monomer composition or additives, lead to a wide range of mechanical properties that are important to characterize. We already mentioned that, in order to show good adhesion, materials must have fine-tuned properties in small and large strain. Thus, mastering techniques to characterize these properties is essential. In the following, we will explain the characterization techniques that can be used and we will discuss the common values obtained for standard PSAs.

1.3.1 Linear Viscoelastic properties

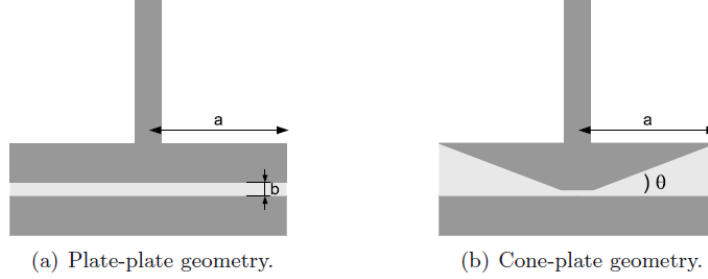


FIGURE 1.13 – Sketch of different rheometer geometries

The experiment that has been most widely used to determine the linear viscoelastic properties of polymers is small amplitude oscillatory shear (SAOS) on a rheometers. Usually, the experiment consists of a sample subjected to a simple shear deformation following a sinusoidal function between two plates or a cone and a plate (cf Fig. 1.13). In an imposed strain rheometer, the deformation is given by :

$$\gamma(t) = \gamma_0 \sin(\omega t) \quad (1.4)$$

where γ_0 is the strain amplitude and ω the frequency. The shear rate is simply obtained by differentiating the equation (1.4) :

$$\dot{\gamma}(t) = \gamma_0 \omega \cos(\omega t) = \dot{\gamma}_0 \cos(\omega t) \quad (1.5)$$

with $\dot{\gamma}_0$ the shear rate amplitude. The stress obtained is measured as a function of time, which can be described by a sinusoidal function with a phase angle or phase shift δ .

$$\sigma(t) = \sigma_0 \sin(\omega t + \delta) \quad (1.6)$$

σ_0 is the stress amplitude. The stress can be written by using a trigonometric identity to transform the equation (1.6). We obtain :

$$\sigma(t) = \gamma_0 [G'(\omega) \sin(\omega t) + G''(\omega) \cos(\omega t)] \quad (1.7)$$

where $G'(\omega)$ is called *elastic modulus* or *storage modulus* and $G''(\omega)$ is called the loss modulus. We can express these terms as function of γ_0 , σ_0 and δ :

$$G'(\omega) = \frac{\sigma_0}{\gamma_0} \cos(\delta) \quad (1.8)$$

$$G''(\omega) = \frac{\sigma_0}{\gamma_0} \sin(\delta) \quad (1.9)$$

A complex shear modulus can be defined by :

$$G^*(\omega) = G'(\omega) + i G''(\omega) \quad (1.10)$$

$G'(\omega)$ and $G''(\omega)$ can thus be seen as real and imaginary components respectively of this complex modulus. The magnitude of this complex modulus is linked to γ_0 and σ_0 :

$$|G^*(\omega)| = \frac{\sigma_0}{\gamma_0} = \sqrt{(G')^2 + (G'')^2} \quad (1.11)$$

A useful parameter is the ratio between the loss modulus and the storage modulus called *loss tangent* $\tan(\delta)$:

$$\tan(\delta) = \frac{G''(\omega)}{G'(\omega)} \quad (1.12)$$

G' can be defined as the stress in phase with the imposed strain divided by the strain. G'' is the stress out of phase of 90° with the imposed strain divided by the strain. For a perfectly elastic material, G'' is equal to zero, while for a perfectly viscous material, G' is equal to zero.

An alternative representation of the stress is to write it as a function of the dynamic viscosity :

$$\sigma(t) = \dot{\gamma}_0 [\eta'(\omega) \cos(\omega t) + \eta''(\omega) \sin(\omega t)] \quad (1.13)$$

where :

$$\eta'(\omega) = \frac{\sigma_0}{\dot{\gamma}_0} \sin(\delta) = \frac{G''}{\omega} \quad (1.14)$$

$$\eta''(\omega) = \frac{\sigma_0}{\dot{\gamma}_0} \cos(\delta) = \frac{G'}{\omega} \quad (1.15)$$

we can define a complex viscosity in the same way as the complex modulus G^* :

$$\eta^*(\omega) = \eta'(\omega) + i \eta''(\omega) \quad (1.16)$$

with :

$$|\eta^*(\omega)| = \frac{\sigma_0}{\dot{\gamma}_0} = \sqrt{(\eta')^2 + (\eta'')^2} \quad (1.17)$$

While this representation is less used for SAOS results, we will see later that it is used to compare SAOS with dynamic measurements.

It has been known since the 1940s that the viscoelastic response of a polymer material submitted to a given loading depends on both the time interval between the loading and observation and the temperature at which the mechanical test is performed (Halary et al., 2011). It was observed that behavior at a high temperature for short observation times can be equivalent to the behavior at a lower temperature for longer observation times. This principle is called Time-Temperature equivalence and holds as long as the molecular structure at the origin of the viscoelastic processes does not change with temperature.

A direct consequence of this principle is that it is possible to measure behavior at frequencies not accessible by SAOS equipments (usually 0.01Hz to

1.3. MECHANICAL CHARACTERIZATION AND PROPERTIES OF PSAS21

50Hz) by simply changing the temperature. This allows to build master curves, obtained by shifting viscoelastic curves at different temperatures in order to superimpose them to the curve obtained at the reference temperature. Examples of drawing master curves from three experiments at different temperatures are given in Fig. 1.14.

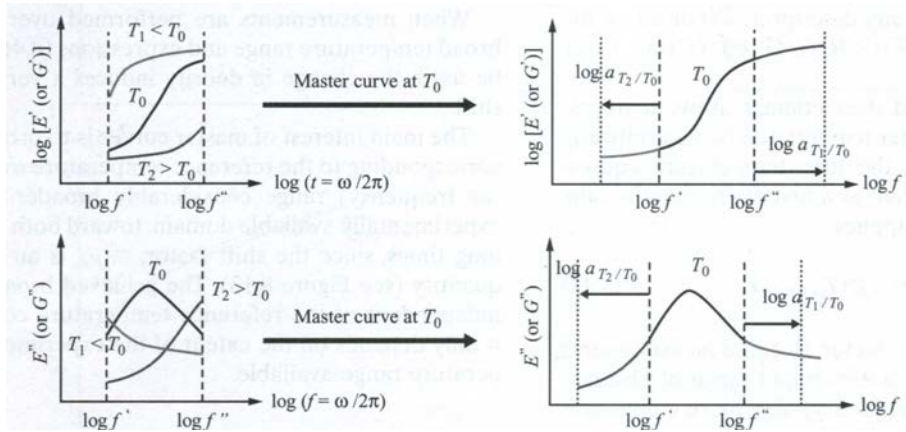


FIGURE 1.14 – Schematic drawing of a master curve from viscoelastic data (Halary et al., 2011).

These experiments allow to test the linear properties at small deformations. These linear properties obtained at small deformation can be extremely useful to understand the properties of materials, it is however important to test also non-linear properties at large deformations where new processes can happen.

1.3.2 Non-linear viscoelastic properties

While polymer materials behave following relatively simple relations at small deformations, non-linear phenomena are observed at larger deformations even in geometrically simple flows like uniaxial extension. Most of the nonlinear phenomena are observed in transient flows involving large strain and large strain rates. In order to model adhesion properties, a focus is done on uniaxial deformation, as it is the most representative geometry of the deformation occurring in a material during debonding process.

To study these phenomena, we will focus on two tests using a uniaxial extension geometry (cf Fig. 1.15) : tensile tests and extensional rheology. We will see that the only variation between the two tests is the Hencky strain rate, which is constant for extensional rheology while it is not for tensile test.

In the case of uniaxial deformation where the material is pulled in the x direction with a strain rate $\dot{\epsilon}_0$, the velocity field reads in a cartesian coordinate

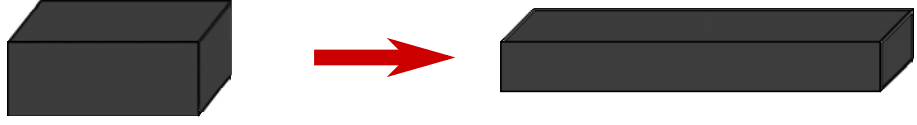


FIGURE 1.15 – Material under uniaxial geometry

system :

$$\begin{cases} v_x = \dot{\epsilon}_0 x, \\ v_y = -\frac{\dot{\epsilon}_0}{2} y, \\ v_z = -\frac{\dot{\epsilon}_0}{2} z. \end{cases} \quad (1.18)$$

Definition of normalized variables

We can measure the force as a function of the displacement, which both can be converted to stress and strain. As different definitions of stress and strains exist, we will discuss them here.

Deformations

We will note l_0 the initial length of the sample and $l(t)$ the length of the sample at a given time. F is the force applied to the material, A_0 the initial cross-section area and $A(t)$ the cross-section at a given time.

The nominal strain, or engineering strain, usually noted ϵ or ϵ_N is defined as :

$$\epsilon_N = \frac{l - l_0}{l_0} \quad (1.19)$$

The stretch or extension ratio λ is defined as :

$$\lambda = \frac{l}{l_0} \quad (1.20)$$

As a consequence :

$$\lambda = \epsilon_N + 1 \quad (1.21)$$

Another strain, called Hencky strain and noted here ϵ_H , is defined by an incremental displacement. It has as a reference the length $l(t)$ and not l_0 as for the nominal strain.

By this definition :

$$\delta\epsilon_H = \frac{\delta l}{l} \quad (1.22)$$

1.3. MECHANICAL CHARACTERIZATION AND PROPERTIES OF PSAS23

We can integrate it :

$$\int_{l_0}^l \delta\epsilon_H = \int_{l_0}^l \frac{\delta l}{l} \quad (1.23)$$

Thus :

$$\epsilon_H = \ln \frac{l}{l_0} = \ln \lambda \quad (1.24)$$

And :

$$\epsilon_H = \ln(1 + \epsilon_N) \quad (1.25)$$

Hencky strain rate and nominal strain rate are respectively defined by :

$$\dot{\epsilon}_H = \frac{\partial \epsilon_H}{\partial t} \quad (1.26)$$

$$\dot{\epsilon}_N = \frac{\partial \epsilon_N}{\partial t} \quad (1.27)$$

Stresses

The nominal stress σ_N is commonly used for plotting tensile test results. It is defined by the force divided by the initial cross-section area :

$$\sigma_N = \frac{F}{A_0} \quad (1.28)$$

The true stress is defined as the force divided by the cross-section area at a given time :

$$\sigma_T = \frac{F}{A(t)} \quad (1.29)$$

Since the sample volume is conserved during deformation, we can write that, at any time :

$$A_0 l_0 = A(t) l(t) \quad (1.30)$$

We deduce that :

$$\sigma_T = \sigma_N \frac{l(t)}{l_0} = \sigma_N \lambda \quad (1.31)$$

Tensile tests

A tensile test is a standard test to characterize the mechanical properties of solid materials. In this test, the sample is typically stretched in a tensile machine where the movable part pulls at a constant velocity (cf Fig. 1.16). The length of the sample is an affine function of time :

$$l(t) = v * t + l_0 \quad (1.32)$$

Where v is the velocity, kept constant, and l_0 is the initial length of the sample. As a consequence, the nominal strain rate is constant :

$$\dot{\epsilon}_N = \frac{\partial \epsilon_N}{\partial t} = \frac{\partial}{\partial t} \left(\frac{l(t) - l_0}{l_0} \right) = \frac{\partial}{\partial t} \left(\frac{v * t}{l_0} \right) \quad (1.33)$$

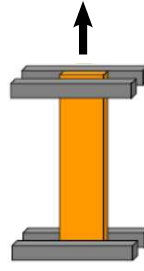


FIGURE 1.16 – Geometry of a classical tensile test

$$\dot{\epsilon}_N = \frac{\partial}{\partial t} \left(\frac{v * t}{l_0} \right) = \frac{v}{l_0} \quad (1.34)$$

If we use $\alpha = \frac{v}{l_0}$, the relation becomes :

$$\begin{cases} \epsilon_N = \alpha t \\ \dot{\epsilon}_N = \alpha \end{cases} \quad (1.35)$$

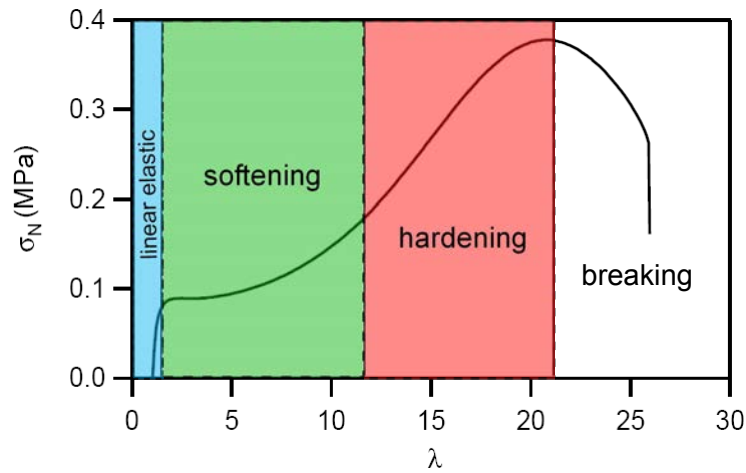


FIGURE 1.17 – Standard tensile stress-strain curve for a typical viscoelastic material

Tensile tests are usually represented by plotting σ_N as a function of λ or ϵ_N . The curve obtained for a typical viscoelastic adhesive is shown in Fig. 2.15. This curve can be separated in three parts : the first part corresponds to a linear increase of the stress corresponding to the linear viscoelastic regime. The second part shows a decrease of the slope that can be very pronounced and is called "softening". Finally, the stress strongly increases until breaking of the sample.

1.3. MECHANICAL CHARACTERIZATION AND PROPERTIES OF PSAS25

The origins of this behavior will be discussed later, when discussing elastic solids and elastomers (section 1.5.1).

Softening and hardening are a characteristic signature of the material relative to a reference behavior. In small strain the usual reference behavior for a solid is linear elasticity. However in large strain the usual reference behavior for a solid is the so-called neo-Hookean behavior, i.e. the mechanical behavior of a well crosslinked elastic rubber.

To quantitatively characterize the difference between a material and a standard rubber, tensile test data is usually plotted in the so-called Mooney representation, in which a reduced stress is plotted as a function of $1/\lambda$. The reduced stress is defined as :

$$\sigma_R = \frac{\sigma_N}{\lambda - \frac{1}{\lambda^2}}, \quad (1.36)$$

and corresponds to the nominal stress normalized by the standard behavior of a standard rubber.

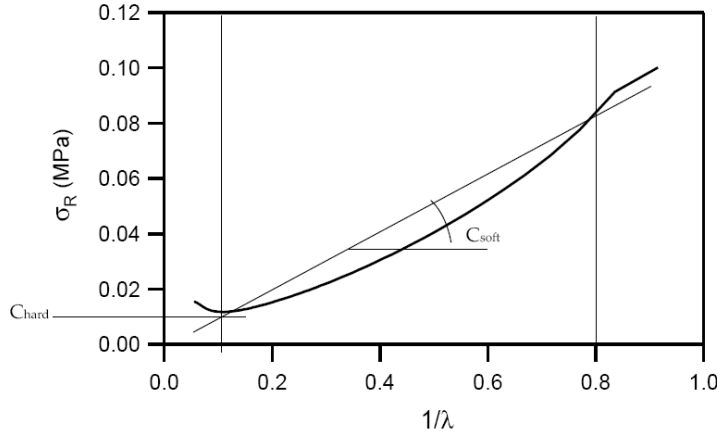


FIGURE 1.18 – Mooney representation for a typical viscoelastic material, with determination of C_{soft} and C_{hard} .

By plotting σ_R as a function of $1/\lambda$ for a typical PSA, the material non linearity is immediately apparent since such a plot should yield a constant value for a standard rubber. Two characteristic parameters of the softening and hardening, C_{soft} and C_{hard} , can be extracted from the data. A typical Mooney curve for a viscoelastic PSA material with determination of C_{soft} and C_{hard} is represented on Fig. 1.18. As the horizontal axis is $1/\lambda$, the curve reads from the right to the left. The decreasing part corresponds to the softening while the hardening is defined by the minimum of the curve at λ_{min} . C_{soft} has been defined as the slope of a line drawn between $\lambda = 0.8$ and λ_{min} . C_{hard} is defined as σ_R for λ_{min} .

These empirical parameters were defined by Deplace et al. (2009b) and later used by Agirre et al. (2010) and Bellamine et al. (2011). They are useful to

compare the type of non linear behavior encountered in different PSA materials but it should be noted that both C_{soft} and C_{hard} are not really "material" parameters since their value depends on strain rate and temperature.

Extensional rheology

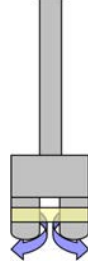


FIGURE 1.19 – Geometry of a classical extensional rheology test

Extensional rheology is not yet a common tool for the characterization of soft solids. It is more commonly used by the rheology community to characterize the non-linear properties of polymer melts and more recently viscoelastic fluids dynamically. The advantage of extensional rheology over the tensile test is that the Hencky strain rate is constant, simplifying the comparison of the data with viscoelastic models that will be discussed in section 1.5.3. In this experiment, the length of the sample $l(t)$ is kept constant by stretching the sample between two counterrotating cylinders (cf Fig. 1.19). It leads to :

$$\dot{\epsilon}_H = \frac{\partial \epsilon_H}{\partial t} = \frac{\partial}{\partial t} \left(\frac{\delta l}{l} \right) \quad (1.37)$$

During this test, the force is measured as a function of time. The results are usually presented as dynamic extensional viscosity as a function of time, with the dynamic extensional viscosity defined as :

$$\eta_E^+(t) = \frac{F(t)}{\dot{\epsilon}_H A(t)} \quad (1.38)$$

with $F(t)$ the force measured and $A(t)$ the instantaneous cross-sectional area.

The relevance of this technique was first pointed out by Cogswell (1972). Nevertheless, despite the simple approach of this test, the measurement of the transient uniaxial extensional rheology remained a technical challenge for a long time. Many of the experimental difficulties encountered were discussed by Schweizer (2000) using a RME commercial system originally developed by Meissner and Hostettler (1994). The principal issue was the need of a very precise protocol (as presented by Schweizer) to ensure reproducibility. One of the encountered problems was that the effective $\dot{\epsilon}_H$ was observed to vary from the imposed one due to inertia, gravity and surface tension. A more recent system,

known as SER, increased the performance of these measurements. Sentmanat et al. (2005) summarized the improvements in an article and obtained good reproducibility on polymer melts. One limit of this system is the maximal elongation of the sample : the material is stretched and rolled around two drums. After one turn of the drum, the material covers itself. Maia et al. (2012) developed a new system allowing infinite elongation and possible feed-back control by a direct visual measurement of the size of the sample. This allows to correct the effective strain rate in real time. Up to now, extensional rheology has rarely been used to characterize solid viscoelastic materials at ambient temperature.

When studying the extensional rheology of a material, using the Cox-Merz rule (Cox and Merz, 1958) can be useful. According to this empiric rule, the oscillatory steady state shear viscosity $\eta^*(\omega)$ at a given pulsation is equal to the dynamic viscosity $\eta^+(\dot{\epsilon}_H)$ at the same frequency. So, for $\dot{\epsilon}_H = \omega$:

$$\eta^+(\dot{\gamma}) = \eta^*(\omega) \quad (1.39)$$

Thus, it is possible to compare properties in the linear regime from SAOS with extensional viscosity by using a factor 3 due to the different geometries between shear and uniaxial extension. If the material shows the same behavior, then :

$$3\eta^+(\dot{\gamma}) = \eta_E^+(t) \quad (1.40)$$

when $t = 1/\dot{\gamma}$.

Comparing tensile test and extensional rheology

While tensile tests and extensional rheology have the same geometry (uniaxial elongation), their principal difference resides in the strain-rate applied to the sample. As noted above, the nominal strain rate $\dot{\epsilon}_N$ is constant in a tensile test while it is the Hencky strain rate $\dot{\epsilon}_H$ that is kept constant during an extensional rheology test. One way to understand this difference is to use $\dot{\epsilon}_H$ for both experiments : in that case, in a tensile test, $\dot{\epsilon}_H$ is dependent on time. Combining Eqs. (1.25) and (1.35), we obtain :

$$\dot{\epsilon}_H = \frac{\alpha}{1 + \alpha t} \quad (1.41)$$

Thus, a tensile test is equivalent to a test of extensional rheology with an $\dot{\epsilon}_H$ that decreases following the relation given by Eq. 1.41.

Another way to look at that problem is to find a non-constant $\epsilon_N(t)$ that would correspond to a constant $\dot{\epsilon}_H$ in a tensile test. Writing :

$$\epsilon_H = \ln(1 + \epsilon_N), \quad (1.42)$$

With $\beta = \dot{\epsilon}_H$, we obtain :

$$\frac{\dot{\epsilon}_N(t)}{1 + \epsilon_N(t)} = \beta \quad (1.43)$$

In that case, we obtain a simple differential equation :

$$\dot{\epsilon}_N(t) - \beta\epsilon_N(t) = \beta \quad (1.44)$$

The solution of this first-order differential equation is well-known as :

$$\epsilon_N(t) = K \exp(\beta t) - 1 \quad (1.45)$$

where K is a constant. In our case, $\epsilon_N(0) = 0$, so $K=1$, giving :

$$\epsilon_N(t) = \exp(\beta t) - 1 \quad (1.46)$$

and :

$$\dot{\epsilon}_N(t) = \beta \exp(\beta t) \quad (1.47)$$

The consequence of this result is that the extensional rheology can be seen as a tensile test where the pulling velocity follows an exponential increase. While the two tests are identical at low strains, the differences can be very important at large strains. These considerations are important to understand the differences in results obtained with the two methods.

1.4 Adhesive characterization and debonding mechanisms of PSA

In this section, we will discuss classical techniques used to characterize adhesion of pressure-sensitive-adhesives. We will close the section by discussing the knowledge about the transitions between debonding mechanisms, their relation with mechanical properties and the limitations of current PSAs systems.

1.4.1 Characterisation of adhesive properties of PSA

The performances of a PSA are characterized by its properties in peel, shear and tack. Peel is defined as the force needed to remove a tape of PSA from a substrate. Shear resistance is defined by the resistance of the adhesive to failure in the direction parallel to the interface at long times. Finally, tack is the capability to stick instantaneously to a substrate with the application of a light pressure.

Industry defined early empirical tests that could be used to get a simple comparison between different adhesives with a precise protocol. Those tests will be discussed in a first part. However, understanding the details of the debonding mechanisms or the physical parameters controlling the adhesive properties is limited with these tests. To improve this understanding, an instrumented version of the probe-tack test was developed by Zosel in the late 80's (Zosel, 1985) and later improved by our group (Lakrou et al., 1999; Josse et al., 2004).

Industrial characterization

The Pressure-Sensitive Tape Council in the USA and the FINAT in Europe developed and normalized different empirical tests that are widely used to test the adhesive properties of PSA.

*PSTC-101 International Standard for Peel Adhesion of Pressure Sensitive Tape*¹ is a normalized test used to characterize peel properties. This test measures the strength required to detach a PSA from a given surface (in N/m). Two pulling angles can be used, 90° (Fig. 1.20) or 180°. The peeling rate, the substrate and the contact time can be varied. Peeling properties are dependent on the dissipation properties of the adhesive and on its cohesion. Viscous behavior is needed to dissipate energy while elastic behavior is needed to keep a good cohesion of the material and ensures adhesive debonding. When a debonding at the interface (adhesive debonding) is targeted, the material will need a fine tuning of its viscoelastic properties (Marin and Derail, 2006).

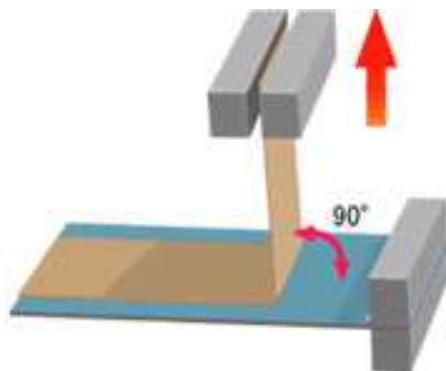


FIGURE 1.20 – Standard peel-test at 90 °.

Resistance to shear can be measured by the standardized *PTSC-107 Shear Adhesion of Pressure Sensitive Tape*. In this test, the time at which the adhesive bond fails under a given load is measured. Contact area and load can vary, but 25.4mm x 25.4mm (1 inch x 1 inch) contact area and a load of 1kgf (9.81 N) are commonly used (see Fig. 1.21). PSAs must resist over a long period of time (requirements are usually over 10000 min in these standard loading conditions and at room temperature). In order to reach these performances, adhesives must exhibit sufficiently large elastic moduli as well as a strain hardening at high strains to prevent flow at long times.

Different simple tack methods that are easy to implement, such as the loop tack test or the rolling ball test, exist and give quick results on the tack properties of materials. Nevertheless, the information is particularly limited on these

1. Informations on this test can be found on the website of PSTC : <http://www.pstc.org/i4a/pages/index.cfm?pageid=3379>.

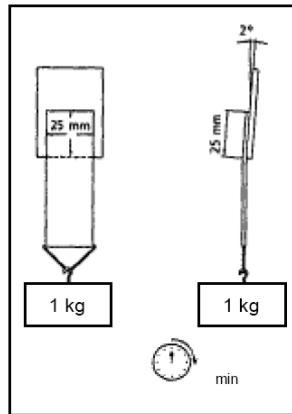


FIGURE 1.21 – PSTC-107 shear test <http://www.pstc.org/i4a/pages/index.cfm?pageid=3379>.

tests. Because of these limitations, Zosel, a research scientist working at BASF, developed the probe-tack test (Zosel, 1989), that will be discussed in more detail.

Probe-Tack test

In a typical probe-tack test, a cylindrical flat ended probe is brought into contact with an adhesive layer. After a preset contact time which can be varied, the probe is pulled away at a constant rate. Probes can be made of a variety of materials, stainless steel being used as a standard. The force F and displacement d as a function of time are measured during the whole experiment (cf Fig. 1.22). From these data, normalized variables nominal stress and strain can be obtained. Probe-tack results are usually presented by stress vs strain curves.

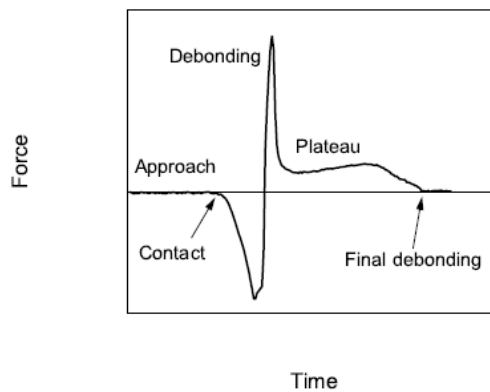


FIGURE 1.22 – Typical force-time curve in the probe tack test

1.4. ADHESIVE CHARACTERIZATION AND DEBONDING MECHANISMS OF PSA31

Initially developed by Zosel (1989), the probe-tack test was further implemented and improved to study the debonding mechanisms in details (Lakrout et al., 1999; Creton et al., 2001). The effect of different parameters such as the contact time, pressure or debonding velocity (Creton and Fabre, 2002) or the effect of the confinement (ratio between the radius of the probe and the thickness of the film a/h) were studied in details (Webber et al., 2003).

The adhesion energy W_{adh} is defined here as the energy dissipated during the debonding process. It can be calculated as the area under the curve multiplied by the initial thickness of the layer h_0 between 0 and the deformation at failure ϵ_{max} :

$$W_{adh} = h_0 \int_0^{\epsilon_{max}} \sigma_N d\epsilon \quad (1.48)$$

For a permanent PSA, this adhesion energy should be as high as possible while keeping a clean removal (no macroscopic residues) from the surface.

A description of the debonding mechanisms occurring during these tests, originally discussed by Creton, Hooker and Shull (Creton et al., 2001) and later developed by Nase et al. (2010) is summarized in Fig. 1.23. When a PSA is deformed, low-pressure cavities nucleate at the interface and quickly grow. Depending on the properties of the adhesives and the substrate, the cavities propagate at the interface or grow in the bulk. This then either leads to an interfacial deformation with low level of dissipation (case A), or a deformation in the bulk. In that case, fibrils formed by the material around the cavities, are stretched, leading to a stress plateau, dependent on the sample elasticity at large strains (Roos and Creton, 2005). The cavity walls will then either detach from the interface (case B) or break in the bulk, usually preceded by a breakup of the walls between cavities to equilibrate the pressure, leading to a characteristic two-plateaus curve of liquid-like material (case C) that has been well described by Poivet et al. (Poivet et al., 2003, 2004).

The implementation of a visualization of the complex kinematics of the debonding process (Lakrout et al., 1999; Josse et al., 2004) has brought very important information on fingering instabilities (Derks et al., 2003; Nase et al., 2010; Yamaguchi et al., 2007) and cavitation (Tirumkudulu et al., 2003; Poivet et al., 2003, 2004; Chiche et al., 2005) and on the evolution of the shape of the cavities as debonding proceeds (Lindner et al., 2004). A typical picture observed during a probe-tack test is shown in Fig. 1.24 : bubbles observed in the picture are the cavities presented above. Recently, Peykova et al. further developed this approach by studying the average growth rate of cavities as a function of the roughness by an analysis of these images (Peykova et al., 2010, 2012).

A quantitative analysis of the debonding structure of PSAs based on image analysis will be discussed in the third chapter of this thesis.

1.4.2 Debonding mechanisms

The probe-tack test gives us a powerful method to characterize the adhesive properties of PSAs and link them to their mechanical properties. In the following

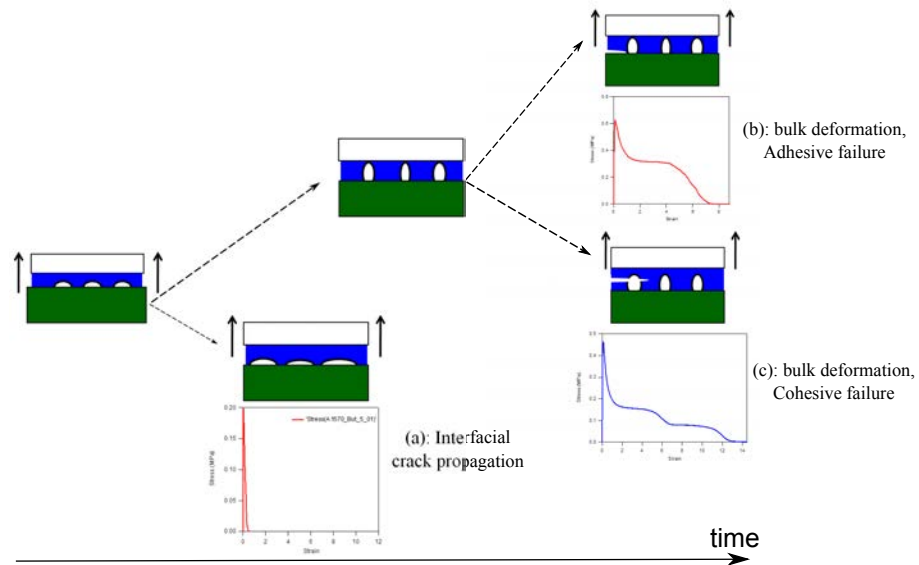


FIGURE 1.23 – Different stress-strain curves obtained from probe-tack tests. At the beginning, the material either debonds at the interface, leading to (a), or deforms in the bulk. Fibrils stretch until the material fails at the interface (b : adhesive failure) or in the bulk (c : cohesive failure).

section, we will discuss the transition between the three observed mechanisms A, B and C and their relation with the mechanical and rheological properties of the adhesive.

Transition between interfacial crack propagation and bulk deformation

As discussed in section 1.3.1, values of storage modulus G' , loss modulus G'' and phase angle $\tan \delta$ can be easily obtained from SAOS tests. These parameters can be used to predict if the material will deform mainly in its bulk (case B or C) or will detach at the interface without forming fibrils (case A).

The evolution of the growth of the initially formed cavities is governed by two competitive phenomena. On one hand, cavities can grow in the bulk of the adhesive layer by deforming it. The rate of growth will be controlled by the elastic modulus E for an elastic material, or by G' for a viscoelastic material. On the other hand, cavities can also propagate at the interface like a crack. This phenomenon is driven by the critical energy-release rate G_c , the energy per unit area needed to make an interfacial crack move. The ratio between G_c and the energy per unit volume necessary to deform the bulk E is a characteristic length which can be used to differentiate interfacial propagation from bulk deformation

1.4. ADHESIVE CHARACTERIZATION AND DEBONDING MECHANISMS OF PSA33

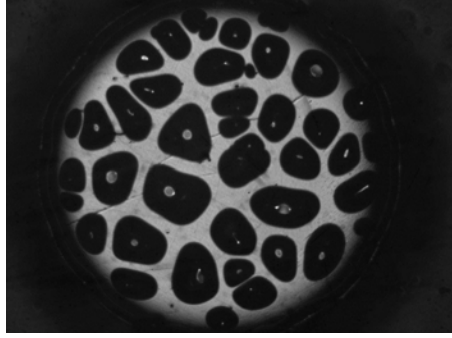


FIGURE 1.24 – Visualization of the debonding from the top during a probe-tack experiment

for elastic materials (Crosby et al., 2000; Creton et al., 2001; Webber et al., 2003). More specifically, three regimes can be determined, dependent on the thickness of the adhesive layer h and the radius r of initially existing interfacial defects :

- if G_c/E is smaller than r , only interfacial propagation is observed,
- if G_c/E is higher than h , the bulk is deformed,
- in the intermediate cases, the transition between the two extreme situations is observed.

These three cases are summarized on Fig. 1.25.

While this approach is useful for elastic materials, we cannot simply use G_c or E for viscoelastic materials as are PSAs. An extension of this model has been introduced by Deplace et al. (Deplace et al., 2009b). First, for a viscoelastic material, G_c depends on the strain rate and the dissipation processes. Maugis and Barquins (Maugis and Barquins, 1978) proposed an empirical equation for the dependence on G_c as :

$$G_c = G_0 (1 + \Phi(a_T V)) \quad (1.49)$$

where G_0 is the resistance to crack propagation at vanishingly low crack velocity and $\Phi(a_T V)$ is the dissipative factor. Deplace et al. proposed an approximated Φ as a linear function of $\tan \delta(\omega)$ (Deplace et al., 2009b), which leads to :

$$\Phi(a_T V) = k \tan \delta(\omega) \quad (1.50)$$

where k is a constant. Even if our materials are more viscoelastic than elastomers, this approach can be used as a first approximation. As a consequence, for a viscoelastic material :

$$\frac{G_c}{E} = \frac{G_0 (1 + \Phi(a_T V))}{G'(\omega)} = \frac{G_0 (1 + k \tan \delta(\omega))}{G'(\omega)} \quad (1.51)$$

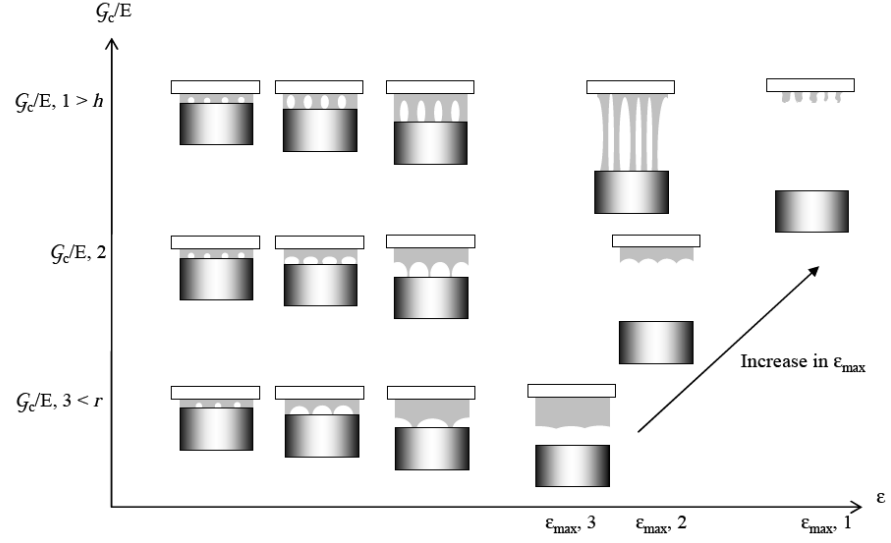


FIGURE 1.25 – Debonding process involved for during probe tack test for elastic materials. Three typical cases are displayed, leading to different debonding mechanisms (from Deplace et al., 2009b).

Finally :

$$\frac{G_c}{E} \approx k \frac{G_0 \tan \delta(\omega)}{G'(\omega)} \quad (1.52)$$

This ratio depends only on the linear properties of the material and on G_0 , dependent on the surface chosen. Thus, for a given surface, we can determine a value of $\tan(\delta)/G'$ which characterizes the transition between interfacial crack propagation and bulk deformation (see Fig. 1.26). This approach has been confirmed experimentally by Nase et al. (Nase et al., 2008).

Linear properties can thus give important insight to predict interfacial crack propagation or bulk deformation. Non-linear properties are needed however to give us information about the final debonding, adhesive or cohesive, that will occur when fibrils are formed, i.e. in the regime where $\tan \delta/G'$ is large and deformation is high. This will be discussed in more details in the following paragraph.

Transition between adhesive and cohesive failure

When deformation occurs primarily in the bulk, fibrils are elongated to very large strains until interfacial detachment or cohesive failure occurs (Hui et al., 2005). Thus, understanding the properties of the materials under uniaxial deformation at constant velocity, e.g tensile tests discussed in section 1.3.2 is useful.

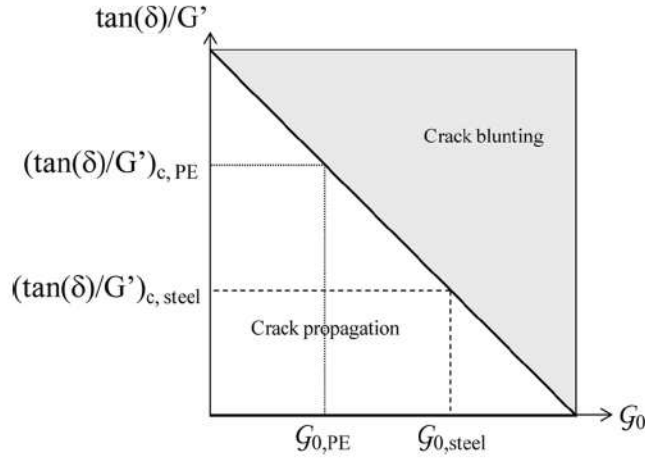


FIGURE 1.26 – Prediction of the transition from interfacial crack propagation to bulk deformation (from Deplace et al., 2009b).

The parameters C_{soft} and C_{hard} can be especially useful as they characterize softening and hardening of the material. Indeed, softening is needed to reach high deformation (high ϵ_{max}) and thus to maximize energy dissipation during the extension of the fibrils. Hardening is needed to obtain strong fibrils that will not break in their middle but will detach from the substrate.

The C_{soft}/C_{hard} ratio corresponds to the viscoelastic relaxation of the sample relative to its permanent crosslink structure (Deplace et al., 2009b). A high ratio characterizes a sample with high dissipation with non-permanent crosslinks while a low value corresponds to materials highly crosslinked with low dissipation. As it was discussed in the section 1.1.2, PSA must show dissipation during debonding and an elastic behavior to resist shear at long times. Elastic behavior is also needed to obtain adhesive debonding. Deplace et al. (2009b) and Bellamine et al. (2011) et al. showed that a value $\approx 2 - 3$ lead to efficient adhesives on stainless steel, confirming that hardening is needed to ensure an adhesive debonding on high adhesion surfaces like stainless steel.

1.4.3 Limits of actual PSA systems

The discussion in the last section showed that, in order to get optimal PSAs, different parameters need to be optimized. The ratio $\tan \delta/G'$ needs to be carefully controlled to ensure bulk deformation and avoid crack propagation **at the interface**, while some softening in large strain is needed to ensure maximal dissipation and eventual hardening at large strain is needed to avoid failure **in the bulk**. Moreover, in order to get good resistance to shear over long times, materials need also a high G' at low frequency and show some hardening in

large strain. In other words, a fine tuning is needed to get the best PSA possible that is highly dependent on the application targeted. Fulfilling these different and sometimes contradictory requirements is often not possible and compromises have to be made. These compromises are especially important on surfaces where adhesion is low, like polyolefins.

In order to obtain better properties than those imposed by this compromise, different inhomogeneous materials have been developed. Lately, waterborne nanostructured adhesives composed by latexes with core-shell particles were studied (Deplace, 2008), as well as hybrid urethane/acrylic latexes (Degrandi, 2009; Bellamine et al., 2011). More specifically, Carelli et al. showed that bi-layer adhesives, optimizing properties at the interface and in the bulk, were an interesting approach to improve adhesives properties of PSAs (Carelli et al., 2007).

In this thesis, we will show that it is possible to find a way to optimize material properties of PSAs, depending on the targeted application using model acrylic materials.

1.5 Modeling elastic solids, viscous fluids and viscoelastic materials

As discussed above, the performances of current PSAs are limited by a compromise needed between their elastic and their viscous properties. A fine tuning of the viscoelasticity is thus needed. Previous works discussed in the last section helped to formulate good PSAs empirically by characterizing the most relevant material parameters. Nevertheless, it is still difficult to directly link these material parameters to adhesive performance. This is particularly true for waterborne acrylic polymers which have complex interfaces at the submicron scale between the particles of the latex used to make the PSA. It is thus important to present some fundamental knowledge about modeling strategies used for viscoelastic materials.

First, a few non-dimensional parameters should be introduced to differentiate flow regimes :

Deborah number

The Deborah number is defined as :

$$De = \frac{\lambda}{\tau} \quad (1.53)$$

where λ is a characteristic time scale of the fluid studied and τ is a characteristic time of the flow. De represents the transient nature of the flow relative to the fluid time scale. If the observation time scale is small compared to the characteristic time of the flow ($De \ll 1$), the material behaves like a solid, while

on the opposite ($De \gg 1$) the material will behave like a liquid. It is interesting to see here that the transition from a solid to a liquid is only a question of observation time. Indeed, the Deborah number gets its name from a verse of the Bible where the prophetess Deborah states in a song "The mountains flowed before the Lord"². The limiting cases are when $De = 0$ for a perfect liquid (called Newtonian liquid) and $De = \infty$ for an elastic solid. The Deborah number is not specific to polymer materials and characterizes the rate at which the fluid stores and releases elastic energy. It is a parameter which is associated with linear viscoelasticity.

Weissenberg number

The Weissenberg number is defined as :

$$Wi = \lambda \dot{\gamma} \quad (1.54)$$

$\dot{\gamma}$ being the characteristic shear rate or extension rate of the flow. The Weissenberg number is only meaningful in steady flow and compares the relative importance of the elastic forces due to the orientation of the chains and the viscous effects : for a high Wi , the elastic restoring forces drive the flow behavior while for a low Wi the viscous effects are the major forces. It is interesting to note that a flow with a small Wi and a large De is possible as is the opposite (Dealy, 2010).

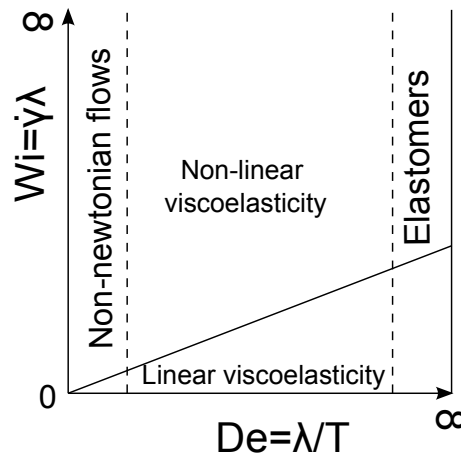


FIGURE 1.27 – Pipkin diagram, delimiting different flows as a function of the De and the Wi number.

Pipkin's diagram (Pipkin and Tanner, 1972) is useful to understand the models and their range of validity as a function of De and Wi . In Fig. 1.27, Wi is represented on the vertical axis and De on the horizontal axis. The Newtonian

². For obvious reasons, this book does not appear in the bibliography. The citation is extracted from an anthem known as the *song of Deborah*, Judges(5 :5).

liquid is represented by the point where $De = Wi = 0$, while the elastic response is represented by a single point, when $De = \infty$. The domain "elastomers" on the right side will be discussed in the *Elastic solids and elastomers* part while non-Newtonian flows will be discussed in the *Viscous fluids* part. The central part presents the part when viscoelastic models are needed to describe the behavior of the material, described in the *Viscoelasticity* part.

1.5.1 Elastic solids and elastomers

An elastic solid is a material able to be deformed reversibly without any energy dissipation. In an amorphous polymer network, the presence of cross-links is the source of elasticity. In such materials, when the temperature is above the glass transition temperature T_g , chains between crosslinks are mobile but on a limited range. Such materials, which can be deformed nearly reversibly several times their original length, are called elastomers. At the macroscopic scale, they behave as a solid. At small strains, they behave like a linear elastic (or Hookean) solid, following Hooke's law :

$$\sigma_N = E\epsilon \quad (1.55)$$

where σ_N is the nominal stress defined as the force divided by the initial section area, ϵ the nominal strain, defined as $(l - l_0)/l_0$ with l the length of the sample, l_0 its initial length and E the Young's modulus. This relation is only true for small deformations.

Affine and Phantom network models

An affine model, derived from thermodynamical considerations can predict the behavior of an elastomer for small to medium deformations (Colby and Rubinstein, 2003). From this model, nominal stress is linked to the deformation $\lambda = \epsilon + 1$ by :

$$\sigma_N = \nu kT \left(\lambda - \frac{1}{\lambda^2} \right) \quad (1.56)$$

where k is the Boltzmann constant, T the temperature (in K) and ν is the number of cross-links per unit volume. The shear modulus G_x that can be calculated by :

$$G_x = \frac{\rho RT}{M_x} \quad (1.57)$$

where ρ is the network density, R the gas constant, and M_x the number-average molar mass between two cross-links. Thus, Eq. (1.56) becomes :

$$\sigma_N = G \left(\lambda - \frac{1}{\lambda^2} \right) \quad (1.58)$$

In this model, cross-links are supposed to be fixed in space and displaced affinely within the whole network.

The phantom network model is the simplest model incorporating spatial fluctuations of the cross-links. In that case, if we define f as the functionality of the network, i.e the number of chains attached to each nod of the network, we obtain :

$$\sigma_N = \nu kT \left(\lambda - \frac{1}{\lambda^2} \right) \left(1 - \frac{2}{f} \right) \quad (1.59)$$

Both the affine and phantom network model predict the same dependency of stress on deformation. As shown from experimental data, the behavior of typical elastomers differs from these models. A softening is observed at intermediate deformations and hardening at higher deformations. Some phenomenological alternatives have been developed.

Doi-Edwards tube model

The models presented in the previous paragraph does not explain why the modulus of an uncross-linked network of extremely long chains does not fall toward zero but reaches a plateau. In a real network made of long and linear chains, the chains impose topological constraints on each other due to the presence of entanglements. Doi and Edwards (1978) showed that the entanglements restrict the available conformations of a chain to a confining tube of diameter defined as the length between two entanglements. In that case, the entanglements effectively replace cross-links, and Eq. 1.57 can be rewritten as :

$$G_e = \frac{\rho RT}{M_e}, \quad (1.60)$$

M_e being the weight between two entanglements. In the case of cross-linked networks, the modulus can thus be written as :

$$G = G_e + G_x. \quad (1.61)$$

The modulus is controlled by crosslinks for low molecular mass strands between cross-links ($G \approx G_x$ for $M_x < M_e$) and by entanglements for high molar mass strands between cross-links ($G \approx G_e$ for $M_x > M_e$).

Rubinstein - Panyukov model

To complete the Edwards tube model and to extend it to higher deformations, Rubinstein and Panyukov (Rubinstein and Panyukov, 1997, 2002) proposed a non affine tube model in which the deformations of the tubes and random cross-links are taken into account.

This leads to a relation between the Mooney stress (already presented in section 1.3.2) and G_x and G_e .

$$\sigma_R = \frac{\sigma_N}{\lambda - \frac{1}{\lambda^2}} = G_x + \frac{G_e}{\lambda + \lambda^{-1/2} - 1} \quad (1.62)$$

This approach leads to a relation between the Mooney stress and the modulus from entanglements and crosslinks, E_e and E_x respectively. This solution is in good agreement with experiments on uniaxial deformation of networks in tension. Nevertheless, it overpredicts the stress required to compress a network. Rubinstein and Panyukov took into account that chains along the deformation are elongated and compressed towards other chains by introducing a non-affine slip-tube model. The resulting dependence of stress on the deformation does not have an analytical solution but has been numerically solved for $0.1 < \lambda < 10$ and can be approximated by :

$$\sigma_R = \frac{\sigma_N}{\lambda - \frac{1}{\lambda^2}} = \left(\frac{G_e}{0.74\lambda + 0.61\lambda^{-1/2} - 0.35} \right) \quad (1.63)$$

Eq. 1.63 can be reduced to Eq. 1.62 in the small deformation limit. This simple equation separates the contribution from entanglements from that of crosslinks and hence allows them to be determined experimentally.

Mooney-Rivlin model

The Mooney-Rivlin model allows to catch the softening in uniaxial extension with a fairly easy expression. This model was developed by Mooney (Mooney, 1940) and later developed by Rivlin. It introduces a modulus depending on the deformation λ . In that case, the nominal stress becomes :

$$\sigma_N = 2 \left(C_1 + \frac{C_2}{\lambda} \right) \left(\lambda - \frac{1}{\lambda^2} \right) \quad (1.64)$$

C_1 and C_2 are two positive material constants. C_2 is the parameter characterizing the softening behavior : when $C_2=0$, the model is equivalent to a classical neo-hookean equation with the modulus shear $G = 2C_1$. The higher C_2 is, the more important will be the decrease of the modulus as a function of λ will be, showing a more important softening.

The so-called Mooney or Mooney-Rivlin representation using a reduced stress as a function of $1/\lambda$, already presented in section 1.3.2, allows to show well C_1 and C_2 (see Fig. 1.28). The reduced stress σ_R is defined as :

$$\sigma_R = \frac{\sigma_N}{\lambda - \frac{1}{\lambda^2}} = 2 \left(C_1 + \frac{C_2}{\lambda} \right) \quad (1.65)$$

The Mooney-Rivlin model captures well the softening that numerous elastomers show under deformation, but does not capture the hardening part.

Hardening models

At high strain, elongated chains between cross-links impose a maximal deformation of the network (cf Fig 1.29). This leads to a strong increase of the stress at high strain when approaching the maximal deformation of this network.

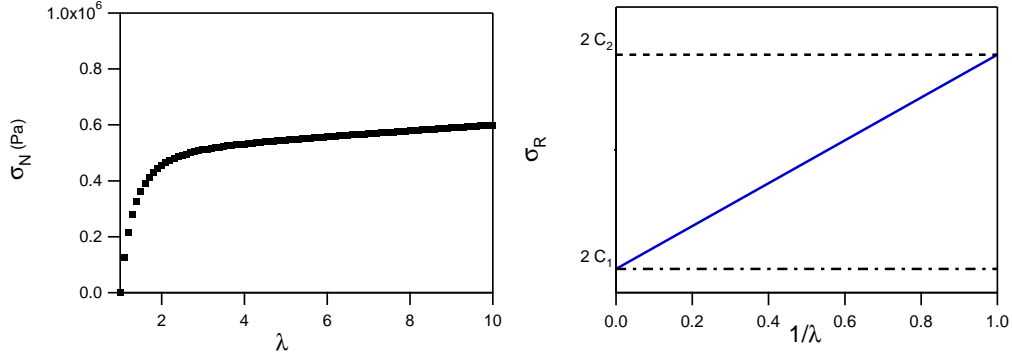


FIGURE 1.28 – Mooney-Rivlin model plotted as nominal stress versus deformation (left) and in the Mooney-Rivlin representation (right). C_1 and C_2 values are easily seen from the Mooney-Rivlin plot.

Numerous phenomenological and physical models have been proposed to capture this behavior. Gent proposed a simple model (Gent, 1996) by introducing a maximal value J_m of J_1 , with $J_1 = I_1 - 3$, I_1 being the first strain invariant. In the case of uniaxial deformation :

$$J_1 = \lambda^2 + \frac{2}{\lambda} - 3 \quad (1.66)$$

J_m is defined as J_1 for the maximal elongation λ_m allowed by the network :

$$J_m = \lambda_m^2 + \frac{2}{\lambda_m} - 3 \quad (1.67)$$

Under these assumptions, the nominal stress can be written as :

$$\sigma_N = G \left(\lambda - \frac{1}{\lambda^2} \right) \frac{1}{1 - \frac{J_1}{J_m}} \quad (1.68)$$

When λ approaches λ_m , the stress diverges to infinity, as is observed for cross-linked elastomers before they break.

Seitz et al. (2009) proposed a model based on the same hypothesis but used an exponential term which seems to better describe the hardening behavior. It has the advantage to avoid divergent stress for $J_1 = J_m$ that creates problems in finite element codes. In that case, for uniaxial deformation, the nominal stress can be expressed as :

$$\sigma_N = G \left(\lambda - \frac{1}{\lambda^2} \right) \left(\exp\left(\frac{J_1}{J_m}\right) \right) \quad (1.69)$$

A comparison between the results given by the two models are represented in Fig. 1.30.

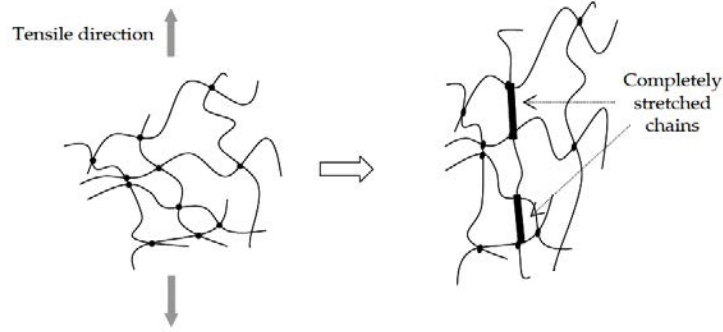


FIGURE 1.29 – Schematics of the maximal extensibility of stretched polymer chains (from Deplace (2008)).

These hardening models can be added to a Mooney-Rivlin model in order to capture the softening and the hardening. For example, coupling a Gent model with a Mooney-Rivlin would follow to an expression of the nominal stress as :

$$\sigma_N = \left(C_1 + \frac{C_2}{\lambda} \right) \left(\lambda - \frac{1}{\lambda^2} \right) \frac{1}{1 - \frac{J_1}{J_m}} \quad (1.70)$$

In that case, three parameters are needed to describe the material : C_1 , C_2 and J_m . The comparison with a simple Gent model is presented in Fig. 1.31.

These models can be compared to tensile curves of typical PSAs, see Fig. 1.32. We clearly see a good matching of these models at low to intermediate strains, while the final hardening seems too strong in both models. Moreover, the equations discussed above show no dependency at all with the strain rate, while we observe, especially for weakly crosslinked PSA, a high influence of the strain rate. We thus understand that we need at least to introduce a viscoelastic contribution in order to model PSAs.

1.5.2 Viscous fluids

At the other limit of the Pipkin diagram (fig.1.27), for $De = Wi = 0$, the flow can be described as Newtonian. As for viscous fluids the shear properties are highly dependent on viscosity, we will need to study the stress in x and y directions. Thus, we will use 3x3 tensors that will replace scalars for this part. The tensors will be written as \underline{X} . For example, the stress tensor $\underline{\tau}$ is :

$$\underline{\tau} = \begin{pmatrix} \tau_{xx} & \tau_{xy} & \tau_{xz} \\ \tau_{yx} & \tau_{yy} & \tau_{yz} \\ \tau_{zx} & \tau_{zy} & \tau_{zz} \end{pmatrix} \quad (1.71)$$

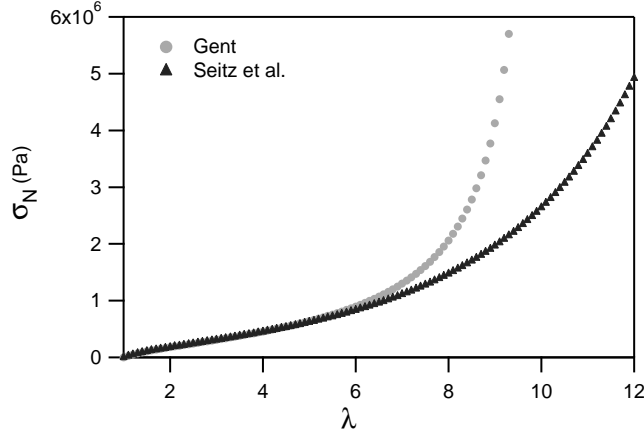


FIGURE 1.30 – Exemple of Gent model and Seitz et al. model for $G = 100kPa$ and $J_m = 100$.

In the case of a shear flow, the tensor can simplify as :

$$\underline{\underline{\tau}} = \begin{pmatrix} 0 & \tau_{xy} & 0 \\ \tau_{yx} & 0 & 0 \\ 0 & 0 & 0 \end{pmatrix} \quad (1.72)$$

$$\underline{\underline{\dot{\gamma}}} = (\nabla v + \nabla v^T) \quad (1.73)$$

where ∇ stands for the mathematical operator **grad** and v is the flow field vector.

For a newtonian fluid, the tensor has a unique component :

$$\tau = \tau_{yx} = \tau_{xy} \quad (1.74)$$

For an incompressible Newtonian flow, we use the expression defined by Bird et al. (Bird et al., 1977) :

$$\underline{\underline{\tau}} = -\mu \underline{\underline{\dot{\gamma}}} \quad (1.75)$$

where μ is the viscosity of the fluid, constant for a given temperature, pressure and composition. μ is independent of the strain rate for Newtonian fluids. Especially for polymers, the viscosity can change by a few orders of magnitude depending on the strain rate. Therefore, the non-Newtonian models will be written as :

$$\underline{\underline{\tau}} = -\eta(\underline{\underline{\dot{\gamma}}}) \underline{\underline{\dot{\gamma}}} \quad (1.76)$$

where η is a viscosity dependent on the strain rate $\underline{\underline{\dot{\gamma}}}$. The next step is then to find different ways to express the relation between the viscosity and the strain rate.

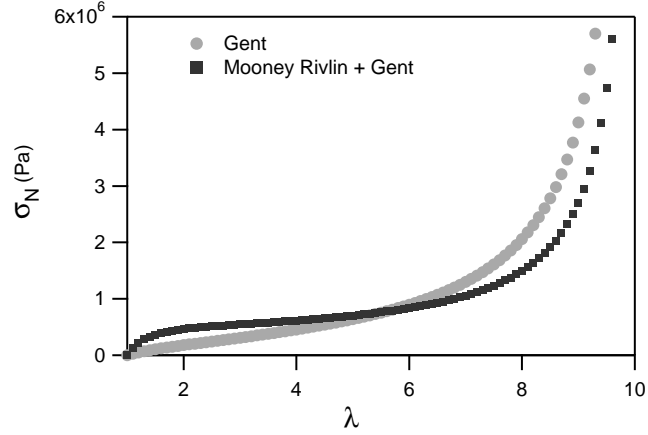


FIGURE 1.31 – Example of Gent model with $G = 100kPa$ and $J_m = 100$ and of the Gent model coupled with a Mooney-Rivlin model for $C_1 = 10kPa$, $C_2 = 500kPa$ and $J_m = 100$.

A simple way to do it is the one following a power-law relation between η and $\dot{\gamma}$. Ostwald and de Waele proposed a simple model which contains only two parameters m and n :

$$\eta = m\dot{\gamma}^{n-1} \quad (1.77)$$

When $n = 1$ and $m = \mu$ we recover the Newtonian fluid expression. If $n < 1$, the fluid is *shear thinning* and is *shear thickening* for $n > 1$.

Other models for the relation between η and $\dot{\gamma}$ exist. A summarizing table has been given by Bird et al. in the *Dynamics of Polymeric fluids* (Bird et al., 1977).

1.5.3 Viscoelasticity

We already discussed the two limits of the Pipkin diagram (Fig. 1.27) which were elastomers and non-Newtonian fluids. The main central part of the Pipkin diagram can be described by viscoelastic models. Indeed, most of the polymeric materials behave somewhere in between the purely elastic solid and the pure Newtonian liquid. This leads to transient responses that can be observed with some easy experiments. For example, when put under constant stress, the deformation will not remain constant but will continue to grow over time. If a viscoelastic solid is constrained at constant deformation, the stress will go up to a given value and will then relax with time until reaching a given value. This is known under the name of relaxation. Examples are given in Fig. 1.33.

In this part we will see how elasticity and viscosity concepts can be combined to capture these particular behaviors.

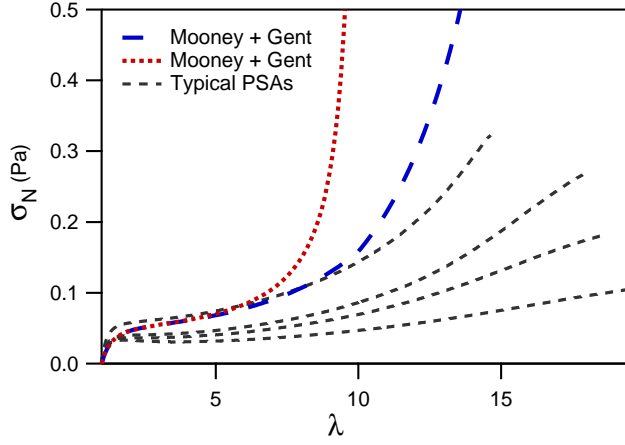


FIGURE 1.32 – Comparison of a Gent-Mooney and Seitz-Mooney models with typical tensile curves of PSAs

Maxwell model

The easiest approach to model linear viscoelasticity is to describe the material as a sum of an ideal elastic component (Hookean) and an ideal viscous component (Newtonian fluid). These two models can be added in two ways : as two components in series, leading to the Maxwell model, or in parallel leading to the Kelvin-Voigt model. The Maxwell model describes the behavior of a viscoelastic fluid and the Kelvin-Voigt model a viscoelastic solid. Usually, an analogy is done with the mechanics of a spring for the hookean part and of a dashpot for the Newtonian part, leading to the representations in Fig. 1.34. We focus here on the Maxwell model.

A generalized writing of this model is :

$$\underline{\tau} + \lambda \frac{\partial \underline{\tau}}{\partial t} = -\mu \underline{\dot{\gamma}} \quad (1.78)$$

λ is defined as μ/G and is a time constant, usually called relaxation time. Eq. (1.78) is a differential equation, which in that case can be easily solved. In the case of a constant uniaxial imposed deformation γ_0 , with $\tau = \tau_0$ at $t = 0$, then :

$$\tau(t) = \tau_0 \exp(-\lambda_0 t) \quad (1.79)$$

The solution will depend on the flow imposed and the initial conditions. A general integral writing is given by :

$$\underline{\tau} = \int_{t'=-\infty}^{t'=t} \left[\frac{\eta_0}{\lambda_0} \exp\left(\frac{-(t-t')}{\lambda}\right) \right] \underline{\dot{\gamma}}(t') dt' \quad (1.80)$$

The part between brackets is called *relaxation modulus* or *fading bracket*.

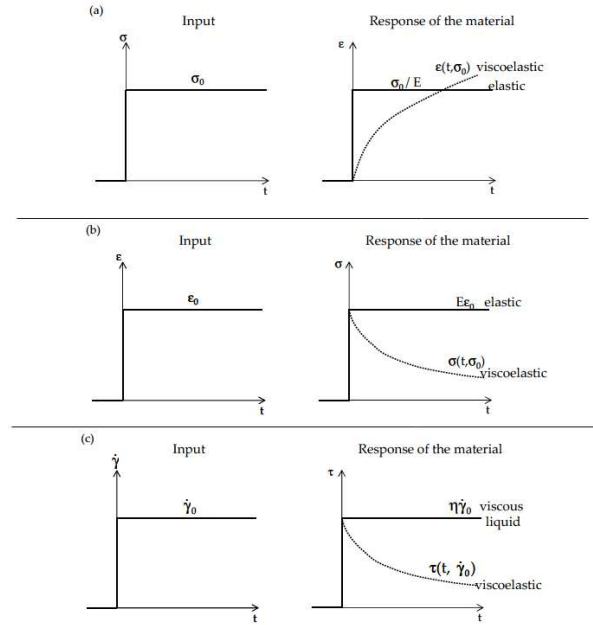


FIGURE 1.33 – (a) Comparison of the creep at a constant applied stress of an elastic and a viscoelastic material. (b) Comparison of the relaxation of an elastic and a viscoelastic material submitted to a constant strain. (c) Comparison of the responses of a viscous liquid and a viscoelastic material after the application of a constant strain rate (from Deplace (2008)).

Jeffreys model

The Maxwell model proposes a simple linear relation between τ and $\dot{\gamma}$. Jeffreys proposed to introduce a *retardation time* in the strain rate term, leading to the following model :

$$\tau + \lambda \frac{\partial \tau}{\partial t} = -\eta_0 \left(\dot{\gamma} + \lambda_r \frac{\partial \dot{\gamma}}{\partial t} \right) \quad (1.81)$$

This model is the starting point for numerous nonlinear viscoelastic models not discussed here.

Generalized Maxwell model

The models presented before show only one or two relaxation times. The relaxation time λ_0 of the Maxwell model allows to describe a wide range of behaviors from a purely viscous liquid ($\lambda_0 = 0$) to a purely elastic material (λ_0 tends to ∞). Unfortunately, our PSA show a wide range of relaxation times. An

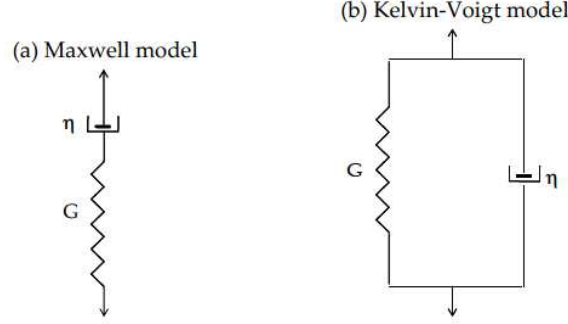


FIGURE 1.34 – Two mechanical models used to represent the viscoelastic behavior of polymers. (a) Maxwell model, (b) Kelvin-Voigt model.

easy way to describe that is to use a generalized Maxwell model, that is a sum of Maxwell models with different relaxation times. In this case, we can simply write the model as a sum of sub-models :

$$\underline{\tau}(t) = \sum_{k=1}^{\infty} \underline{\tau}_k(t) \quad (1.82)$$

$$\underline{\tau}_k + \lambda_k \frac{\partial \underline{\tau}_k}{\partial t} = -\eta_k \dot{\underline{\gamma}} \quad (1.83)$$

The integral expression is then :

$$\underline{\tau}(t) = \int_{t'=-\infty}^{t'=t} \left[\sum_{k=1}^{\infty} \frac{\eta_k}{\lambda_k} \exp\left(\frac{-(t-t')}{\lambda_k}\right) \right] \dot{\underline{\gamma}}(t') dt' \quad (1.84)$$

With this approach, it is possible to describe most of the behaviors encountered in the linear regime by using enough modes. For simulations for example, adding numerous parameters will help to capture complex phenomena, even if the parameters do not have a physical meaning.

Generalized linear viscoelastic model

Finally, a widely generalized model can be written using a relaxation modulus that will be defined by different models :

$$\underline{\tau}(t) = \int_{t'=-\infty}^{t'=t} G(t-t') \dot{\underline{\gamma}}(t') dt' \quad (1.85)$$

$G'(t-t')$ is the relaxation modulus, and can be defined as the sum of Maxwell models (leading to the generalized Maxwell model). Nevertheless, all these models will fail at large deformation as $\underline{\tau}$ is simply proportional to $\dot{\underline{\gamma}}(t')$. In this domain, we will need to introduce some non-linearity in our models.

Upper Convected Maxwell (UCM) model

The Maxwell model only offers linear dependency of stress and strain. To better characterize $\underline{\tau}$ at large deformation, we need to take into account that the materials store elastic energy in a non-linear way in the flowing liquid. This is integrated in the Upper Convected Maxwell (UCM) model. The way it is constructed is well described in the *Dynamics of Polymeric Fluids* book (Bird et al., 1977). Besides, Deplace (2008) described well the admissibility of this model in her thesis. The principle is to introduce a *convected derivative* that will introduce non linear dependence of stress and strain. This derivative is taken with respect to a coordinate system moving with velocity \underline{v} , instead of a simple time derivative. This convected derivative $\underline{\tau}_{(1)}$ is defined as :

$$\underline{\tau}_{(1)} = \frac{\partial \underline{\tau}}{\partial t} + \underline{v} \cdot \nabla \underline{\tau} - (\nabla \underline{v})^T \cdot \underline{\tau} - \underline{\tau} \cdot (\nabla \underline{v}) \quad (1.86)$$

Thus, the UCM model is described by :

$$\underline{\tau} + \lambda_0 \underline{\tau}_{(1)} = -\eta_0 \dot{\underline{\gamma}} \quad (1.87)$$

Convected models can be defined for all the linear models discussed before : the Jeffreys model can be extended to a Convected Jeffreys model and of course, the UCM model can be generalized by summing UCM sub-modes.

Giesekus model

While the UCM model can describe non-linear features of viscoelastic materials, it has no parameter to capture shear-thinning or shear thickening. Giesekus proposed to add a quadratic term in the UCM model and therefore introduces a new parameter α (Giesekus, 1982) :

$$\underline{\tau} + \lambda_0 \underline{\tau}_{(1)} + \frac{\alpha \lambda_0}{\eta_0} [\underline{\tau} \cdot \underline{\tau}] = -\eta_0 \dot{\underline{\gamma}} \quad (1.88)$$

Phan-Thien Tanner (PTT) model

The Giesekus model is really efficient but has the same limitation as the Gent model discussed in the elastic solids part : it diverges for a high strain rate. In the same approach as Seitz et al., Phan-Thien and Tanner replaced the diverging term by an exponential one, allowing to describe the same physics without getting the mathematical problems of the previous model (Phan-Thien, 1978), and added a term dependent on a parameter ξ describing the flow variation. The PTT model can be written as :

$$\exp\left(-\epsilon \frac{\lambda}{\eta} Tr \underline{\tau}\right) \underline{\tau} + \frac{\xi}{2} \lambda (gd \cdot \underline{\tau} + \underline{\tau} \cdot \dot{\underline{\gamma}}) + \lambda \underline{\tau}_{(1)} = -\eta \dot{\underline{\gamma}}, \quad (1.89)$$

Combined models : the example of the Deplace model

This section would not be complete without discussing the possible association between different models discussed above. Indeed, each model has its limitations and cannot describe the whole behavior of complex polymeric materials used as PSAs. For example, a PTT model does not show hardening due to the finite extension of a network. One good example of this approach is the one developed by Deplace et al. (2009a). They associate a UCM model in parallel with an elastic Gent model to capture the hardening behavior. In that case, the constitutive equation is simply the sum of the viscoelastic and the elastic contributions :

$$\tau = \tau_{UCM} + \tau_{Gent} \quad (1.90)$$

While this model fits well tensile data on waterborne nanostructured adhesives for a given strain rate, it does not fit well experiments at different strain rates. Nevertheless, this general approach allows us to finely define a model depending on the characteristics of our materials.

As it was discussed in this part, the first difficulty in modeling polymeric materials used as PSAs is to choose the correct approach to fit the experimental data. The model selected should lead to parameters predicting the adhesive behavior of materials, which involves deformations and flows with very complex transient kinematics, from their mechanical properties characterized in simple steady-state flows. Especially, a good model can lead to a better understanding of the phenomena controlling the transitions in debonding mechanisms and maximizing the energy dissipated during the debonding of PSAs. A previously used approach is to use models able to catch most of the behavior of the materials in one geometry to simulate the debonding processes. This is the approach developed by partners of the MODIFY EU project in Patras, from the groups of Vlas Mavrantzas and John Tsamopoulos. This approach has the limitation that the fitting parameters of the model cannot be directly interpreted physically and related to structural parameters of the material.

In this thesis, we will show that it is possible to define a simple model, which has a physical meaning and is able to fit the behavior of model PSAs over a range of strain rate in uniaxial deformation. The parameters obtained will be linked to adhesion properties of our materials.

Bibliographie

- Agirre, A., Nase, J., Degrandi, E., Creton, C., and Asua, J. M. (2010). Improving adhesion of acrylic waterborne PSAs to low surface energy materials : Introduction of stearyl acrylate. *Journal of Polymer Science Part A : Polymer Chemistry*, 48(22) :5030–5039.
- Aubrey, D. W. and Ginosatis, S. (1981). Peel adhesion behaviour of carboxylic elastomers. *The Journal of Adhesion*, 12(3) :189–198.
- Bellamine, A., Degrandi, E., Gerst, M., Stark, R., Beyers, C., and Creton, C. (2011). Design of nanostructured waterborne adhesives with improved shear resistance. *Macromolecular Materials and Engineering*, 296(1) :31–41.
- Bird, R. B., Armstrong, R. C., and Hassager, O. (1977). *Dynamics of Polymeric Liquids*. John Wiley Sons, London.
- Carelli, C., D’Alplace, F., Boissonnet, L., and Creton, C. (2007). Effect of a gradient in viscoelastic properties on the debonding mechanisms of soft adhesives. *The Journal of Adhesion*, 83(5) :491.
- Chan, H.-K. and Howard, G. J. (1978). Structure-property relationships in acrylic adhesives. *The Journal of Adhesion*, 9(4) :279–304.
- Chiche, A., Dollhofer, J., and Creton, C. (2005). Cavity growth in soft adhesives. *Eur. Phys. J. E*, 17 :389–401.
- Cogswell, F. N. (1972). Measuring the extensional rheology of polymer melts. *Transactions of the Society of Rheology*, 16(3) :383–403.
- Colby, R. and Rubinstein, M. (2003). *Polymer Physics*. Oxford University Press, USA.
- Cox, W. P. and Merz, E. H. (1958). Correlation of dynamic and steady flow viscosities. *Journal of Polymer Science*, 28(118) :619–622.
- Creton, C. (2003). Pressure-sensitive adhesives : an introductory course. *MRS bulletin*, 28(6) :434–439.
- Creton, C. and Fabre, P. (2002). *The Mechanics of Adhesion*, chapter 14, pages 535–576. Elsevier.
- Creton, C., Hooker, J., and Shull, K. R. (2001). Bulk and interfacial contributions to the debonding mechanisms of soft adhesives : extension to large strains. *Langmuir*, 17(16) :4948–4954.
- Crosby, A. J., Shull, K. R., Lakrout, H., and Creton, C. (2000). Deformation and failure modes of adhesively bonded elastic layers. *Journal of Applied Physics*, 88(5) :2956–2966.
- Dahlquist, C. (1969). *Pressure-sensitive adhesives*. Marcel Dekker : New York.

- Dealy, J. (2010). Weissenberg and Deborah numbers—their definition and use. *Rheol. Bull*, 79(2) :14–18.
- Degrandi, E. (2009). *Latex Hybrides Urethane/Acrylique Pour Applications Adhésives*. PhD thesis, Université Pierre et Marie Curie.
- Deplace, F. (2008). *Waterborne nanostructured Adhesives*. PhD thesis, Université Pierre et Marie Curie.
- Deplace, F., Carelli, C., Langenfeld, A., Rabjohns, M. A., Foster, A. B., Lovell, P. A., and Creton, C. (2009a). Controlled sparse and percolating cross-linking in waterborne soft adhesives. *ACS Appl. Mater. Interfaces*, 1(9) :2021–2029.
- Deplace, F., Carelli, C., Mariot, S., Retsos, H., Chateauminois, A., Ouzineb, K., and Creton, C. (2009b). Fine tuning the adhesive properties of a soft nanostructured adhesive with rheological measurements. *The Journal of Adhesion*, 85(1) :18–54.
- Derks, D., Lindner, A., Creton, C., and Bonn, D. (2003). Cohesive failure of thin layers of soft model adhesives under tension. *Journal of Applied Physics*, 93(3) :1557–1566.
- Doi, M. and Edwards, S. F. (1978). Dynamics of concentrated polymer systems. part 2.—molecular motion under flow. *J. Chem. Soc., Faraday Trans. 2*, 74 :1802–1817.
- Gent, A. N. (1996). A new constitutive relation for rubber. *Rubber Chemistry and Technology*, 69(1) :59.
- Giesekus, H. (1982). A simple constitutive equation for polymer fluids based on the concept of deformation-dependent tensorial mobility. *Journal of Non-Newtonian Fluid Mechanics*, 11 :69 – 109.
- Gower, M. D. and Shanks, R. A. (2004). The effect of varied monomer composition on adhesive performance and peeling master curves for acrylic pressure-sensitive adhesives. *Journal of Applied Polymer Science*, 93(6) :2909–2917.
- Halary, J., F., L., and L., M. (2011). *Polymer Materials*. Wiley.
- Hui, C.-Y., Glassmaker, N. J., and Jagota, A. (2005). How compliance compensates for surface roughness in fibrillar adhesion. *The Journal of Adhesion*, 81(7-8) :699–721.
- Josse, G., Sergot, P., Creton, C., and Dorget, M. (2004). Measuring interfacial adhesion between a soft viscoelastic layer and a rigid surface using a probe method. *J. Adhesion*, 80 :87–118.
- Jovanovic, R. and Dubé, M. A. (2004). Emulsion-based pressure-sensitive adhesives : A review. *Journal of Macromolecular Science, Part C : Polymer Reviews*, 44(1) :1–51.

- Keddie, J. L. (1997). Film formation of latex. *Materials Science and Engineering : R : Reports*, 21(3) :101 – 170.
- Lakrout, H., Sergot, P., and Creton, C. (1999). Direct observation of cavitation and fibrillation in a probe tack experiment on model acrylic pressure-sensitive adhesives. *The Journal of Adhesion*, 69(3) :307.
- Laureau, C., Vicente, M., Barandiaran, M. J., Leiza, J. R., and Asua, J. M. (2001). Effect of the composition profile of 2-ethyl hexyl acrylate/methyl methacrylate latex particles on adhesion. *Journal of Applied Polymer Science*, 81(5) :1258–1265.
- Lindner, A., Lestriez, B., Mariot, S., Creton, C., Maewis, T., Lühmann, B., and Brummer, R. (2006). Adhesive and rheological properties of lightly crosslinked model acrylic networks. *The Journal of Adhesion*, 82(3) :267–310.
- Lindner, A., Maewis, T., Brummer, R., Lühmann, B., and Creton, C. (2004). Sub-critical failure of soft acrylic adhesives under tensile stress. *Langmuir*, 20 :9156.
- Maia, J., Andrade, R., and Harris, P. (2012). Controlled stress extensional rheometer.
- Marin, G. and Derail, C. (2006). Rheology and adherence of pressure-sensitive adhesives. *The Journal of Adhesion*, 82(5) :469–485.
- Maugis, D. and Barquins, M. (1978). Fracture mechanics and the adherence of viscoelastic bodies. *Journal of Physics D : Applied Physics*, 11(14) :1989.
- Meissner, J. and Hostettler, J. (1994). A new elongational rheometer for polymer melts and other highly viscoelastic liquids. *Rheologica Acta*, 33 :1–21.
- Mooney, M. (1940). A theory of large elastic deformation. *Journal of Applied Physics*, 11(9) :582–592.
- Nase, J., Creton, C., Ramos, O., Sonnenberg, L., Yamaguchi, T., and Lindner, A. (2010). Measurement of the receding contact angle at the interface between a viscoelastic material and a rigid surface. *Soft Matter*, 6 :2685–2691.
- Nase, J., Lindner, A., and Creton, C. (2008). Pattern Formation during Deformation of a Confined Viscoelastic Layer : From a Viscous Liquid to a Soft Elastic Solid. *Phys. Rev. Lett.*, 101 :074503.
- Odian, G. (2004). *Principles of polymerization*. John Wiley & Sons.
- Peykova, Y., Guriyanova, S., Lebedeva, O. V., Diethert, A., Müller-Buschbaum, P., and Willenbacher, N. (2010). The effect of surface roughness on adhesive properties of acrylate copolymers. *Int. J. Adhes. Adhes.*, 30 :245–254.

- Peykova, Y., Lebedeva, O. V., Diethert, A., Muller-Buschbaum, P., and Willenbacher, N. (2012). Adhesive properties of acrylate copolymers : Effect of the nature of the substrate and copolymer functionality. *International Journal of Adhesion and Adhesives*, 34(0) :107–116.
- Phan-Thien, N. (1978). A nonlinear network viscoelastic model. *Journal of Rheology*, 22(3) :259.
- Poivet, S., Nallet, F., Gay, C., and Fabre, P. (2003). Cavitation-induced force transition in confined viscous liquids under traction. *Europhysics Letters (EPL)*, 62(2) :244–250.
- Poivet, S., Nallet, F., Gay, C., Teisseire, J., and Fabre, P. (2004). Force response of a viscous liquid in a probe-tack geometry : Fingering versus cavitation. *The European Physical Journal E*, 15(2) :97–116.
- Roos, A. and Creton, C. (2005). Effect of the presence of diblock copolymer on the nonlinear elastic and viscoelastic properties of elastomeric triblock copolymers. *Macromolecules*, 38(18) :7807–7818.
- Rubinstein, M. and Panyukov, S. (1997). Nonaffine deformation and elasticity of polymer networks. *Macromolecules*, 30(25) :8036–8044.
- Rubinstein, M. and Panyukov, S. (2002). Elasticity of polymer networks. *Macromolecules*, 35(17) :6670–6686.
- Satas, D. (1989). *Handbook of pressure sensitive adhesive technology, 2nd Edition*. Van Nostrand Reinhold.
- Schweizer, T. (2000). The uniaxial elongational rheometer rme six years of experience. *Rheologica Acta*, 39 :428–443.
- Seitz, M. E., Martina, D., Baumberger, T., Krishnan, V. R., Hui, C.-Y., and Shull, K. R. (2009). Fracture and large strain behavior of self-assembled triblock copolymer gels. *Soft Matter*, 5(2) :447.
- Sentmanat, M., Wang, B. N., and McKinley, G. H. (2005). Measuring the transient extensional rheology of polyethylene melts using the ser universal testing platform. *Journal of Rheology*, 49(3) :585–606.
- Smith, W. V. and Ewart, R. H. (1948). Kinetics of emulsion polymerization. *The Journal of Chemical Physics*, 16(6) :592–599.
- Tirumkudulu, M., Russell, W. B., and Huang, T. J. (2003). On the measurement of “tack” for adhesives. *Phys. Fluids*, 15 :1588–1605.
- Tobing, S. D. and Klein, A. (2001). Molecular parameters and their relation to the adhesive performance of acrylic pressure-sensitive adhesives. *Journal of Applied Polymer Science*, 79(7) :2230–2244.

- Webber, R. E., Shull, K. R., Roos, A., and Creton, C. (2003). Effects of geometric confinement on the adhesive debonding of soft elastic solids. *Physical Review E*, 68(2) :021805.
- Yamaguchi, T., Koike, K., and Doi, M. (2007). In situ observation of stereoscopic shapes of cavities in soft adhesives. *Europhys. Lett.*, 77 :64002.
- Zosel, A. (1985). Adhesion and tack of polymers : Influence of mechanical properties and surface tensions. *Colloid Polym. Sci.*, 263 :541–553.
- Zosel, A. (1989). Adhesive failure and deformation behaviour of polymers. *The Journal of Adhesion*, 30(1-4) :135–149.

Chapitre 2

Acrylic polymers as model materials

Contents

1.1 Adhesion and Adhesives	6
1.1.1 Adhesion	6
1.1.2 Pressure-sensitive Adhesives (PSAs)	7
1.2 Acrylic Polymers as PSAs	9
1.2.1 Synthesis of acrylic polymers by free radical polymerization	9
1.2.2 Film formation	17
1.3 Mechanical characterization and properties of PSAs	18
1.3.1 Linear Viscoelastic properties	19
1.3.2 Non-linear viscoelastic properties	21
1.4 Adhesive characterization and debonding mechanisms of PSA	28
1.4.1 Characterisation of adhesive properties of PSA	28
1.4.2 Debonding mechanisms	31
1.4.3 Limits of actual PSA systems	35
1.5 Modeling elastic solids, viscous fluids and viscoelastic materials	36
1.5.1 Elastic solids and elastomers	38
1.5.2 Viscous fluids	42
1.5.3 Viscoelasticity	44

2.1 Introduction

As stated in the last chapter, acrylic polymers are commonly used for application as PSAs. In order to get the best properties for the applications targeted, the architecture of the polymer can be complex. Moreover, they can be formulated with tackifying resins to adjust the network properties (Lindner et al., 2006). Recent advances in emulsion polymerisation techniques have enabled the preparation of acrylic PSAs with a fine control on the properties of the base polymer (Tobing and Klein, 2001; Deplace, 2008; Degrandi, 2009; Bellamine et al., 2011), while avoiding the use of any volatile organic component (VOC), strongly limited in the European Union under the REACH regulation. In order to get systems that could mimic behavior of industrial PSAs while being relatively easy to model, it was chosen in our European project to work with model acrylic polymers.

Simple model systems that can be used as models for PSA have been previously studied in our laboratory. PDMS with different cross-linking degrees was used, showing an interesting control of the viscoelastic properties, but low dissipation due to the low T_g of the material (Nase et al., 2008). For acrylic PSAs obtained from solution polymerization, the link between their mechanical properties and their adhesion performances were studied (Lindner et al., 2006). These different findings, completed by others, lead to specifications that were given to DOW Chemical Company. The team of Ralph Even, based in Midland, synthesized two generations of materials with a wide range of properties.

In this chapter, we present the results of their mechanical characterization and focus on uniaxial tests with two different strain rate profiles, extensional rheology, generally used for flowing systems, and tensile tests, generally used for solid materials. We also present a detailed adhesive characterization of these materials and discuss the transition between the different debonding modes discussed in the previous chapter.

2.2 Specifications of the model materials

After discussions between the partners of the MODIFY project, the specifications given to DOW Chemical Company were :

- latexes made from emulsion polymerization,
- controlled random monomer composition : 98.1% of N-butyl acrylate(BA) and 1.9% of acrylic acid (AA),
- linear polymer architecture (no or little branching),
- no cross-linking,
- high M_w ,

As discussed in the section 1.4.3 p.35, many general purpose PSAs are nowadays synthesized in aqueous media for environmental and economic reasons. This synthesis method, without any volatile solvent, is ideally suited to synthesize

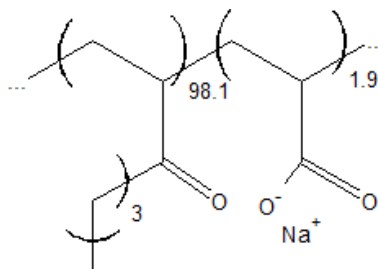


FIGURE 2.1 – Structure of the poly(BA-co-AA) targeted. The BA and AA are randomly distributed

the high M_w and often lightly cross-linked polymers required by the application and produces high solids content low viscosity dispersions without the drawbacks of the high viscosities encountered in solution polymerization.

The composition of the 98.1% of n-Butyl acrylate (BA) and 1.9% of acrylic acid (AA) (see fig 2.1) random copolymer was selected to be the simplest possible that shows a representative PSA behavior. Only one main monomer was used : butyl acrylate, which gives a T_g in the targeted range (around -40°C). In order to be efficient, PSAs need to have a wide range of relaxation times, to be able to show good properties over a wide range of strain rates and temperatures. Therefore, a reasonably high polydispersity of the polymers used as PSAs is not only acceptable but desirable and no attempt to reduce it was made in our model system.

In applications PSAs are usually crosslinked to obtain a good resistance to creep and hence to sustain shear stresses over prolonged periods of time without failure.. Yet the polymers targeted are not cross-linked. needed a high M_w to have PSA properties. Acrylic polymers with long chains will have an entangled structure where entanglements play the role of temporary crosslinks and will thus increase the elastic modulus in a range of frequencies. Contrary to cross-linked network, the response of an entangled network should depend strongly on the applied strain rate.

The addition of acrylic acid is essential since it provides colloidal stability in the latex. After drying, it can both associate with itself and modify the rheological properties of the polymer and form bonds with the surface increasing interfacial adhesion : More specifically, as the carboxylate groups ($pH \approx 8$) are hydrophilic (as opposed to butyl acrylate), these groups tend to migrate at the interface of each latex particle during the synthesis. (Fig. 2.2). During the drying of the latex, particles approach and coalesce (see section 1.2.2, p.17 for more details). Thus, the acrylic acid groups create strongly interacting interfaces between particles and can form dipolar bonds inside each particle , resulting in more cohesion in the material once it is dried. Moreover, these ionic groups offer possible interactions with the adherend surface (Aubrey and Ginosatis, 1981).

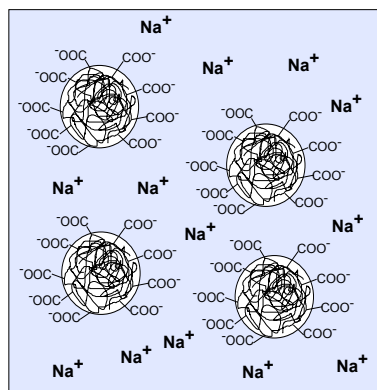


FIGURE 2.2 – Structure of a latex of Poly(BA-co-AA). The carboxylate groups ($pH \approx 8$) migrate to the interface of particles

Due to the high transfer rate of radicals to the polymer during the polymerization, a high degree of branching is usually obtained in acrylic polymers. These branchings create a complex architecture and thus a complex viscoelastic signature, difficult to characterize. To design a model system as simple as possible, we decided to adapt the synthesis conditions to synthesize high Mw polymers as little branched as possible.

To obtain model materials with varying viscoelastic properties, it was decided to use the average M_w as a control parameter. This can be easily done by using chain transfer agent during the synthesis. Indeed, during a polymer synthesis, the amount of active chains can be controlled by the introduction of chain transfer agents (CTA). By increasing the proportion of active chains, the total number of chains obtained will be more important. Thus, the global M_w of the polymer will be lower.

2.3 Characterization of the polymers synthesized

2.3.1 Molecular weight and gel content

Two series of polymers were synthesized with slightly different synthesis conditions : the A series and B series. Within each series the polymerization conditions were kept identical but different amounts of chain transfer agent (CTA) were used . In the rest of the manuscript, the polymers will be named with the following nomenclature : $X1111$, where X is the series (A or B) and 1111 is M_w of the material. The main difference between these two series is the temperature of the synthesis. The B series was synthesized in different conditions, limiting even more the number of branchings compared to A series (Plessis et al.,

2003). Molecular weights of the two series were characterized by Gel Permeation chromatography (GPC) at the DOW Chemical Company. \overline{M}_n and \overline{M}_w absolute values were obtained from coupled refractive index (RI) and multi-angle light scattering (MALS) detection. The gel content was calculated from the proportion of polymer failing to go through the column as it failed to dissolve in the operating solvent. The part that could be trapped in the GPC column was neglected.

Polymer	CTA (%)	Mn (kg/mol)	Mw (kg/mol)	PDI (-)	$d_{particles}$ (nm)	Gel content (%)
A1570	-	611	1572	2.57	400	-
A1070	0.05	466	1065	2.28	403	-
A650	0.1	298	651	2.18	400	-

TABLE 2.1 – Molecular weights, polydispersity index (PDI), diameter of latex particles and gel content for the A series.

The A series (cf Tab 2.1) shows M_w from 651kg/mol up to 1572kg/mol, and is expected to lead to a wide range of viscoelastic properties. None of these polymers showed any gel content, in agreement with the fact that they are not cross-linked.

Polymer	CTA (%)	Mn (kg/mol)	Mw (kg/mol)	PDI (-)	$d_{particles}$ (nm)	Gel content (%)
Bg1110	-	329	1115	3.39	368	33
B1080	0.05	342	1077	3.14	380	-
B600	0.1	248	595	2.39	378	-
B440	0.15	180	437	2.43	365	-
B380	0.2	172	382	2.22	374	-

TABLE 2.2 – Molecular weights, polydispersity index (PDI), diameter of latex particles and gel content for the B series.

The B series was realized in order to further decrease the number of branchings per chain. Their architecture is thus a bit different from the A series. It is expected that fewer branches per chain are created than for A, but once obtained, they will grow for a longer time.

The range of M_w has also been expanded and varies from 374kg/mol up to 1115kg/mol (cf tab ??). The polydispersity obtained is a bit higher than on the A series. In this series, one polymer, named Bg1110 has a gel content of 32%. The presence of gel can be surprising since no cross-linker has been used. Nevertheless, networks can be created by co-termination between a branched chain and an activated one (see fig. 2.3). Adding a small proportion of CTA will lead to more active growing chains, therefore less radicals reacting on the middle of chains. This explains the difference between Bg1110 and B1080, where adding 0.05% of CTA lead to a similar M_w , but no gel.

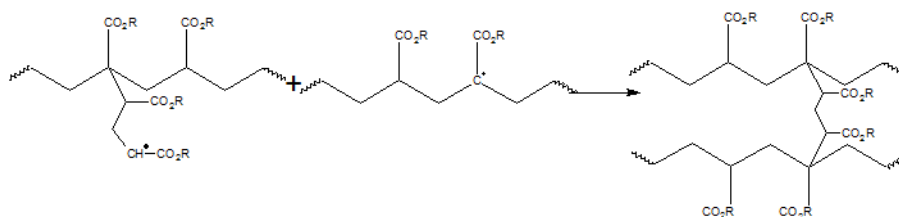


FIGURE 2.3 – Reaction between a growing branch and an activated chain to create partial networks

2.3.2 Architecture characterization

In order to study the linearity of the chains obtained, the GPC results are compared with data obtained for linear polystyrene. Fig. 2.4 and 2.5 show absolute molecular weights derived from RI and MALS data versus elution time. The same data is plotted for a series of linear polystyrene molecular weight standards (in gray). During GPC testing, longer chains get out of the columns faster than short ones. Thus, as seen in these figures, high M_w corresponds to low elution times. For the B series (Fig. 2.4), The data is essentially linear and well correlated to that of the standards for the elution time range over which most of the polymers gets out of the column. This is indicative of a distribution of polymer chains having a consistent degree of overall branching for all molecular weights. If we assume that the linear polystyrene standards represent a good model for solvent/polymer interactions of the experimental polymers, we can conclude that our materials have little or no long chain branching. The same data for A series (Fig.2.5) shows less correlation between the experimental polymers and the standards, as well as less consistency of slope within the experimental polymers, while still being lightly branched. It can be concluded that the B series polymers are less branched and more regularly so than the A series. It has to be noted that this characterization does not give any quantitative data on the average length of the branchings.

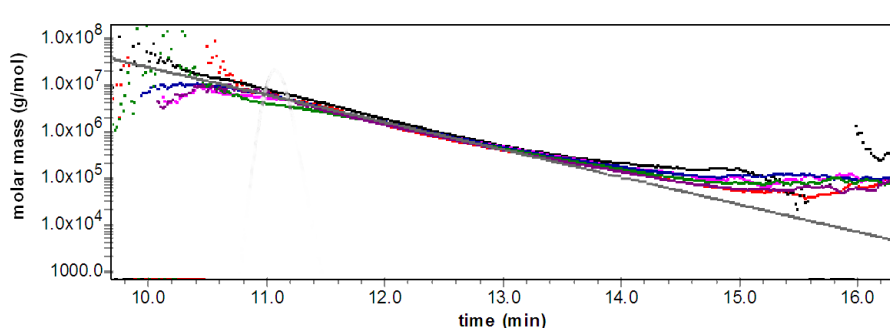


FIGURE 2.4 – Molar mass versus elution time for B series and for linear polystyrene molecular weight standard (gray).

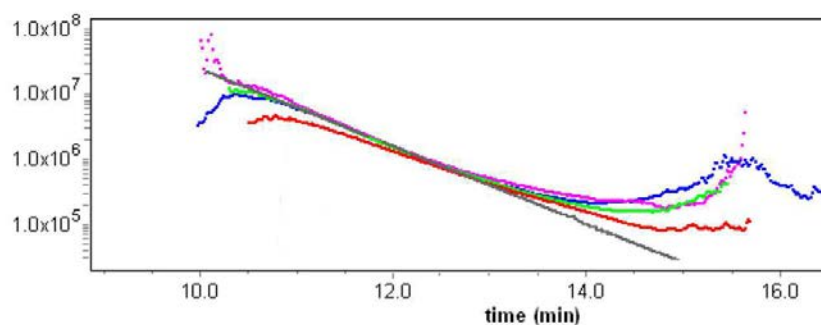


FIGURE 2.5 – Molar mass versus elution time for A series and for linear polystyrene molecular weight standard (gray).

For the adhesion and rheological study of these materials, B600, B440 and B380 were considered too low molecular weight to be representative of PSAs . So, five of the synthesized model materials have been fully characterized mechanically : A1570, A1070, A650, Bg1110 and B1080.

2.4 Mechanical characterization

2.4.1 Sample preparation

For rheological and tensile tests, relatively thick films were necessary ($\approx 600 \mu\text{m}$). In order to obtain them, latexes were cast in silicone molds. The volume of solution was determined in order to get the desired dry thickness by the simple formula :

$$V_{cast} = \frac{L \times w \times h}{V\%} \quad (2.1)$$

where L is length of the mould, w the width of the mould, h the targeted thickness and $V\%$ the solid content of the sample.

The samples were dried during a week at room temperature, followed by 5 min at 110°C in an oven. Samples were then released from the molds and protected between two sheets of release paper. Different sizes and geometries of samples were then cut from it (disks for rheology, rectangular for tensile tests).

2.4.2 Linear viscoelastic characterization

The viscoelastic properties in the linear regime of our polymers have been characterized by the team of Christian Bailly, from the Université Catholique de Louvain (UCL). The small amplitude oscillatory shear flow (SAOS) was performed with a strain-controlled rheometer (ARES, TA Instruments) with a standard parallel plate geometry at frequencies between 10^2 rad/s to 10^{-2} rad/s and at temperatures between -50°C to 90°C . The master curves were calculated

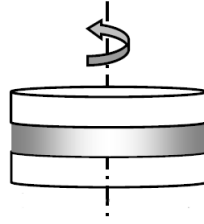


FIGURE 2.6 – Small amplitude oscillatory shear flow geometry

at 30°C by applying a time-temperature superposition (TTS) horizontal shift parameter.

2.4.3 Characterization of the non-linear properties

In order to characterize the non-linear viscoelastic properties of our samples, tensile tests and extensional rheology tests were carried out on our samples. A complete discussion of the geometries of these two tests has been presented in the previous chapter, section 1.3.2, p.21. We will focus here on the set-up used in our laboratory for these tests and recall the important relations about strains in the two experiments.

Tensile tests

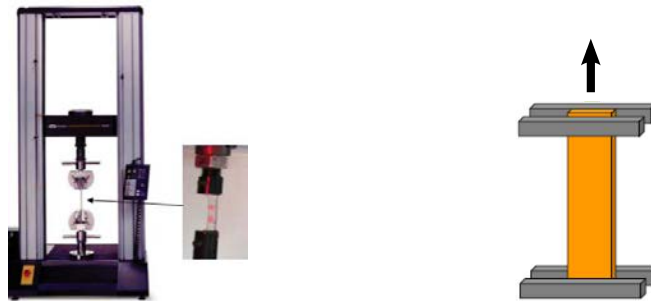


FIGURE 2.7 – Instron machine (left) used for tensile test experiments. A scheme of the geometry is represented (right).

Tensile tests were carried out in a standard tensile Instron equipment (5565) equipped with a non contact laser extensometer (SVE), allowing a precise measurement of the local strain near the center of the sample. The maximal range of displacement measured by the SVE is 200 mm : the machine can apply displacements up to 600 mm. We used a 10 N load cell, offering a resolution of 0.5 %. Samples had an average thickness of 600 μ m and a width of 5 mm. Precise dimensions were determined for each sample before the tests. The cross-head

velocity (kept constant) used was 15 mm/s and 1.5 mm/s for samples with an initial length between clamps of 15 mm. Thus, the nominal strain rate of these experiments were respectively 0.1 s^{-1} and 1 s^{-1} . To avoid slippage, samples were blocked by jaws closed with a dynamometric key (Torque : 25cN/m). Two white spots were drawn on the sample to follow the displacement with the laser extensometer. All tests were performed at room temperature. A minimum of three tests were carried out for each sample at a given strain rate to ensure reproducibility.

During the test, force and displacement from the cross-head were measured by the system. In addition the laser extensometer measured the displacement of the white spots. A comparison of the two nominal strains obtained from the cross-head and the extensometer ensured that no slippage occurred during these experiments.

In this experiment, the sample is stretched at a constant cross-head velocity. Thus, as explained in section 1.3.2 (p.21), the nominal strain rate is constant, and if we define $\alpha = v/l_0$ where v is the cross-head velocity and l_0 the initial length of the sample :

$$\begin{cases} \epsilon_N = \alpha t \\ \dot{\epsilon}_N = \alpha \end{cases} \quad (2.2)$$

Extensional rheology

In order to obtain uniaxial characterization at a constant hencky strain rate, tests were carried out with an extensional rheology device adapted to a rheometer (SER-2 and MCR-301 Anton Paar). The device consists of two counter-rotating drums with intermeshing gears and low-friction bearings. The rotational movement of the rheometer is directly transferred to the drums, which stretch the sample. The length of the sample $l(t)$ is kept constant, since it is the distance between the center of the two cylinders. As l and the rate of the cylinders rotation is constant, $\dot{\epsilon}_H$ is constant too.

All tests were performed at room temperature, with strain rates varying from 0.01s^{-1} to 1s^{-1} .

With the SER-2 device, the torque Γ measured on the drums can be converted to a force on the material by :

$$F(t) = \frac{\Gamma(t)}{2R} \quad (2.3)$$

Where R is the radius of one drum.

The instantaneous cross-sectional area $A(t)$ of the stretched material evolves exponentially with time

$$A(t) = A_0 \exp(-\dot{\epsilon}_H t) \quad (2.4)$$

With A_0 the initial cross-sectional area.

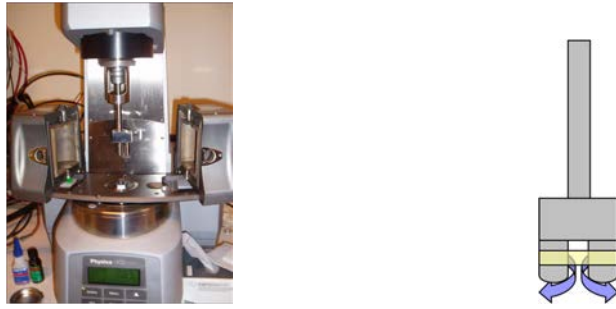


FIGURE 2.8 – SER-2 device adapted on MCR-301 rheometer from Anton Paar (left). A scheme of the geometry is represented (right).

The extensional viscosity $\eta_E^+(t)$ is given by :

$$\eta_E^+(t) = \frac{F(t)}{\dot{\epsilon}_H A(t)} \quad (2.5)$$

and can be represented as a function of time or ϵ_H . Otherwise, nominal and true stress are obtained simply by :

$$\begin{cases} \sigma_N = \frac{F(t)}{A_0} \\ \sigma_T = \frac{F(t)}{A(t)} \end{cases} \quad (2.6)$$

2.5 Adhesive Characterization

2.5.1 Sample preparation

For adhesion tests, thin films ($\approx 100\mu m$) coated on glass slides were made : latex solution were deposited at an extremity of the glass slide. The solution was then carefully coated with a home-made coater until the solution was deposited on all the slide. Films were left to dry for 24 hours at room temperature (cf Fig. 2.9) followed by 2 min at $110^\circ C$ in an oven. After drying, the film became totally transparent.



FIGURE 2.9 – Sample preparation of a probe-tack film with a home-made coater (from left to right).

2.5.2 Probe-tack test

For all samples, adhesive properties were characterized with the well-known probe-tack test (Zosel, 1985). In Our version of this experiment, a 0.6 cm or 1 cm diameter cylindrical probe comes in contact with an adhesive layer until a given compressive pressure is reached. The probe motion is then stopped and after a controlled time, the probe is debonded from the adhesive at a constant velocity. The basic principle of the experiment and the data that can be obtained from it were discussed in section 1.4.1 (p.28). We will especially focus on the specific set-up used in our laboratory.

The set-up developed at the ESPCI allows the observation and recording from a top-view of the deformation of the adhesive during the debonding and the measurement of the actual contact area when small misalignments occur (see Fig. 2.10) (Lakrouit et al., 1999).

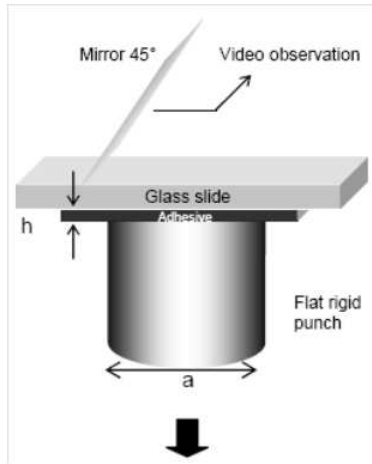


FIGURE 2.10 – Geometry of the probe-tack test.

In order to control the parallelism between the probe and the adhesive layer, a tripod system is fixed on the apparatus to set-up the alignment of the probe and the adhesive layer (see Fig. 2.11).

The force F was measured by a load cell ($250\text{N} \pm 0.5\text{N}$) and the displacement $d(t)$ with an LVDT extensometer (range 10mm , $\pm 0.5\mu\text{m}$). The initial adhesive layer thickness is h_0 , and is pulled by a probe of diameter a and area A_T . The nominal stress is simply given by

$$\sigma_N = \frac{F}{A_T}. \quad (2.7)$$

the nominal strain is simply given by :

$$\epsilon = \frac{d(t)}{h_0}. \quad (2.8)$$

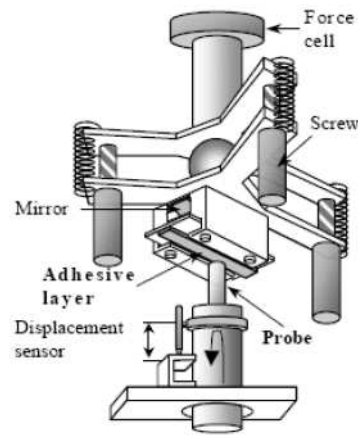


FIGURE 2.11 – Schematic of the probe-tack set-up with the representation of the tripod system used for the alignment of the adhesive layer with the probe

As it was presented in section 1.4.2 (p.31), different mechanisms can occur during the debonding of an adhesive during a probe-tack test, leading to three typical curves reminded on Fig. 2.12. Thus, the shape of the curve obtained leads to the mechanism which occurred during each experiment. The transition between interfacial crack propagation and bulk deformation can be detected by the presence of a plateau in the stress-strain curve, characteristic of a bulk deformation process. More precisely, the experiment is said with bulk deformation if a pronounced inflexion showing a start of a plateau is observable on the curve. The adhesive or cohesive failure is confirmed by the presence of adhesive on the probe or not, which is verified after each test.

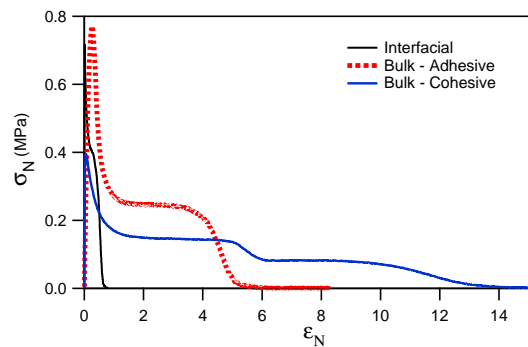


FIGURE 2.12 – Typical stress vs strain curve obtained from probe-tack tests with different mechanisms : interfacial crack propagation (black), bulk deformation leading to adhesive failure (red) or cohesive failure (blue).

A typical curve obtained in probe-tack test for a PSA is shown in Fig. 2.13. A number of parameters can be obtained from these curves : σ_f , stress at the beginning of the plateau when fibrillation occurs, ϵ_{max} , strain for which adhesive completely debonds from the probe and W_{adh} , adhesion energy. This last parameter is calculated as the integral of this curve multiplied by h_0 . In the case of interfacial crack propagation, no σ_f can be measured, but a change in inflexion can be observed after the peak : it corresponds to the beginning of the plateau, before crack propagation occurs at the interface. In that case, σ_f will be the nominal stress corresponding to this variation in curvature.

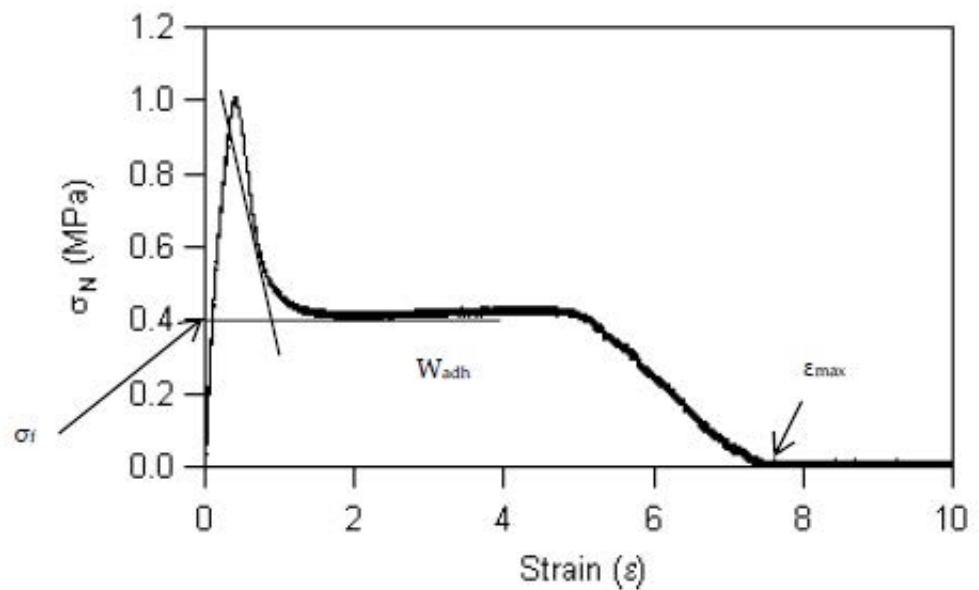


FIGURE 2.13 – Classical stress vs strain curve obtained from a probe-tack test

Stress-strain curves from probe-tack of our model adhesives were obtained on two surfaces with different surface energies, namely a stainless steel (SS) and a polyethylene (PE) surface. In order to obtain a perfectly smooth and reflective surface, the SS probe was mechanically polished. The PE probe was made using a standard plate of HDPE given by DOW, which was stuck on the top of a probe with a commercial Loctite glue. The SS surface can be qualified as a high adhesion surface, while PE is representative of lower adhesion surfaces encountered in applications.

2.6 Results and Discussions

2.6.1 Mechanical characterization

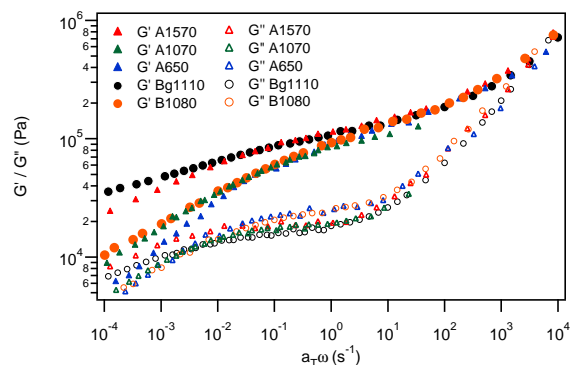


FIGURE 2.14 – Mastercurves of dynamic storage (G') and loss (G'') modulus as function of angular frequency ($a_T\omega$) for the five different materials at a reference temperature of 30°C .

Master curves of the dynamic storage (G') and loss (G'') modulus as function of angular frequency ($a_T\omega$) for the five different materials at a reference temperature of 30°C are given in Fig. 2.14. The curves were obtained by applying time-temperature superposition and it can be seen that the viscoelastic properties of the three materials are identical at frequencies larger than 10s^{-1} but significant differences are observed at low frequency. The materials display solid-like behavior over the frequency range tested and as expected, G' (omega) increases with M_w . A1570 and Bg1110 have very similar linear viscoelastic properties, while A650, A1070 and B1080 are significantly more viscoelastic at low frequency. No cross-over between G' and G'' was detected for any material, meaning that no terminal flow was observed with the range of accessible frequencies.

Differences between the materials are more pronounced in large strain (cf Fig. 2.15). Visual observation during the experiments showed that failure occurs by macroscopic flow for the less elastic materials, i.e. A650 and A1070. Strain hardening behavior characterizes the high molecular weight materials of the B series. While A1570 and Bg1110 are difficult to distinguish in the linear regime, the difference in architecture and the presence of a gel fraction in Bg1110 provides finite extensibility resulting in a different large-strain behavior. Interestingly, B1080 shows strain hardening while A1570 does not, even if B1080 has a lower M_w . This confirms that this behavior is due to the difference in architecture between the two series. The strain hardening is a signature of a longer life of the entangled structure, which is indeed visible in linear rheology for the Bg1110, but the comparisons between B1080 and A1570 is more puzzling. Figure 2.14 shows that at low frequency B1080 has a lower value of G' and appears to

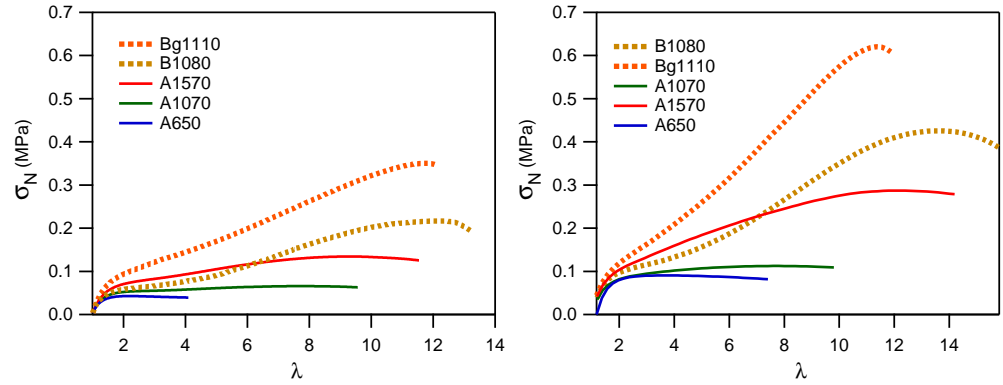


FIGURE 2.15 – Nominal Stress versus λ for the five different materials, at $\dot{\lambda} = 0.1s^{-1}$ (left) and $\dot{\lambda} = 1.0s^{-1}$ (right).

be closer to flow and yet at high strain rates it strain hardens in a much more pronounced way. This shows that the structure of the particles itself should be different for the two series.

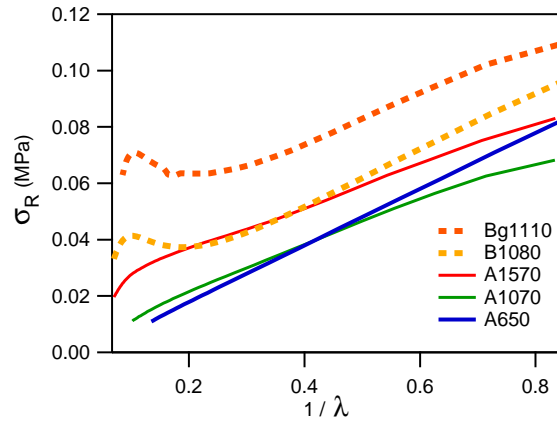


FIGURE 2.16 – Reduced Stress versus $1/\lambda$ for the five different materials, at $\dot{\lambda} = 1.0s^{-1}$.

Another way to study these curves is to plot them in the Mooney representation of the reduced stress σ_R versus $1/\lambda$, as discussed in section 1.3.2. Results are presented in Fig. 2.16. C_{soft} and C_{hard} parameters were extracted from these plots and are presented in Table 2.3. Roos and Creton have shown that these parameters can be approximately interpreted as contributions due to temporary and permanent crosslinks respectively (Roos and Creton, 2005).

C_{soft}/C_{hard} estimates the ratio between these two contributions.

As expected, no C_{hard} can be defined for the A series as they do not show any hardening due to permanent cross-links. C_{soft} clearly depends on M_w , due to the temporary bonds of to the entanglements and the stickers of AA. The value of A650 is especially high, confirmed by the higher slope observed in Fig.2.16. The ratio C_{soft}/C_{hard} shows that the B materials show a relatively hard behavior.

It has been shown that on high adhesion surface like stainless steel, a value of this ratio superior to 2 was needed to obtain good PSAs performances (Lindner et al., 2006)(Deplace et al., 2009)(Agirre et al., 2010). For lower adhesion surfaces like PE, more dissipation is needed, resulting in a targeted ratio higher. In our case, B1080 is in agreement with this criterion and should show good adhesive properties on stainless steel.

	$C_{soft}(kPa)$	$C_{hard}(kPa)$	$\frac{C_{soft}}{C_{hard}}$
A650	101.2	-	-
A1070	83.7	-	-
A1570	73.3	-	-
B1080	89.0	37.3	2.38
Bgl110	75.6	52.2	1.45

TABLE 2.3 – Values of the C_{soft} and C_{hard} viscoelastic parameters for the five materials for $\dot{\lambda} = 1s^{-1}$.

When studying the extensional rheology of a material, using the Cox-Merz rule (Cox and Merz, 1958) (discussed in section 1.3.2 p.21) can be useful. According to this rule, the steady state shear viscosity measured in the linear regime $\eta^*(\omega)$ at a given frequency is equal to the dynamic viscosity $\eta^+(\dot{\gamma})$ at a shear rate $\dot{\gamma}$ if one considers that $\dot{\gamma} = \omega$:

$$\eta(\dot{\gamma}) = \eta^*(\omega) \quad (2.9)$$

$$\eta^*(\omega) = \sqrt{\left(\frac{G'}{\omega}\right)^2 + \left(\frac{G''}{\omega}\right)^2} \quad (2.10)$$

Thus, we can compare the dynamic viscosity extrapolated from the steady state shear viscosity with the dynamic viscosity measured in the SER test. We expect that the dynamic viscosity measured will derive from the one predicted from steady state at large deformations, as other deformation mechanisms contribute. In order to compare shear experiments to elongation experiments, one has to multiply the viscosity obtained in shear η^* by a factor of three due to conservation of volume.

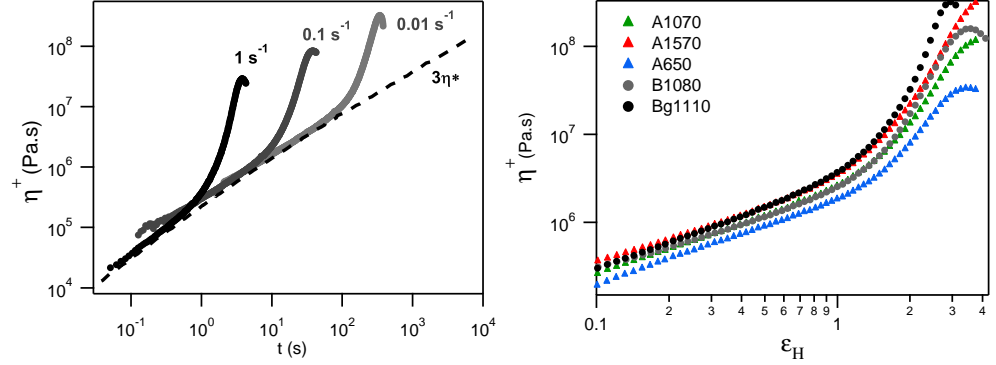


FIGURE 2.17 – Extensional viscosity as a function of time for A1070 (left) and as a function of the hencky strain for five different materials at $\dot{\epsilon}_H = 0.1s^{-1}$

Results are presented in Fig.2.17(left) for the A1070 material (similar observations are made for the other materials). Elongational viscosities taken from experiments at different strain rates agree with each other for short times (i.e small strains) which show that this domain is in the linear regime of the material. After a Hencky strain $\epsilon_H \approx 1.5$, η strongly diverges from $3\eta^*$, showing a strong increase of the stress due to the non-linear response of the material. As shown in Fig.2.17(right), all materials show a strong increase in the stress relative to the linear prediction at high strain.

While the tensile test, especially in the Mooney plot, showed clear differences between the A series and the B series with the presence of a strain hardening for the latter, the differences between the five materials are not as obvious in the case of elongational rheology, mainly due to a different way to present the results. Compared to a newtonian fluid, all materials show a "strain hardening", *e.g* an increase of its stress compared to the linear prediction due to the accumulation of elastic energy in the material that does not relax. However, the A series materials do not show any "strain hardening" in tensile test, *e.g* relative to the neo-hookean solid prediction, due to a finite extension of the chains.

The behavior observed in elongational rheology show that our materials are not purely linear, as it would in that case give no strain hardening when compared to newtonian fluid (Munstedt and Laun, 1979; Munstedt, 1980).

It is also interesting to compare tensile curves with the extensional rheology by plotting nominal stress σ_N vs nominal strain ϵ_N in linear and log scales for both experiments (see Fig.2.18). The results show good agreement between the two techniques for the small strain domain, while for values of nominal strain superior to 100%, the curves separate. This difference can first be explained by the different strain rate histories used in the two experiments. As we discussed in section 1.3.2 (p.21), an extensional rheology test is equivalent to a tensile test

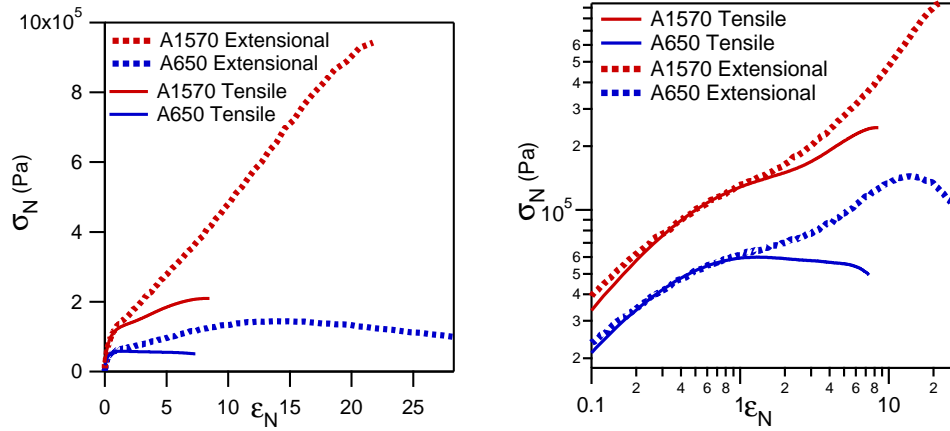


FIGURE 2.18 – Nominal stress vs Nominal Strain in linear scale (left) and log scale (right) for tensile test ($\dot{\epsilon}_N$ constant) and extensional rheology ($\dot{\epsilon}_H$ constant). The initial $\dot{\epsilon}_N$ and $\dot{\epsilon}_H$ are equal to $0.1s^{-1}$

with a cross-head velocity accelerating exponentially. Thus, for small strains, the tests can be considered as equivalent, whereas for large strains, the materials are stretched at a higher strain rate in extensional rheology, resulting in a higher stress and a more pronounced hardening. A1570 clearly shows a more pronounced hardening in extensional rheology, and A650 shows a slight hardening while macroscopic flow was observed in a tensile test.

In conclusion, our materials behave as viscoelastic solids with a wide range of properties, from a viscoelastic fluid behavior for A650, to a strain-hardening viscoelastic solid for Bg1110. This should translate to a broad range of adhesive properties and debonding mechanisms.

2.6.2 Adhesion characterization and debonding mechanisms

Experimental results

Curves obtained from probe-tack experiments on our materials with a stainless steel probe at a velocity of $100 \mu\text{m/s}$ are shown in Fig.2.19. We observe different shapes of curves corresponding to different debonding mechanisms, as discussed in section 2.5.2 with typical curves shown on Fig. 2.12 : in our case, Bg1110 moderate level of bulk deformation concluded by an interfacial crack propagation, B1080 and A1570 show a clear bulk deformation leading to an adhesive debonding while A650 and A1070 show a bulk deformation coupled with a cohesive debonding. A650 shows a particularly pronounced double-plateau shape, typical of liquid-like materials (Poivet et al., 2004).

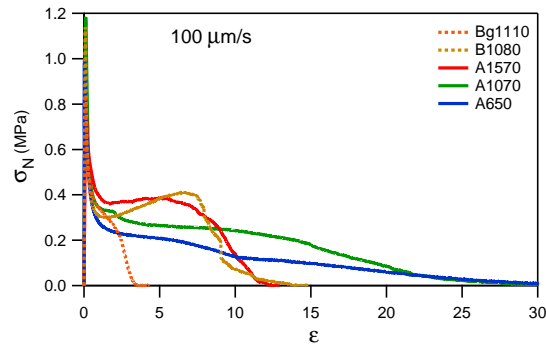


FIGURE 2.19 – Stress-Strain tack curves for the five different materials at debonding velocity of $100 \mu\text{m/s}$ against a stainless steel probe.

As shown in the previous section, the mechanical response of our materials is heavily dependent on deformation rate due to their uncross-linked nature. This can be confirmed by tests realized on our materials at four pulling velocities : $1 \mu\text{m/s}$, $10 \mu\text{m/s}$, $100 \mu\text{m/s}$ and $1000 \mu\text{m/s}$. The results are presented in Fig.2.20. An increase in the pulling velocity leads to an increase in the stress of the plateau σ_f . Interestingly, we see that, while A650 shows the same characteristic curve shape at all rates (even if an adhesive debonding is experimentally observed on the probe at $1000 \mu\text{m/s}$), the other materials show different shapes, proving that the debonding mechanism is dependent of debonding rate for our materials, confirming the influence of viscoelasticity on this. A1070 shows a clear transition between $100 \mu\text{m/s}$ and $1000 \mu\text{m/s}$ from cohesive to adhesive debonding (confirmed by experimental observation). The same transition is observed around $10 \mu\text{m/s}$ for A1570. Finally, the transition between an interfacial crack propagation and bulk deformation is observed for Bg1110 at $10 \mu\text{m/s}$. All experiments but one show a bulk deformation. On the other hand, these materials offer us a great opportunity to study the transition between the different mechanisms which we will discuss later.

Influence of the debonding rate (A650 / A 1070 / Bg1110).

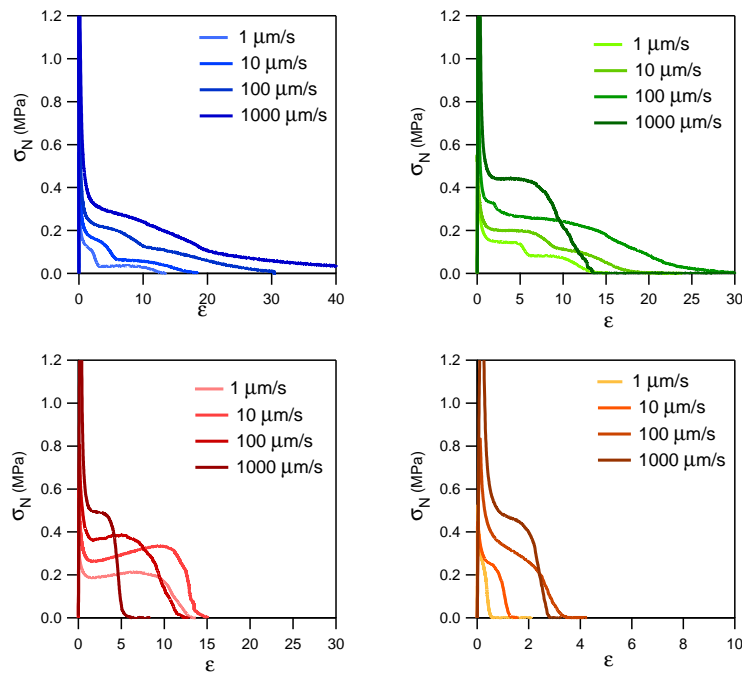


FIGURE 2.20 – Stress-Strain tack curves at four debonding velocities for A650 (top left), A1070 (top right), 1570 (bottom left) and Bg1110 (bottom right) on stainless steel probe.

The adhesion energy was measured for all the experiments on stainless steel from the integral of the stress strain curve. Results are summarized on Fig.2.21. A maximum is observed for A1570 and B1080 while for other materials, W_{adh} simply increases vs V_{deb} . A distinction between the failure modes (full circles for cohesive debonding and empty circles for adhesive failure) has been drawn on this figure. For Bg1110, where energy is mainly dissipated at the interface, the adhesion energy seems to follow a power law. This result is consistent with the theory of crack propagation in elastic materials (Shull et al., 1998). For the softest material, A650, the stress during the growth of the fibrils, σ_{fib} , strongly increases as the elastic modulus increases with frequency. As ϵ_{max} increases with v_{deb} , W_{adh} follows the trend. For other materials, the transition from cohesive to adhesive failure leads to an optimum around this transition except for A1070.

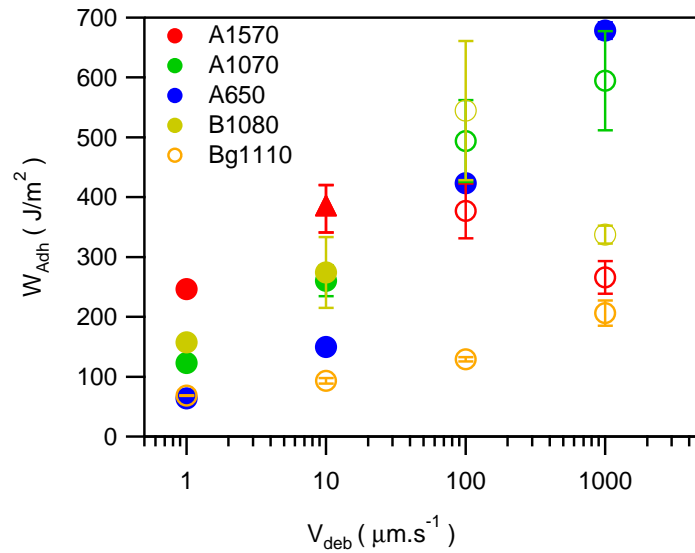


FIGURE 2.21 – Adhesion energy for the five materials vs debonding velocity on SS. Empty circles are for adhesive debonding and full circles for cohesive debonding. Triangle represents a mixed failure. Note that Bg1110 shows adhesive debonding in all cases.

In order to study the impact of the surface of the probe, we also used a probe made with Polyethylene (PE) and realized the same series of tests. Results for a pulling velocity of $100 \mu\text{m}/\text{s}$ are shown on Fig. 2.22. The results are very different from the case of stainless steel. For all materials except A650, the experiment leads to an interfacial crack propagation and to a low adhesion energy W_{adh} . A650 leads to bulk deformation and adhesive debonding, even if the shape of the curve may let one think otherwise. The difficulty to get a strong interaction between the adhesive and the PE results in an easy propagation of cracks at

the interface, limiting any deformation in the bulk. When the material is more viscous than viscoelastic (like A650), the energy of adhesion is higher, but since the material does not strain harden in extension : the failure is cohesive. The differences in results obtained between the SS probe and the PE probe show well the difficulty to simultaneously tune a PSA to adhere well on surfaces creating strong interactions (SS) and those creating weak interactions.

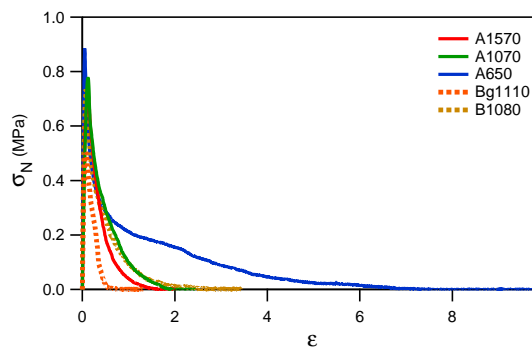


FIGURE 2.22 – Stress-Strain tack curves for the five different materials at a debonding velocity of $100\mu\text{m}/\text{s}$ on a Polyethylene probe.

By varying the pulling velocity of the experiments for our different materials, we were able to obtain a series of experimental conditions where interfacial crack propagation is observed, and others where bulk deformation is observed. All experiments but two showed an adhesive failure. We will discuss these transitions as well as that between adhesive and cohesive failure observed with the other probe in the next section.

Analysis of the transitions between mechanisms

As discussed in the first chapter (section 1.4.2, p.31), different mechanisms can occur during the debonding of a PSA. At the beginning of the debonding, the initial deformation of the adhesive can either lead to an interfacial propagation of a crack or to a bulk deformation of the material and to a fully developed fibrillar structure. This transition has been shown to depend on the ratio between the critical energy-release rate (i.e energy per unit area necessary to propagate a crack at a given velocity) G_c and the elastic modulus E for elastic materials (Crosby et al., 2000). We explained in the last chapter (see section 1.4.2 p.32) that $\frac{\tan \delta(\omega)}{G'}$ can be used as an empirical criterion to predict which one of the two mechanisms is dominant.

This parameter has been tested to separate the interfacial debonding from the bulk deformation for PDMS gels (Nase et al., 2008) and for emulsion poly-

merized acrylic PSAs (Deplace et al., 2009). G' and $\tan \delta$ for a given debonding velocity are obtained by using the Cox-Merz rule discussed before. The strain rate used in this case is the nominal one at the beginning of the debonding. As an example, a tack experiment with a debonding velocity of $10 \mu\text{m}\cdot\text{s}^{-1}$ on a film with a thickness of $100 \mu\text{m}$ ($\dot{\lambda} = 0.1\text{s}^{-1}$) is considered as equivalent to a frequency of 0.1 Hz under SAOS. We can then plot the data for the different experiments realized on PE and showing bulk deformation or interfacial crack propagation in a G' vs. $\tan \delta$ plot.

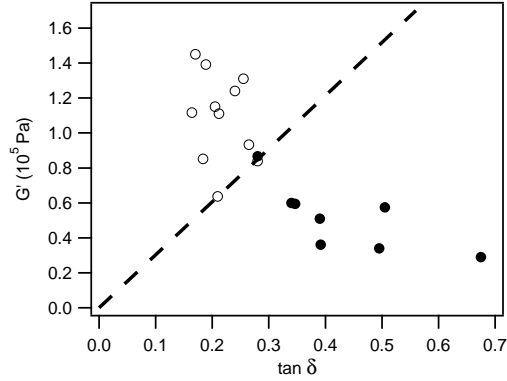


FIGURE 2.23 – G' vs $\tan \delta$ for all five materials at 0.01 , 0.1 , 1 and 10 Hz with analysis of the debonding mechanism for equivalent tack experiments at 1 , 10 , 100 and $1000 \mu\text{m}\cdot\text{s}^{-1}$ on PE. Empty circles stand for interfacial crack propagation debonding, full circles for bulk deformation (with adhesive or cohesive failure).

As shown in Fig.2.23, the two mechanisms (empty circles for interfacial crack propagation and full circles for bulk deformation) are clearly discriminated by a value of $\frac{\tan \delta(\omega)}{G'} = 0.35 \cdot 10^{-5} \text{ Pa}^{-1}$. This value is of course characteristic of PE, as all the experiments but one realized on SS showed bulk deformation. For SS, the transition value cannot be discussed as all the materials showed a bulk deformation. Nevertheless, we can conclude that this value should be inferior to $0.11 \cdot 10^{-5} \text{ Pa}^{-1}$. As a comparison, Deplace et al. (2009) obtained values of $\tan \delta(\omega)/G' = 10^{-5} \text{ Pa}^{-1}$ on PE and $0.5 \cdot 10^{-5} \text{ Pa}^{-1}$. The value for SS is in agreement for the boundary we found but the transition value is lower in our case. We can suppose that the very different structures of the polymers (nanostructured and cross-linked for Deplace *et al.*, mostly linear and uncross-linked in our case) play a role in the variation of this transition parameter. This will be confirmed by experiments on cross-linked systems in the Chapter 6 of this thesis.

If bulk deformation is the dominant deformation mechanism, the adhesive material can eventually debond by detaching from the interface (adhesive debonding) or by breaking inside the material (cohesive debonding). This result

is easily observed by the presence or not of material on the probe at the end of the test. Results of failure modes on SS are summarized in Table 2.4. Another proof that our materials are highly strain-rate dependent is that the failure modes change for all materials except Bg1110 at a given rate, different for each material. This shows well that our materials are especially well defined to study the transition between bulk and interface transition as shown in Fig. 2.23 and, in the case of bulk deformation as observed in SS in all cases, the transition between adhesive and cohesive debonding.

Despite the absence of any hardening measured in the tensile test, A1570, A1070 and A650 show an adhesive debonding for high debonding rates (experiments at $10 \mu m.s^{-1}$ show a light deposit of material on the probe, proof of an intermediate mechanism between adhesive and cohesive failure). This confirms what was observed with extensional rheology : at high extension, the material stores elastic strain energy and this strain hardening relative to the linear viscoelastic regime may be a signature of stickers bonds between chains which will not be felt under a lower strain rate. As expected, adhesive debonding is more easily obtained for materials with a higher value of $G'(\omega)$. Results of debonding from PE are not shown since all experiments led to adhesive failure excepted A650 at $1 \mu m.s^{-1}$ and $10 \mu m.s^{-1}$. This is due to the weak interactions with the polyolefin surface which lead to an easier failure at the interface.

	$1 \mu m.s^{-1}$	$10 \mu m.s^{-1}$	$100 \mu m.s^{-1}$	$1000 \mu m.s^{-1}$
A650	Cohesive	Cohesive	Cohesive	Adhesive
A1070	Cohesive	Cohesive	Adhesive	Adhesive
A1570	Cohesive	Coh/Adh	Adhesive	Adhesive
B0180	Cohesive	Adhesive	Adhesive	Adhesive
Bg1110	Adhesive	Adhesive	Adhesive	Adhesive

TABLE 2.4 – Failure modes for the five materials at four debonding rates on SS. On PE, all materials fail adhesively except A650 at $1 \mu m.s^{-1}$.

The ratio C_{soft}/C_{hard} is expected to have some predictive power for the debonding mechanisms (i.e bulk deformation leading to high adhesion energy dissipated and adhesive failure) on high adhesion energy, like SS. C_{soft} and C_{hard} were calculated for $\dot{\lambda} = 1 s^{-1}$, corresponding to a pulling velocity of $100 \mu m.s^{-1}$, see Tab. 2.3. However the ratio C_{soft}/C_{hard} could be only calculated for B1080 and Bg1110 because other tensile curves did not show any hardening part allowing us to calculate a C_{hard} . The C_{soft}/C_{hard} superior to 2 for B1080 and inferior to 2 for Bg1110 discriminates well which material showed good performances at this rate : Bg1110 is too elastic to dissipate enough energy, which is well described by a low value of C_{soft}/C_{hard} . Nevertheless, A1570 did not show any hardening in tensile test but behaved in the same way than B1080 (see Fig. 2.19). Thus, while it predicted well good performances of B1080, it was not efficient to predict the good performances of A1570, as the tool is not really

discriminating for uncross-linked materials. We will discuss in Chapter 4 of this thesis a new criterion to characterize behavior at large strain and will calculate it on a wide range of strain rates to predict debonding modes.

2.7 Conclusion

In this chapter, we characterized in detail the model acrylic polymers that have been designed to represent PSA covering a wide range of viscoelastic properties. Two series of polymers were synthesized by Dow Chemical Company for the Project MODIFY.

A range of molecular weights has been obtained with polymers that are essentially linear and uncrosslinked, with a different architecture between the two series. Only one polymer contained some gel fraction (Bg1110). A detailed mechanical characterization has been carried out on five of these materials, using small amplitude shear oscillation, tensile tests and extensional rheology. Their behavior ranges from that of a viscoelastic liquid (A650) which flows under deformation, to that of a viscoelastic solid for Bg1110. While strain hardening relative to neo-Hookean elasticity is observed only for the B series under tensile test, all materials show some hardening relative to linear viscoelasticity in extensional rheology experiments carried out at a constant strain rate. While the geometry of these tests is identical, the nominal strain rate $\dot{\epsilon}_N$ is higher at high strains for extensional rheology. This rate-dependent hardening can be explained by the presence of stickers felt only for a high enough rate. Thus, two dynamics control the mechanical response of this material: the entangled polymer network dynamics and the sticker dynamics. The two uniaxial tests used are interesting in their own ways: tensile test is representative of what happens in tack tests while extensional rheology, at constant $\dot{\epsilon}_H$ is easier to model. The dynamics of our polymers, the differences between uniaxial tests and their use to predict a transition between adhesive and cohesive debonding will be further discussed in Chapter 4.

Adhesive properties of the materials were studied with a probe-tack test over a range of debonding rates and with two probes showing different surface interactions. This led us to observe the three characteristic debonding mechanisms of PSAs. Using the experiments on PE, we were able to characterize the transition between interfacial crack propagation and bulk behavior, determined by a value of $\tan \delta(w)/G'(\omega) = 0.35 \cdot 10^{-5} Pa^{-1}$. Transition from cohesive failure to adhesive failure on stainless steel was observed at a high enough strain rate for all materials except Bg1110. While the ratio C_{soft}/C_{hard} discriminates well materials of the B series, it is not adapted to uncrosslinked materials of the A series. We will see in Chapter 4 an introduction of a new parameter for uncrosslinked materials.

While this complete characterization allows us to better understand the materials available, their range in mechanical and adhesive properties and the relations between both, we can go a step further by systematically analyzing the images obtained during the probe-tack experiments. This should allow us to determine relations between the growth and the shape of the cavities created during the debonding and the adhesive properties, and to better compare tensile

experiments with probe-tack tests. These analysis and discussions will be done in the next chapter.

Bibliographie

- Agirre, A., Nase, J., Degrandi, E., Creton, C., and Asua, J. M. (2010). Improving adhesion of acrylic waterborne PSAs to low surface energy materials : Introduction of stearyl acrylate. *Journal of Polymer Science Part A : Polymer Chemistry*, 48(22) :5030–5039.
- Aubrey, D. W. and Ginosatis, S. (1981). Peel adhesion behaviour of carboxylic elastomers. *The Journal of Adhesion*, 12(3) :189–198.
- Bellamine, A., Degrandi, E., Gerst, M., Stark, R., Beyers, C., and Creton, C. (2011). Design of nanostructured waterborne adhesives with improved shear resistance. *Macromolecular Materials and Engineering*, 296(1) :31–41.
- Cox, W. P. and Merz, E. H. (1958). Correlation of dynamic and steady flow viscosities. *Journal of Polymer Science*, 28(118) :619–622.
- Crosby, A. J., Shull, K. R., Lakrout, H., and Creton, C. (2000). Deformation and failure modes of adhesively bonded elastic layers. *Journal of Applied Physics*, 88(5) :2956–2966.
- Degrandi, E. (2009). *Latex Hybrides Urethane/Acrylique Pour Applications Adhésives*. PhD thesis, Université Pierre et Marie Curie.
- Deplace, F. (2008). *Waterborne nanostructured Adhesives*. PhD thesis, Université Pierre et Marie Curie.
- Deplace, F., Carelli, C., Mariot, S., Retsos, H., Chateauminois, A., Ouzineb, K., and Creton, C. (2009). Fine tuning the adhesive properties of a soft nanostructured adhesive with rheological measurements. *The Journal of Adhesion*, 85(1) :18–54.
- Lakrout, H., Sergot, P., and Creton, C. (1999). Direct observation of cavitation and fibrillation in a probe tack experiment on model acrylic pressure-sensitive adhesives. *The Journal of Adhesion*, 69(3) :307.
- Lindner, A., Lestriez, B., Mariot, S., Creton, C., Maewis, T., Lühmann, B., and Brummer, R. (2006). Adhesive and rheological properties of lightly crosslinked model acrylic networks. *The Journal of Adhesion*, 82(3) :267–310.
- Munstedt, H. (1980). Dependence of the elongational behavior of polystyrene melts on molecular weight and molecular weight distribution. *Journal of Rheology (1978-present)*, 24(6) :847–867.
- Munstedt, H. and Laun, H. (1979). Elongational behaviour of a low density polyethylene melt. *Rheologica Acta*, 18(4) :492–504.
- Nase, J., Lindner, A., and Creton, C. (2008). Pattern Formation during Deformation of a Confined Viscoelastic Layer : From a Viscous Liquid to a Soft Elastic Solid. *Phys. Rev. Lett.*, 101 :074503.

- Plessis, C., Arzamendi, G., Alberdi, J. M., van Herk, A. M., Leiza, J. R., and Asua, J. M. (2003). Evidence of branching in poly(butyl acrylate) produced in pulsed-laser polymerization experiments. *Macromolecular Rapid Communications*, 24(2) :173–177.
- Poivet, S., Nallet, F., Gay, C., Teisseire, J., and Fabre, P. (2004). Force response of a viscous liquid in a probe-tack geometry : Fingering versus cavitation. *The European Physical Journal E*, 15(2) :97–116.
- Roos, A. and Creton, C. (2005). Effect of the presence of diblock copolymer on the nonlinear elastic and viscoelastic properties of elastomeric triblock copolymers. *Macromolecules*, 38(18) :7807–7818.
- Shull, K. R., Ahn, D., Chen, W.-L., Flanigan, C. M., and Crosby, A. J. (1998). Axisymmetric adhesion tests of soft materials. *Macromolecular Chemistry and Physics*, 199(4) :489–511.
- Tobing, S. D. and Klein, A. (2001). Molecular parameters and their relation to the adhesive performance of acrylic pressure-sensitive adhesives. *Journal of Applied Polymer Science*, 79(7) :2230–2244.
- Zosel, A. (1985). Adhesion and tack of polymers : Influence of mechanical properties and surface tensions. *Colloid Polym. Sci.*, 263 :541–553.

Chapitre 3

Analysis of the growth of cavities at the interface

The results of this chapter have been published in the peer-reviewed journal European Physics Journal-E under the title "Quantitative analysis of the debonding structure of soft adhesives", January 2014, 37 :3.

Contents

2.1	Introduction	57
2.2	Specifications of the model materials	57
2.3	Characterization of the polymers synthesized	59
2.3.1	Molecular weight and gel content	59
2.3.2	Architecture characterization	61
2.4	Mechanical characterization	62
2.4.1	Sample preparation	62
2.4.2	Linear viscoelastic characterization	62
2.4.3	Characterization of the non-linear properties	63
2.5	Adhesive Characterization	65
2.5.1	Sample preparation	65
2.5.2	Probe-tack test	66
2.6	Results and Discussions	69
2.6.1	Mechanical characterization	69
2.6.2	Adhesion characterization and debonding mechanisms	74
2.7	Conclusion	81

3.1 Introduction

When soft adhesives are detached from rigid surfaces, the incompressibility of the material combined to its extreme deformability leads to complex deformation patterns involving the formation of air fingers and cavities (Nase et al., 2010; Urahama, 1989; Lakrouf et al., 1999; Yamaguchi et al., 2007; Zosel, 1998). The details of these patterns depend markedly on the material properties and often evolve towards a fibrillar structure of highly stretched polymers which eventually fail by fracture or detach from the surface (Deplace et al., 2009b). The criteria for the onset of the initial elastic or viscous instabilities have been known for some time (Crosby et al., 2000; Nase et al., 2008) and several experimental studies have focused on fingering instabilities (Nase et al., 2008; Shull et al., 2000; Nase et al., 2011), on the cavitation criteria (Chiche et al., 2005; Chikina and Gay, 2000; Poivet et al., 2003, 2004; Tirumkudulu et al., 2003), cavity nucleation rate (Peykova et al., 2010, 2012) or growth rate (Brown et al., 2002). However the transition from growth of individual cavities to the collective growth of a population of cavities under the applied stress, leading to elongated walls between cavities, also called "fibrils" and to eventual detachment, has received much less attention experimentally (Peykova et al., 2010, 2012). Some theoretical papers have been published on collective growth (Yamaguchi et al., 2006a,b).

Up to date, it remains difficult to relate the observed patterns to the rheological properties of the soft adhesives, mainly due to the lack of precise experimental characterization of the 3D structures and of the material deformation during the debonding process. Because the processes are dynamic, powerful 3D scanning techniques, such as confocal microscopy, are too slow and one has to rely on classical 2D imaging limited by its depth of field. Proper identification of the cavity borders in an automatic and reliable way is not a trivial task and requires good quality well contrasted images and adapted imaging software tools. Yet, this information, albeit statistical in nature, is essential if one wishes to gain more insights on the debonding process and to be able to compare experiments with results from numerical simulations. It is also a necessary ingredient to understand which rheological properties of the material determine the debonding patterns and, eventually, the adhesion performance, the important parameter for practical applications.

In this chapter, we perform careful experiments yielding high contrast images of the cavities nucleated in the early stages of debonding during a probe tack test. We develop precise image analysis tools to characterize quantitatively and in a statistically significant way the size, shape and overall projected surface of the cavities. Using selected model materials studied in the previous chapter, we present detailed measurements of the growth dynamics of cavities, including the total projected area, the average cavity shape and their growth rate. These measurements give access to a corrected true or effective stress and strain which can then be quantitatively compared with material properties in shear and uniaxial extension.

3.2 High resolution observation and numerical analysis

3.2.1 Probe-Tack tests coupled with microscope

A home built "probe tack" set up (Josse et al., 2004), similar to the one presented in section 2.5.2 (p.65), coupled this time with a microscope, was employed to observe the deformation structure of the soft adhesives and to measure force and displacement during debonding.

After a contact time of 10 s, the probe was pulled away at a constant rate V of 1 or 10 $\mu\text{m s}^{-1}$. In order to ensure a total and reproducible contact area, the thickness of the sample h_0 was increased 140 μm (100 μm in chapter 2). the nominal strain rate approximated by V/h_0 was 0.007 and 0.07 Hz, respectively. The force F and displacement d were measured during the whole experiment. In this chapter, we used only a SS probe with a diameter of 6 mm, prepared the same way as the probe used in the Chapter 2.

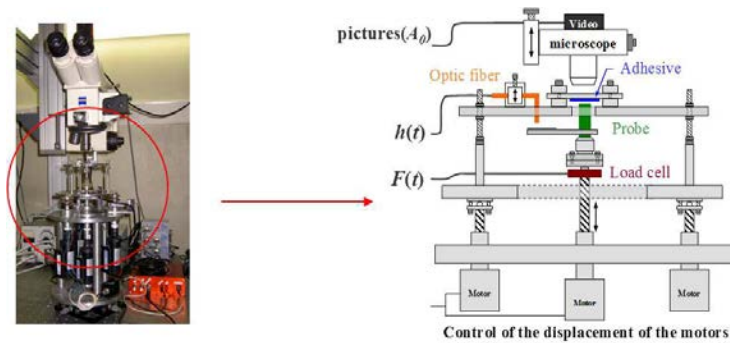


FIGURE 3.1 – Picture and scheme of the probe-tack coupled with a microscope. During the debonding, the lateral motors move, allowing the interface to be static and thus a better quality of the images.

A microscope was coupled to this experiment in order to observe the debonding structure from the top, see Figure 3.1 for the complete set-up. A camera (resolution of 1292×964 pixels) numerical recorded the digitalized images. Two Zeiss lenses (1.25x and 5x) were used in order to get low or high magnification images, with a field of view of 7.34×5.48 mm and 1.92×1.44 mm, respectively. Images and force-displacement data were synchronized with a trigger to start simultaneously the probe-tack experiment and the image acquisition process. This trigger also controlled the frequency of the acquisition of the images, setting a frame rate of 10 and 20 fps for a velocity of 1 and 10 $\mu\text{m s}^{-1}$, respectively.

3.2.2 Image Analysis

Quantitative information about the nucleation and the growth of cavities can be obtained by processing the digitalized top-view images acquired in probe-tack experiments. We developed a simple method to analyze these images by only resorting to standard routines already available in many packages for image processing, such as the Image Processing ToolboxTM for Matlab[®]. An example of the result of this procedure is shown in Figure 3.2.

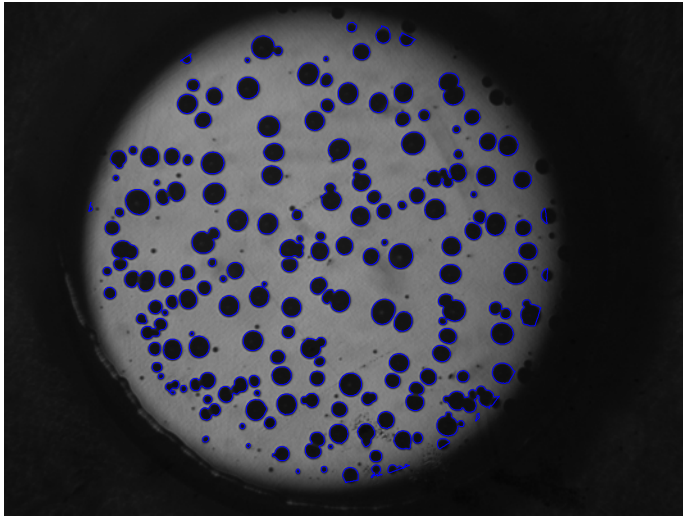


FIGURE 3.2 – Processed top-view frame of the cavitation process. Blue contours represent the borders of the cavities our algorithm is able to detect. Only a few small cavities are missed because they are below the noise level. They will be tracked in the next frames when their area exceeds ϵ_A (see the main text).

The algorithm detects all cavities with a surface larger than a threshold $\epsilon_A = 50$ pixels. Several geometrical quantities, such as the center of mass, the area, the equivalent diameter and the eccentricity are measured for each cavity. The program also assigns an index to each cavity and by comparing the center of mass of cavities between two subsequent frames, nucleation and coalescence events can be tracked.

Image Analysis algorithm

The algorithm starts with a calibration routine before the nucleation of cavities. In this first step, through a trial and error procedure, we estimate the critical level τ_0 (with $0 < \tau_0 < 1$) for the conversion from grayscale to binary image. Besides, we determine the region of the image within which we run our detection routine for the cavities. This region is established at the beginning of

the image recognition procedure and does not evolve with time. The algorithm assigns to each cavity an index and manages dynamically the events of nucleation and coalescence [for details see point 4.]. Obviously, an empty list is created at the start of the procedure. Then, the algorithm repeats the following steps for each frame :

1. The image is filtered with a low pass filter in order to reduce its noise content, we typically use a simple averaging over windows of size 3×3 pixels.
2. The format of the image is converted from greyscale to binary according to τ_0 , that is, all the pixels with luminance smaller than τ_0 are mapped to 1 (white) while the others to 0 (black).
3. All the connected regions with area smaller than a threshold ϵ_A are removed. This step is easily implemented by morphologically opening the binary image.
4. The boundaries between black and white regions are traced and labeled with an index. The children of each parent object are discarded in order to avoid the wrong detection of small cavities inside a large encompassing cavity. These white spots are created by the unscattered light that passes through the cavity and is reflected back from the steel substrate. Although their position and their extension is related to the contact region of the cavity with the steel substrate, these quantities are very sensitive to many irreproducible factors, such as the intensity of the light, the magnification factor and the sample alignment. For this reason these white spots are not taken into account in the analysis of the images from whole probe experiments.
5. For each cavity several geometrical quantities are measured, e.g. its center of mass, area, equivalent diameter, and eccentricity.
6. By comparing the center of mass of cavities in the current and the previous frame, the index of each cavity is changed according to the list of indexes of the previous frame. In this step the processes of nucleation and coalescence of cavities are handled. For each new nucleated cavity a new entry in the list is created with a new index $n_T + 1$, where n_T is the largest index of the list. However, when the coalescence of two or more cavities occurs, the new data of the coalesced cavity are assigned to the lowest index in the list while the entries of the other cavities are deleted. In this manner we are able to track the evolution of each cavity and record all the coalescence events.

Thick film samples ($\sim 600 \mu\text{m}$) for rheology and tensile tests and thin films ($\sim 140 \mu\text{m}$) coated on glass slides were prepared the same way as in Chapter 2 (see respectively section 2.4.1 (p.61) and section 2.5.1 (p.64)). In both cases transparent cohesive films were obtained showing a good coalescence of the particles of the latex.

3.3 Material Properties

Three representative materials from the materials discussed in the last chapter were chosen to study their debonding structures : A650, A1570 and Bg1110. Their main chemical parameters are reminded in Table 3.1.

Polymer	CTA (%)	Mw (kg/mol)	PDI (-)	d_0 (nm)	Gel content (%)
Bg1110	-	1115	3.39	368	30
A1570	-	1572	2.57	400	-
A650	0.1	651	2.18	400	-

TABLE 3.1 – Properties of the model acrylic polymers. The parameter d_0 is the diameter of the particles, see Chapter 2 for more details.

As the thickness of the layer for probe-tack tests is higher than in Chapter 2 and the tensile test strain rate is adjusted to correspond to the equivalent rate of probe-tack experiments, we will discuss here again the mechanical and adhesive properties of these materials.

3.3.1 Mechanical properties

The three different materials studied differ only in architecture and molecular weight and the molecular interactions with a substrate should thus be the same for all three materials. Figure 3.3 shows master curves at 20°C of G' and G'' as a function of angular frequency ω already discussed in chapter 2 and in an article from (Mohite et al., 2013). The curves were obtained by applying time-temperature superposition and it can be seen that the viscoelastic properties of the three materials are identical at frequencies f larger than 10 Hz. However, at low frequencies the rheology of A650 differs from the behavior found for A1570 and Bg1110. The elastic modulus of A650 decreases strongly at low frequency, leading to a material with a pronounced viscoelastic character. A1570 and Bg1110 on the other hand can be described as soft viscoelastic solids over the whole range of frequencies.

While linear viscoelastic properties characterize time-dependent relaxation processes, strain-dependent behavior is characterized using large strain properties measured at a given strain rate. Tensile tests were performed to obtain the mechanical properties of the sample in uniaxial deformation in the same conditions as in section 2.4.3 (p.62). We imposed two different cross-head velocities v , 1.05 and 0.105 mm s⁻¹, for samples with an initial length l_0 of 15 mm (initial cross section $S_0 = 2.5$ mm²), resulting in a nominal initial strain rate v/l_0 of 0.07 and 0.007 Hz, respectively, equivalent to the one obtained in probe-tack tests discussed in this chapter. In uniaxial extension, the materials show pronounced differences, as shown in Figure 3.4 by the experimental curves of nominal stress $\sigma_N = F/S_0$ versus the deformation of the sample $\lambda = l(t)/l_0$. Macroscopic flow

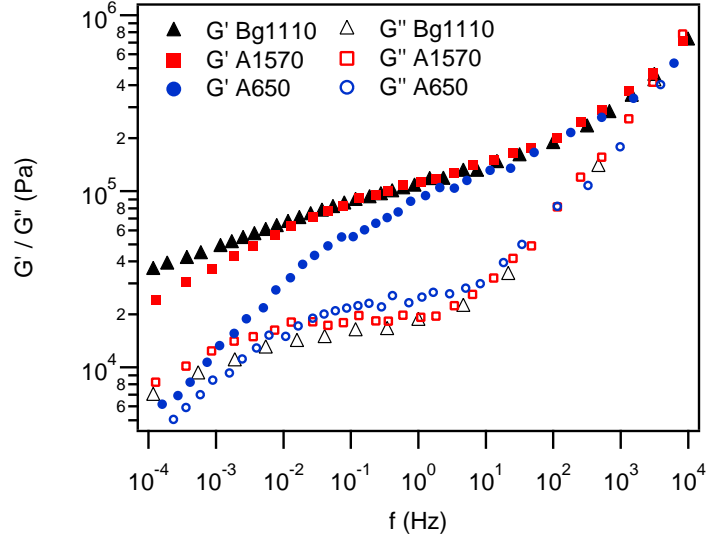


FIGURE 3.3 – Storage (G') and shear (G'') modulus as function of angular frequency (ω) for the three different materials (Mohite et al., 2013).

is observed for the most viscoelastic material, i.e. the A650 series, while a slight strain hardening behavior characterizes the Bg1110 adhesive. Although A1570 and Bg1110 have identical linear viscoelastic properties at frequencies above 0.01 Hz, the presence of a gel fraction in the Bg1110 series results in a different large-strain behavior and we observe a markedly higher stress at large strain.

3.3.2 Adhesion properties

Probe tack tests were carried out at two probe velocities (1 or 10 $\mu\text{m s}^{-1}$) for the three materials. For all experiments, the adhesive films have an initial thickness h_0 and are pulled by a cylindrical probe of area A_T . Experiments were repeated several times and the force F_T and the displacement $d = h(t) - h_0$ as a function of time were measured. The nominal stress is given by

$$\sigma_N = \frac{F_T}{A_T}, \quad (3.1)$$

while the nominal deformation reads

$$\lambda = \frac{h}{h_0}, \quad (3.2)$$

and represents the nominal deformation of the whole sample in the vertical direction.

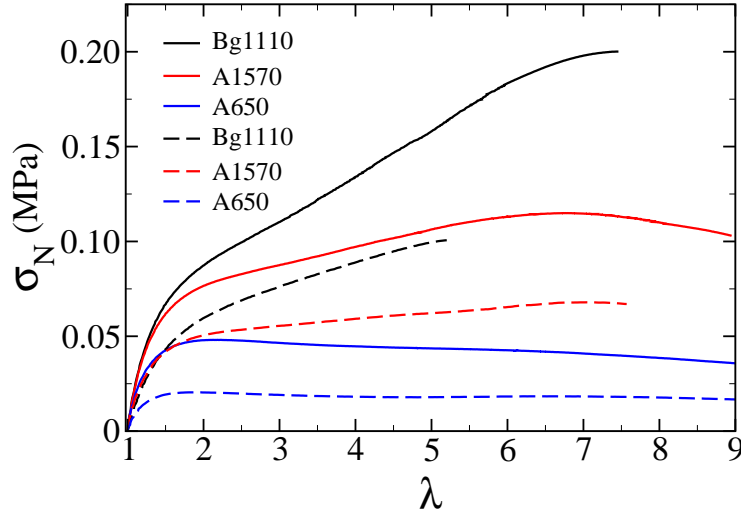


FIGURE 3.4 – Nominal stress versus deformation in tensile test for a deformation rate $\dot{\lambda}_z = 0.07$ (solid lines) and $\dot{\lambda}_z = 0.007$ (dashed lines).

The experiments are filmed at low and high magnification to capture the dynamics of cavity nucleation and growth. During the displacement of the probe the volume between the probe and the glass slide expands. As the adhesive is incompressible and does not slip at the interface, this increase in volume leads to a large increase in tensile stress inside the layer and to the nucleation of cavities at the interface between the probe and the adhesive (Creton and Lakrout, 2000) and to their subsequent growth. Note that as the volume of the cavities expands the pressure inside the cavities tends towards zero.

The nominal stress-strain curves $\sigma_N = f(\lambda)$ are shown on Figure 3.5 and are discussed together with the different dynamics of cavity growth. At a debonding rate of $10 \mu\text{m s}^{-1}$ (Figure 3.5a), three different shapes of stress-strain curves are observed for the three materials used. Bg1110, the most elastic material, shows a sharp stress peak, followed by a fast decrease of σ_N . This shape is explained by the nucleation of cavities during the increase in σ_N . These cavities first expand in the bulk of the layer but eventually coalesce at the interface with the substrate. This rapid coalescence leads to the fast decrease in nominal stress observed and results in interfacial debonding. For A1570, cavities also mainly nucleate during the initial increase of the nominal stress. At higher deformation the nominal stress is found to stabilize at a nearly constant value, characteristic of the growth of cavities in the bulk and the subsequent formation of elongated walls or fibrils. At the end, the fibrils detach from the surface, leading to an adhesive debonding. The experiment with A650 shows a double plateau, characteristic of liquid-like materials. In this case the walls formed between growing cavities are too liquid-like to sustain the pressure difference between the low pressure cavities and the

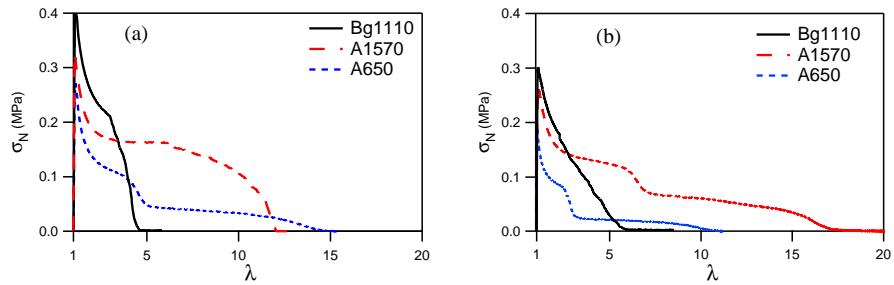


FIGURE 3.5 – Nominal stress σ_N for the three materials as a function of the deformation λ at a pulling velocity of $10 \mu\text{m s}^{-1}$ (a) and $1 \mu\text{m s}^{-1}$ (b).

atmospheric pressure and pressure equilibration takes place before final fibril detachment (Poivet et al., 2004). In this case cohesive failure, i.e. residues on the probe, are observed.

At $1 \mu\text{m s}^{-1}$ (Figure 3.5b), the shape of the stress-strain curve of the Bg1110 and A650 are qualitatively identical except for a decrease of the overall stress during debonding. For A1570, a transition is observed towards a liquid-like behavior with two plateaus.

3.4 Analysis of the debonding structure

3.4.1 Evolution of the load-bearing area

Due to the presence of cavities, the force applied on the disk-shape sample is effectively only applied on a load-bearing cross section that becomes increasingly smaller as λ increases. By analyzing the projected area covered by the cavities

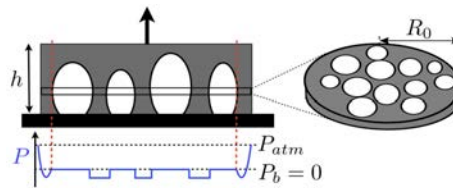


FIGURE 3.6 – Left : representation of the sample under deformation. The load bearing area determined by the top-view analysis is represented by the slice shown on the right. The effective normal stress (sec. 3.4.4) and the effective elongation (sec. 3.4.5) are calculated for this slice and correspond to averages over the area of the slice. Bottom : Sketch of a typical pressure distribution in the stretched adhesive layer containing cavities.

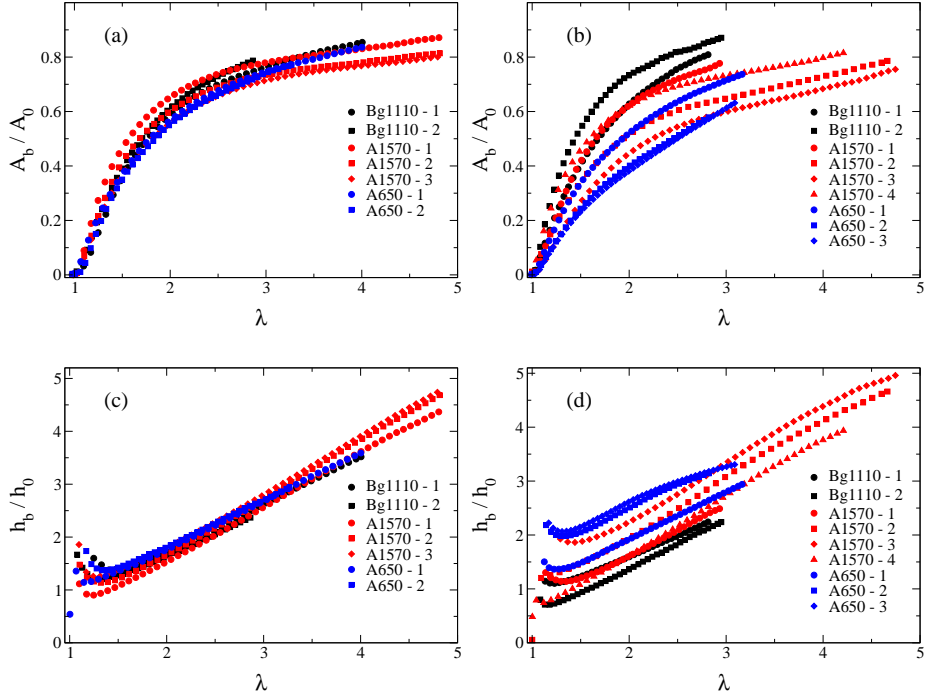


FIGURE 3.7 – Evolution of the normalized projected area covered by the cavities A_b/A_0 (a and b) and the normalized average cavity height h_b/h_0 (c and d) as function of the nominal elongation λ . These experiments were performed at a constant pulling velocity of $10 \mu\text{m s}^{-1}$ and $1 \mu\text{m s}^{-1}$.

and subtracting it from the total contact area, this load bearing area can be obtained. This will allow us to calculate (in the following section) the average true or effective stress applied, instead of the nominal stress studied in previous investigations (Lakrout et al., 1999; Chiche et al., 2005; Peykova et al., 2010; Zosel, 1985).

By means of the image analysis method described in the previous section we can measure for each frame the total area covered by the cavities A_b and then subtract it from the area of the probe A_0 , corresponding to the total contact area. Note that for our experiments no debonding takes place from the edges of the probe and the total contact area A_0 does thus not evolve during the experiment. In this way we deduce the load-bearing cross section of our disk as a function of time, $A_e(t) = A_0 - A_b(t)$. This latter quantity is simply the effective area of the walls between cavities. As the observation direction is normal to the disk, the maximal diameter of each cavity is observed in the projected image, see the sketch in Figure 3.6, and we thus obtain the minimal projected area of the walls between the cavities. Note that the illuminated area on which the image analysis is performed is typically slightly smaller than the area of the probe A_0 .

For simplicity reasons we do however not distinguish these areas explicitly, but whenever necessary we corrected for the small difference.

The precise measurement of the growth dynamics of the cavities can unfortunately not be undertaken for the complete force–displacement curve. Due to loss of contrast and resolution we can only precisely track cavities until $\lambda = 3 - 5$, i.e. the first part the curves shown on Figure 3.5 and all the following results will be restricted to this elongation range.

The study of the evolution of the projected areas taken by the cavities A_b as a function of time and nominal elongation λ gives interesting insights on the growth dynamics of the cavities and can be linked to the rheological properties of the material and to the adhesion at the interface with the probe.

Cavity nucleation is, for the used materials, mainly determined by the presence of small defects at the interface between the sample and the probe. The spatial and time distribution of cavity nucleation are thus given by the spatial and size distribution of these defects and are thus not reproducible between experiments (Chiche et al., 2005). The picture shown on Figure 3.2 thus has to be taken as an example of a typical distribution of cavity locations and sizes and it is not necessarily representative of all experiments. Interestingly, however, when the probe is pulled at $10 \mu\text{m s}^{-1}$ the function A_b/A_0 (shown on Figure 3.7a) is very reproducible for different experiments with the same material and is found to be similar for the three materials.

Contrary to the tests at $10 \mu\text{m s}^{-1}$, when the probe is pulled more slowly (at $1 \mu\text{m s}^{-1}$), see Figure 3.7b, some scatter is observed for A_b/A_0 for each material and A_b/A_0 now seems to depend on the material. Bg1110 shows a faster increase in the projected cavity area, then A1570 and A650. This indicates that at slow pulling rate a more interfacial growth is observed for the more elastic material, whereas the more viscous materials show a stronger growth in the bulk. This result is consistent with what was found by Yamaguchi *et al.* (Yamaguchi et al., 2007) for adhesives with different crosslink densities. The data can also be represented as the average cavity height $h_b/h_0 = A_0/A_b(\lambda - 1)$ shown on Figure 3.7c and 3.7d showing more clearly the difference observed for the different materials at slow pulling speed. Note that the data for λ close to 1 have not been represented as cavities are only detected when their size is larger than a given threshold. In particular in the beginning of the experiment the total surface covered by cavities A_b is thus underestimated leading to an overestimation of h_b/h_0 . Further more in the beginning of the experiment some additional material from the adhesive film might be pulled under the probe leading to a small increase in total volume. Also this effect leads to an overestimation of h_b/h_0 and to the small decrease of the average cavity height with increasing λ observed on figure 3.7.

The differences in the measurements between the two probe velocities are interesting. In fact, they show that at $10 \mu\text{m s}^{-1}$ the shape of the cavity is fully determined by the high frequency behavior of the materials, which does not vary much between the different materials. On the other hand, at $1 \mu\text{m s}^{-1}$, differences in rheological properties do lead to significantly different kinematics which will eventually lead to very different levels of dissipated energy.

3.4.2 Projected shape of cavities

During the early stages of the debonding process described in the previous paragraph, the shape of the projected area of individual cavities undergoes a transition from a circular to a more irregular form. Initially cavities grow in a circular manner. As the cavities start to occupy more volume they begin to feel each other through elastic interactions and viscoelastic flow. These interactions lead to a deviation from their initial circular shape and, eventually, to the coalescence of cavities, further modifying the overall shape. A simple way to quantify this geometrical transition is to compute the size of the difference between the shape of the cavity and the circle with the same projected area placed at the center of mass of the cavity, see Figure 3.8. This absolute difference between areas, A_d , provides a measure of the average change in shape of the cavities, thus quantifying in this way how the material responds to an external deformation. The elasticity of the material acts here like a surface tension and restricts sharp changes in shape (Dollhofer et al., 2004).

The data is best shown as a function of the relative area occupied by cavities (A_b/A_0) as we expect their shape to evolve as a function of their interaction with each other. Note that similar trends are observed when plotting the results as a function of λ but, in particular at $1 \mu\text{m s}^{-1}$, the value of λ where $(A_b/A_0) = 0.5$ varies significantly for different materials (see Figure 3.7) making the comparison difficult.

For all materials and strain rates, the projected area of the cavities becomes markedly non-spherical as cavities interact or merge with each other. The evolution of the normalized A_d/A_0 for the two velocities is shown in Figure 3.9. At both velocities the more elastic material Bg1110 maintains more circular cavities consistent with its more elastic character. This strongly suggests that the level of elastic energy stored in the material during deformation has an effect on the curvature of the cavities.

3.4.3 Growth rate of individual cavities

We estimate the growth rate of individual cavities from the evolution of the projected area of each cavity as a function of time shortly after their nucleation.

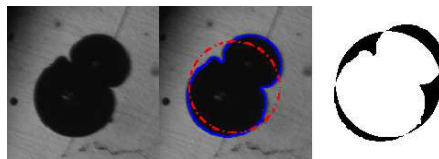


FIGURE 3.8 – Procedure to measure A_d . From left to right : i) Image of the cavity, ii) Detected perimeter (blue solid line) and equivalent circle (red dashed line) placed on the center of mass of the cavity, iii) Absolute difference between the two areas (black region).

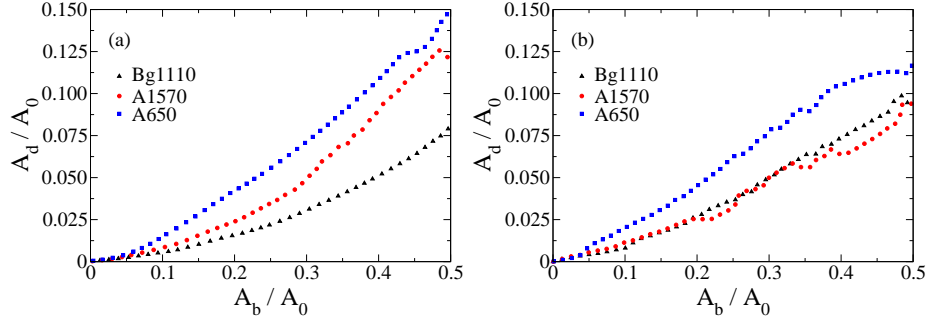


FIGURE 3.9 – Evolution of the equivalent cavity ellipticity A_d/A_0 as function of the load bearing area A_b/A_0 at the pulling velocity of $10 \mu\text{m s}^{-1}$ (a) and $1 \mu\text{m s}^{-1}$ (b).

Images of the whole probe have not enough resolution to provide this information and we thus use high magnification images (5x) of the central part of the sample.

The increase in area of a single cavity normalized by the area of the probe is shown as a function of time on Figure 3.10. From this figure it is clear that the growth of cavities does not follow a simple functional form, in agreement with previous observations (Chiche et al., 2005; Peykova et al., 2010; Brown et al., 2002). Right after nucleation, exponential cavity growth is observed (Brown et al., 2002), but quickly after this initial stage they start to interact with the surrounding cavities and their growth slows down and deviates from the exponential behavior. This is easily explained by the fact that cavities relax

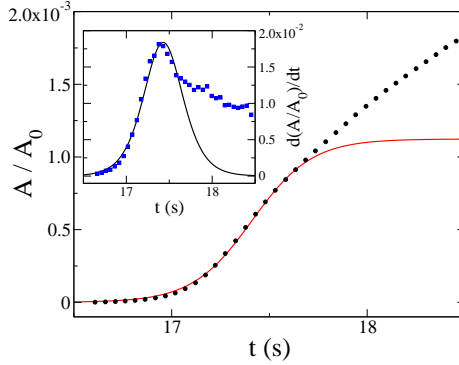


FIGURE 3.10 – Example of the evolution of the area of a growing cavity and its time derivative (inset) as a function of time and example of the fit procedure used to estimate α . Points are experimental data from digitalized images whereas solid lines correspond to fits of Eq. (3.3) and (3.4) (inset), respectively.

the accumulated stress in the adhesive layer very quickly after their nucleation, leading to a slow down of the growth.

We aim at capturing the first stages of cavity growth, as differences between different materials are expected to be important mainly when cavities grow independently. Even if cavities grow exponentially right after nucleation, the later stages of the growth rate can be approximated by a square root function and a simple exponential fit does not permit a clean estimation of the growth rate α . In fact, the time variation of the area $A(t)$ of each cavity reaches a maximum in a very short time and, subsequently, it decreases. From a practical point of view, it is easier to catch this change of behavior looking at the maximum of the growth velocity. In this way, all the data before and some data after this peak can be used for the estimation of the growth rate. This simple practical consideration allows one to increasing the number of points used for the nonlinear fit (and hence its accuracy) compared to the estimation of the growth rate with a standard exponential function.

A sigmoid function S captures the initial exponential growth of $A(t)$ and its successive relaxation in a very compact functional form

$$S = a \left[1 + e^{-\alpha(t-t_0)} \right]^{-1}, \quad (3.3)$$

where a is the amplitude of S (for $a = 1$, $S \rightarrow 1$ when $t \rightarrow \infty$), α is the growth rate, and t_0 is the moment of maximum growth. These three parameters are estimated from a nonlinear least squares fit of the time derivative of A by using the function

$$\frac{dS}{dt} = \frac{a\alpha e^{-\alpha(t-t_0)}}{\left[1 + e^{-\alpha(t-t_0)} \right]^2}. \quad (3.4)$$

A typical result of this fitting procedure is reported in Figure 3.10.

A box plot of the growth rate α for the three materials is shown in Figure 3.11. We have divided the cavities in two groups, those that have nucleated before the force peak during the probe-tack test (left column) and those nucleated after it (right column).

First of all, one can note that for the more elastic materials, Bg1110 and A1570, most of the cavities nucleate before the maximum of the stress peak is reached (Peykova et al., 2012). For the more liquid-like material however significant nucleation is observed even after the stress peak has been reached. This phenomenon can be explained by the fact that for the low modulus of the A650 material the compliance of the adhesive layer quickly drops below the compliance of the apparatus leading to a sudden transfer of energy from the apparatus to the adhesive layer initiating nucleation of further cavities. This observation is known to be apparatus dependent (Poivet et al., 2003; Tirumkudulu et al., 2003; Francis and Horn, 2001). The most interesting observation is the difference in growth rate between the different adhesives. The most elastic material, Bg1110, and the most liquid-like material, A650, both show larger growth rates with a large scatter, whereas the growth rate of the A1570 material is found to be smaller and more reproducible. For the Bg1110 the large growth

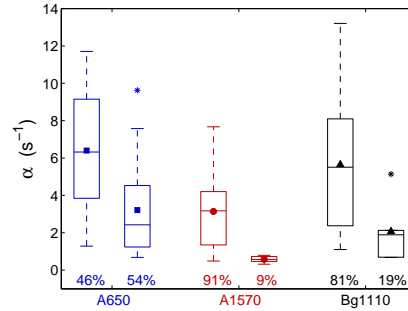


FIGURE 3.11 – Box plot of the growth rate α for the three different materials at the pulling velocity of $10 \mu\text{m s}^{-1}$. Cavities have been divided into two groups according to their nucleation time, before (left boxes) and after (right boxes) the force peak. Percentages show the proportion of cavities for each group. The total number of cavities were 39 for the A650, 53 for the A1570, and 32 for the Bg1110. The box plot is characterized by five-numbers summaries, i.e. the smallest observation (the lower horizontal line), the lower quartile (lower boundary of the box), the median (the line inside the box), the upper quartile (upper boundary of the box), and the largest observation (the upper horizontal line). We have also added the mean of each data set (the symbol inside the box) and outliers are represented by stars.

rate of the projected area can be explained by the large amount of elastic energy stored in the elastic layer, leading to strong cavity growth along the interface (a crack propagation mechanism). For A650 the resistance of the material is too small to prevent bulk expansion of cavities, also leading to rapid growth of the projected area. The A1570 material seems to have the optimal material properties and leads to a moderate growth rate. The large scatter in the growth rate of cavities nucleated before the peak, observed for A650 and Bg1110, is most likely due to differential nucleation at different stress levels leading to different growth rates (Chiche et al., 2005; Peykova et al., 2010). For A1570 the growth rate is dominated by the viscoelasticity of the material leading to smaller differences in the observed growth rates.

A detailed discussion of the criteria leading to different cavity shapes for different experimental conditions has also been carried out for simple silicone viscoelastic fluids by Teisseire *et al.* (Teisseire et al., 2007).

3.4.4 Effective Normal Stress

One of the most interesting results that comes from the detailed analysis of the kinematics of the debonding structure is the analysis of the applied force. The stress field in the material when many cavities are growing simultaneously

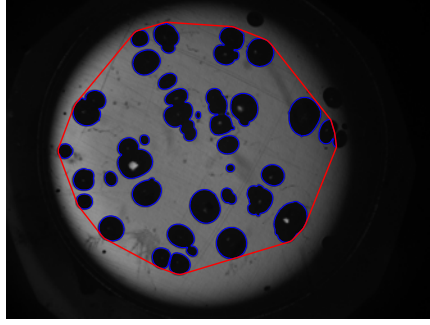


FIGURE 3.12 – Convex envelope of the region occupied by cavities (red solid line) with area A_c . Cavities with area smaller than the threshold $\epsilon_A = 50$ pixels are not taken into account. Also cavities nucleated at the border of the illuminated region are discarded because they lie outside the area our algorithm set as safe region for detection.

is complex and cannot be measured directly as a function of position. However it is possible to use average quantities such as force and total projected area of the cavities A_b to infer average information.

The measured normal force F_T results from two contributions. The first one, F_m , arises from the elongation of the viscoelastic material, whereas the other contribution, F_P , is due to the work done against the atmospheric pressure to increase the volume of the low-pressure cavities (a suction cup effect) (Poivet et al., 2003, 2004). As our interest lies in the estimation of the viscous tensile stress inside the cavity walls, we first separate these two contributions. Then we use F_m to estimate the effective viscous stress applied to the load bearing area, corresponding to the slice with the smallest cross-section.

In detail, the fraction of the measured force due to the work against the atmospheric pressure depends on the spatial distribution of the cavities on the sample. Yamaguchi *et al.* used a simple model to study the dynamics of debonding of an axisymmetric PSA simplified to a one-dimensional problem (Yamaguchi et al., 2006a,b). Their numerical investigations showed that, after nucleation of cavities, the pressure field rapidly drops to a value close to zero at the position of the two outermost cavities, leading to a screening effect on other cavities inside the PSA, in agreement with the findings of other authors (Poivet et al., 2003; Tirumkudulu et al., 2003). This result can be easily extended to our two-dimensional arrangement of cavities by considering the convex envelope of the perimeters of the cavities. A sketch of a typical pressure distribution can be seen on Figure 3.6. The dotted lines represent the position of the envelop of the cavities. As shown on Figure 3.12, this area A_c strongly depends on the location of cavities and can be obtained from the images, so that

$$F_P = A_c(P_{atm} - P_b), \quad (3.5)$$

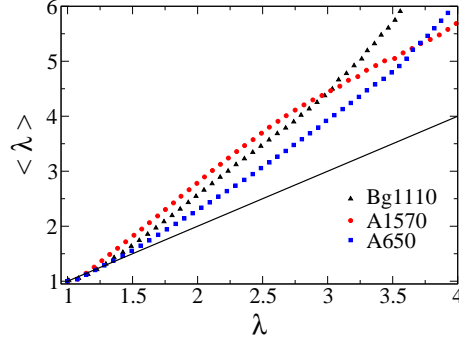


FIGURE 3.13 – Effective elongation $\langle \lambda \rangle$ versus nominal elongation λ for the three materials at a pulling velocity of $10 \mu\text{m s}^{-1}$. The black line is a guide for the eye with slope one.

where P_b is the pressure inside the cavities and P_{atm} is the atmospheric pressure. As P_b is of the order of magnitude of the vapor pressure, $P_{atm} \gg P_b$ and equation (3.5) reduces to (Poivet et al., 2004)

$$F_P \sim A_c P_{atm}. \quad (3.6)$$

Although it is obvious that this crude calculation of the pressure field is not accurate in the nucleation region (before and around the force peak), it gives a good approximation after the force peak when many cavities are growing simultaneously in size.

We can then deduce $F_m = F_T - F_P$ and calculate the effective tensile component of the viscous stress in the slice where the cavities have their maximal diameter (i.e. where the projected area of the walls between cavities is minimum)

$$\sigma_e = \frac{F_m}{A_e}. \quad (3.7)$$

where $A_e = A_0 - A_b$.

3.4.5 Effective elongation

To plot an effective stress versus strain curve, we should not only consider an effective stress but also an effective average elongation along the tensile direction in the wall for a position in the slice where the projected area of the walls between cavities is minimum. Analogous to the correction of the nominal stress we now use the load bearing area to write the effective elongation as

$$\langle \lambda \rangle = \frac{A_0}{A_e}. \quad (3.8)$$

The effective elongation differs from the nominal elongation $\lambda = h(t)/h_0$ due to the fact that the cavities do not necessarily occupy the whole height of the

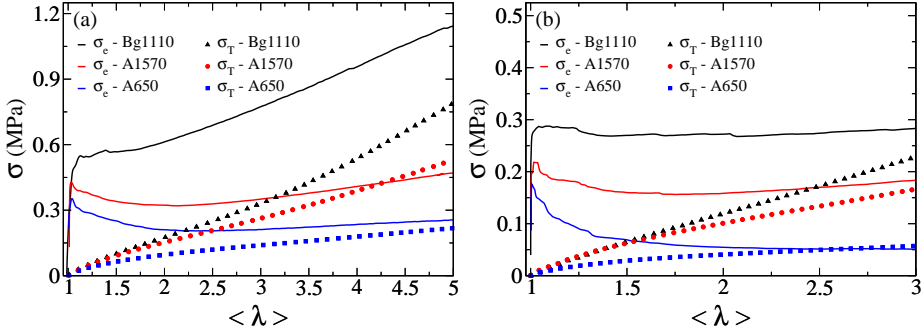


FIGURE 3.14 – Effective σ_e and true tensile σ_T stresses for the three materials at a pulling velocity of $10 \mu\text{m s}^{-1}$ (a) and $1 \mu\text{m s}^{-1}$ (b).

adhesive layer (see Figure 3.6). When considering the load bearing area, corresponding to the slice with the minimal cross section, volume conservation does not apply. $\langle \lambda \rangle$ can thus be larger compared to λ .

In Figure 3.13 this effective average value of $\langle \lambda \rangle$ is plotted as a function of the nominal λ . The results show that the effective elongation always exceeds the nominal one, suggesting a localization of the deformation in the observation plane analogous to a necking process. The necking process appears to be unstable (i.e. the slope of $\langle \lambda \rangle$ vs λ increases with increasing λ) for Bg1110 (crack propagation at the interface due to the stress concentration at the crack tip) and A650 (no strain hardening and cohesive failure) and stable for the A1570 which has the best PSA properties. This figure shows well how the elongational properties of the adhesives should be optimized. If too much elastic energy is stored during elongation, stresses at the edge of the cavities cannot relax and the cracks coalesce at a relatively low value of λ . If too little elastic energy is stored, the debonding geometry leads to necking and cohesive failure. This optimized set of properties is consistent with the PSA design rules proposed by Deplace et al. (2009a) and is also in agreement with the observations made on the growth rates from Fig. 3.11.

3.4.6 Effective stress versus effective elongation curves

We can now discuss effective stress versus effective elongation curves as presented in Figure 3.14. The initial peak present in the nominal stress is not observed anymore for the Bg1110 material and is much less pronounced for the two other materials. At 1 and $10 \mu\text{m s}^{-1}$ the effective stress for the A650 keeps decreasing after the peak and leads, eventually, to cohesive failure. For the intermediate molecular weight (A1570) the effective stress decreases first and then slightly increases while the most interesting behavior occurs for the Bg1110 where the effective stress never decreases after the peak force. One would expect the true stress to be much more directly related to the material properties

and it is clear by qualitatively comparing Figure 3.14 for example with Figure 3.4, that the elasticity influences greatly how the effective stress varies with extension. The increase in effective stress for the Bg1110 is clearly related to the cavities expanding laterally as cracks and this increase in effective stress reflects the presence of a stress concentration at the cavity edge which leads to eventual coalescence of adjacent cavities and debonding. The moderate increase in true stress of the other two materials is characteristic of the extension of the walls between cavities.

To go even further, we can finally compare the effective stress σ_e as function of $\langle \lambda \rangle$ with the true stress $\sigma_T = F/A(t)$ (which, due to incompressibility, can be calculated by $\sigma_T = \lambda \sigma_N$) obtained from the tensile test (Figure 3.4). Our correction of the stress and strain values from the debonding experiments using the load-bearing area is a first attempt to obtain effective stress strain curves that can reasonably be compared to results from material characterization obtained by traction experiments. The results of this comparison are shown on Figure 3.14a and 3.14b. Obviously the two stresses are very different at values of λ close to 1, since the degree of confinement is very high (Crosby et al., 2000; Shull and Creton, 2004). However, as the elongation of the adhesive layer increases the effective stress should become closer to the tensile stress in uniaxial extension since the walls between cavities are not confined anymore. This is qualitatively observed in Figure 3.14a and 3.14b but one should keep in mind that the stress remains highly heterogeneous in the foam structure and is far from being uniaxial. Note also that for the slow pulling speed the contribution of F_P is more important compared to the faster pulling velocity and small errors made by our approximations might thus be more important for this case. The most striking difference is between the A1570 and Bg1110 where an apparently small difference in uniaxial constitutive behavior (dotted lines on Figure 3.14a and 3.14b) leads to a much larger difference in effective stress when plotted as a function of effective elongation and finally to completely different debonding mechanisms (see Figure 3.5).

3.5 Conclusions

We have carried a systematic investigation of the kinematics of deformation of model thin adhesive layers made from acrylic pressure-sensitive adhesives, as they are debonded from a flat-ended cylindrical probe at two different probe velocities.

The rheological properties of the three adhesives were characterized in the linear viscoelastic regime and in uniaxial extension until rupture at two different strain rates. The three adhesives were chosen to show differences in mechanical behavior at low frequency in small strain and at large strain due to variable levels of molecular weight and chain branching.

The debonding of the layer from the probe occurred through the nucleation and growth of cavities which then led to an elongated foam structure. However, the relationship between the applied force and the nominal elongation were

markedly different for the three adhesives representative of behaviors spanning from too liquid-like to too solid-like.

The kinematics of the deformation of the layer was characterized by image analysis as a function of time and the three materials were systematically compared. The average shape of the cavities nucleating during debonding and the total projected area of the cavities in the plane of the adhesive film were characterized quantitatively for all three materials at two different velocities. Very few differences in the overall projected area were observed at $V = 10 \mu\text{m s}^{-1}$. However, cavities were more spherical projected area for the more elastic adhesive at $1 \mu\text{m s}^{-1}$ while cavities were the most irregularly shaped for the lower molecular weight adhesive. Furthermore an estimate of the local tensile strain in the plane of observation showed that the local tensile strain systematically exceeds the nominal strain and diverges for the lowest molecular weight (leading to cohesive debonding) and the most elastic adhesive (leading to interfacial failure by crack propagation) and was only stable for the intermediate adhesive showing the best PSA properties.

The kinematic information was used to calculate for the first time to our knowledge the effective stress as a function of time in the stage where cavities grow mostly in the plane of the film and are not yet very elongated in the tensile direction. While this effective stress drops after the peak force for the two uncrosslinked materials, it keeps increasing after the peak force for the Bg1110. Such a qualitative difference leads to an entirely different debonding mechanism, with stable fibrils for the two uncross-linked materials and crack coalescence for the more elastic Bg1110.

These results show that small differences in rheological properties in small and in particular large strain, lead to significant changes in the kinematics of deformation under the same applied boundary conditions, which then has a great influence on the work on debonding. This coupling between rheological properties and kinematics is a great challenge for modeling soft materials and we hope that our results will be the base of comparison with simulations of computational fluid mechanics using realistic material properties.

This chapter focused on the early stages of the formation of cavities leading to fibrils and helped to discriminate the transition from interfacial crack propagation to bulk deformation. In order to understand better the transition between adhesive and cohesive debonding, we need a way to predict the behavior of materials at large strains at different strain rates. Thus, we will discuss in the next chapter a way to model our materials under uniaxial deformation in order to extract key parameters to predict the transition between adhesive and cohesive failure.

Bibliographie

- Brown, K., Hooker, J. C., and Creton, C. (2002). Micromechanisms of Tack of Soft Adhesives Based on Styrenic Block Copolymers. *Macromol. Mater. Eng.*, 287 :163–179.
- Chiche, A., Dollhofer, J., and Creton, C. (2005). Cavity growth in soft adhesives. *Eur. Phys. J. E*, 17 :389–401.
- Chikina, I. and Gay, C. (2000). Cavitation in Adhesives. *Phys. Rev. Lett.*, 85 :4546–4549.
- Creton, C. and Lakrout, H. (2000). Micromechanics of flat–probe adhesion tests of soft viscoelastic polymer films. *J. Polym. Sci. Pol. Phys.*, 38 :965–979.
- Crosby, A. J., Shull, K. R., Lakrout, H., and Creton, C. (2000). Deformation and failure modes of adhesively bonded elastic layers. *Journal of Applied Physics*, 88(5) :2956–2966.
- Deplace, F., Carelli, C., Mariot, S., Retsos, H., Chateauminois, A., Ouzineb, K., and Creton, C. (2009a). Fine tuning the adhesive properties of a soft nanostructured adhesive with rheological measurements. *The Journal of Adhesion*, 85(1) :18–54.
- Deplace, F., Rabjohns, M. A., Yamaguchi, T., Foster, A. B., Carelli, C., Lei, C.-H., Ouzineb, K., Keddie, J. L., Lovell, P. A., and Creton, C. (2009b). Deformation and adhesion of a periodic soft-soft nanocomposite designed with structured polymer colloid particles. *Soft Matter*, 5(7) :1440.
- Dollhofer, J., Chiche, A., Muralidharan, V., Creton, C., and Hui, C.-Y. (2004). Surface energy effects for cavity growth and nucleation in an incompressible neo-Hookean material – modeling and experiment. *Int. J. Solids Struct.*, 41 :6111–6127.
- Francis, B. A. and Horn, R. G. (2001). Apparatus-specific analysis of fluid adhesion measurements. *J. Appl. Phys.*, 89 :4167–4174.
- Josse, G., Sergot, P., Creton, C., and Dorget, M. (2004). Measuring interfacial adhesion between a soft viscoelastic layer and a rigid surface using a probe method. *J. Adhesion*, 80 :87–118.
- Lakrout, H., Sergot, P., and Creton, C. (1999). Direct observation of cavitation and fibrillation in a probe tack experiment on model acrylic pressure-sensitive adhesives. *The Journal of Adhesion*, 69(3) :307.
- Mohite, L. V., Auhl, D., Ahmadi, M., Tanguy, F., Creton, C., Padding, J. T., and Bailly, C. (2013). Rheological Characterization of Acrylic Acid Functionalized Polybutylacrylates for Pressure Sensitive Adhesives in Shear and Uniaxial Elongational Flow. *submitted to J. Rheol.*

- Nase, J., Creton, C., Ramos, O., Sonnenberg, L., Yamaguchi, T., and Lindner, A. (2010). Measurement of the receding contact angle at the interface between a viscoelastic material and a rigid surface. *Soft Matter*, 6 :2685–2691.
- Nase, J., Derks, D., and Lindner, A. (2011). Dynamic evolution of fingering patterns in a lifted Hele–Shaw cell. *Phys. Fluids*, 23 :123101.
- Nase, J., Lindner, A., and Creton, C. (2008). Pattern Formation during Deformation of a Confined Viscoelastic Layer : From a Viscous Liquid to a Soft Elastic Solid. *Phys. Rev. Lett.*, 101 :074503.
- Peykova, Y., Guriyanova, S., Lebedeva, O. V., Diethert, A., Müller-Buschbaum, P., and Willenbacher, N. (2010). The effect of surface roughness on adhesive properties of acrylate copolymers. *Int. J. Adhes. Adhes.*, 30 :245–254.
- Peykova, Y., Lebedeva, O. V., Diethert, A., Müller-Buschbaum, P., and Willenbacher, N. (2012). Adhesive properties of acrylate copolymers : Effect of the nature of the substrate and copolymer functionality. *International Journal of Adhesion and Adhesives*, 34(0) :107–116.
- Poivet, S., Nallet, F., Gay, C., and Fabre, P. (2003). Cavitation-induced force transition in confined viscous liquids under traction. *Europhysics Letters (EPL)*, 62(2) :244–250.
- Poivet, S., Nallet, F., Gay, C., Teisseire, J., and Fabre, P. (2004). Force response of a viscous liquid in a probe-tack geometry : Fingering versus cavitation. *The European Physical Journal E*, 15(2) :97–116.
- Shull, K. R. and Creton, C. (2004). Deformation behavior of thin, compliant layers under tensile loading conditions. *Journal of Polymer Science-B-Polymer Physics Edition*, 42(22) :4023–4043.
- Shull, K. R., Flanagan, C. M., and Crosby, A. J. (2000). Fingering instabilities of confined elastic layers in tension. *Physical Review Letters*, 84(14) :3057–3060.
- Teisseire, J., Nallet, F., Fabre, P., and Gay, C. (2007). Understanding Cracking Versus Cavitation in Pressure–Sensitive Adhesives : The Role of Kinetics. *J. Adhesion*, 83 :613–677.
- Tirumkudulu, M., Russell, W. B., and Huang, T. J. (2003). On the measurement of “tack” for adhesives. *Phys. Fluids*, 15 :1588–1605.
- Urahama, Y. (1989). Effect of Peel Load on Stringiness Phenomena and Peel Speed of Pressure–Sensitive Adhesive Tape. *J. Adhesion*, 31 :47–58.
- Yamaguchi, T., Koike, K., and Doi, M. (2007). In situ observation of stereoscopic shapes of cavities in soft adhesives. *Europhys. Lett.*, 77 :64002.
- Yamaguchi, T., Morita, H., and Doi, M. (2006a). Debonding dynamics of pressure–sensitive adhesives : 3D block model. *Eur. Phys. J. E*, 21 :331–339.

- Yamaguchi, T., Morita, H., and Doi, M. (2006b). Modeling on debonding dynamics of pressure-sensitive adhesives. *Eur. Phys. J. E*, 20 :7–17.
- Zosel, A. (1985). Adhesion and tack of polymers : Influence of mechanical properties and surface tensions. *Colloid Polym. Sci.*, 263 :541–553.
- Zosel, A. (1998). The effect of fibrillation on the tack of pressure sensitive adhesives. *Int. J. Adhes. Adhes.*, 18 :265–271.

Chapitre 4

Modeling viscoelastic materials used as PSAs

Contents

3.1	Introduction	87
3.2	High resolution observation and numerical analysis	88
3.2.1	Probe-Tack tests coupled with microscope	88
3.2.2	Image Analysis	89
3.3	Material Properties	91
3.3.1	Mechanical properties	91
3.3.2	Adhesion properties	92
3.4	Analysis of the debonding structure	94
3.4.1	Evolution of the load-bearing area	94
3.4.2	Projected shape of cavities	97
3.4.3	Growth rate of individual cavities	97
3.4.4	Effective Normal Stress	100
3.4.5	Effective elongation	102
3.4.6	Effective stress versus effective elongation curves	103
3.5	Conclusions	104

4.1 Introduction

As we presented in Chapter 1, acrylic polymers used as PSAs are usually weakly cross-linked in order to dissipate energy while having enough elasticity to obtain an adhesive debonding and resist creep. We discussed in section 1.5 numerous models that exist to describe viscous, hyperelastic and viscoelastic materials. Relatively simple models coupling a viscoelastic component with a hardening one can fit uniaxial deformation for some cross-linked PSAs (Deplace et al., 2009), but these models are not robust when strain rate is changed. Some of these models have been used to simulate polymer melts in extension, but none of these materials were as representative of PSA as the current materials that we used here and none had acrylic acid as a comonomer (Christensen and McKinley, 1998; Christensen and Carlyleflint, 2000; Du et al., 2004; Jensen et al., 2009a)

The materials described in Chapter 2, mostly uncross-linked, show a high dependence on strain rate and no obvious effect of finite extensibility of the polymer chains. This behavior is not described by hyperelastic models. Viscoelastic models with a non-linear contribution such as the UCM, PTT or Giesekus models discussed in section 1.5.3 of chapter 1 could be interesting if their number of modes was limited. But in most cases, they are not developed in the literature for simple flows such as uniaxial deformation under constant or varying strain rate. Moreover, these models have not been used to simulate soft materials representative of PSAs with extremely long relaxation times as our materials are. Finally, the parameters obtained from these fits and their relation with material properties have rarely been discussed.

In this chapter, we will show the relevance of using a 2-mode PTT model for the uniaxial deformation of the materials described in Chapter 2 and will develop this model specifically to fit experimental data obtained in that geometry. A discussion on the mathematical aspects of this model will be done. Then, this model will be used to fit experimental data of tensile tests and extensional rheology and parameters values will be discussed. Finally, the model will be used to simulate tensile test on a wide range of strain rate and predict from these simulations the transition between adhesive and cohesive debonding.

4.2 Experimental section

In order to characterize the non-linear viscoelastic properties of our samples and fit our model to them, tensile tests and extensional rheology tests were carried out. The details of the protocol used to make these tests as well as the discussion on the properties of the materials has already been done in Chapter 2. We recall here the governing equations of the experiments, especially their key differences.

The velocity field of a simple uniaxial elongation along the 1 direction with

a strain rate $\dot{\epsilon}_H$ is

$$\vec{v} \equiv (v_1, v_2, v_3) = \frac{\dot{\epsilon}_0}{2}(2x_1, -x_2, -x_3), \quad (4.1)$$

hence, for this shear-free flow the rate-of-strain tensor assumes a diagonal form :

$$\dot{\gamma} = (\nabla \vec{v} + \nabla \vec{v}^T) = \dot{\epsilon}_0 \begin{pmatrix} 2 & 0 & 0 \\ 0 & -1 & 0 \\ 0 & 0 & -1 \end{pmatrix} = \dot{\epsilon}_0 \mathbf{A}. \quad (4.2)$$

In these experiments, force is measured as a function of the displacement, and both measurements can be normalized to stress and strain. Since different definitions of stress and strains exist and are used in different communities, we will first discuss them and define the notation. Within the context of uniaxial extension, let l_0 be the initial length of the sample, $l(t)$ its length at a given time, $F(t)$ the force applied to the sample, S_0 the initial cross-section, and $S(t)$ the cross-section at a given time.

Two different definitions can be used for the strain : the nominal or engineering strain

$$\epsilon_N = (l - l_0)/l_0, \quad (4.3)$$

which is typically used for infinitesimal strains and is more common in the solid mechanics community, and the Hencky strain ϵ_H defined by incremental displacements, i.e. $\delta\epsilon_H = \delta l/l$ which is commonly used in the fluid mechanics community. The relation between Hencky and nominal strain is easily obtained through the integration of $\delta\epsilon_H$ from the initial to the final length of the sample

$$\epsilon_H = \int_{l_0}^l \frac{\delta l'}{l'} = \ln(1 + \epsilon_N) = \ln \lambda, \quad (4.4)$$

where λ is the stretch of the sample. Hencky and nominal strain rates are obtained from the time differentiation of Eq. (4.3) and (4.4), respectively.

In the same manner, nominal and true stress are calculated from the initial and final cross-section, i.e. $\sigma_N = F/S_0$ and $\sigma_T = F/S$. The onset of extensional viscosity η_E^+ is usually defined for tests at constant strain rate, such as extensional rheology, and is defined as the ratio between the true stress and the Hencky strain rate, i.e. $\eta_E^+(t) = \sigma_T/\dot{\epsilon}_0$. It is typically increasing with time and for a viscoelastic fluid that does not exhibit strain hardening, tends toward a constant value called eta sub E, i.e. the extensional viscosity.

In order to characterize the uniaxial extension of our materials at a constant Hencky strain rate, tests were carried out with an Extensional device adapted to a conventional rheometer (SER-2 and MCR-301 Anton Paar) already presented in Chapter 2, section 2.4.3, p.63. All tests were performed at room temperature, with strain rates of 0.01 s^{-1} , 0.1 s^{-1} , and 1 s^{-1} .

Another technique widely used to characterize solid materials in uniaxial deformation is the tensile test. This test was also presented in Chapter 2, section 2.4.3, p.62 We imposed two different cross-head velocities, 1.5 and 0.15 mm s^{-1} ,

for samples with an initial length of 15 mm, resulting in α equal to 1.0 and 0.1 s^{-1} , respectively.

While tensile tests and extensional rheology have the same geometry (uniaxial elongation), their principal difference resides in the strain-rate history applied to the sample. From the relation between nominal and Hencky strain we see that, for the tensile test, $\dot{\epsilon}_H$ is clearly time dependent

$$\dot{\epsilon}_H = \frac{\alpha}{1 + \alpha t}. \quad (4.5)$$

As shown in Fig. 4.1, during this test $\dot{\epsilon}_H$ dramatically decreases up to a value of the strain rate that is one order of magnitude smaller than the initial strain rate for a sample stretched ten times its original length.

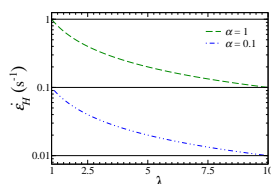


FIGURE 4.1 – Comparison of $\dot{\epsilon}_H$ vs time for extensional rheology (black solid lines) and tensile tests (green dashed and blue dashed-dotted lines) for the different tests.

4.3 Modeling uniaxial deformation of PSAs : choice of a convenient model

4.3.1 Choice of a convenient model for PSAs under uniaxial deformation

We discussed in the state of the art, section 1.5 (p.36) the different possible strategies to model deformations and flows, from the Newtonian liquid or elastic solid to complex viscoelastic flows. Previous successful attempts at describing the large-strain behavior of waterborne PSAs (Deplace et al., 2009) were based on a parallel combination of a viscoelastic model (Upper Convected Maxwell model (Bird et al., 1977) and an elastic model (Gent strain-hardening model (Gent, 1996)) suggesting a hybrid approach to model the PSAs considered in this work. Other contributions focused on modeling viscoelastic fluid polymers (Christensen and McKinley, 1998; Christensen and Carlyleflint, 2000; Du et al., 2004; Jensen et al., 2009b) typical of hot melts but not adapted to materials with very long relaxation times as our model materials show.

Examining the uniaxial deformation data of our materials, we can discuss what models are most appropriate to properly fit them.

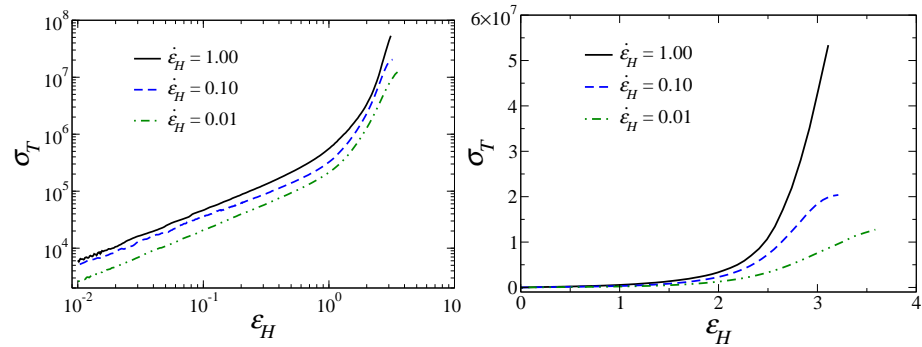


FIGURE 4.2 – Comparison of true stress versus strain for A1570 at three different strain rates for extensional rheology tests. (a) : The axis are in logarithmic scale to show the vertical shift of the linear part (short times). (b) : axis in linear scale. Note the different hardening behavior depending on the strain rate.

The linear response of the extensional viscosity plot (short times), or, equivalently, the stress responses to small deformations, shows that curves from extensional rheology cannot be collapsed in a master curve that depends only on the strain applied to the sample, as shown by the vertical offset of the curves in Fig. 4.2 (a) for A1570. This eliminates purely hyperelastic models and leads toward a viscoelastic model to capture the linear part. Also the strain hardening behavior cannot be reminiscent of a purely hyperelastic model : As shown in Fig. 4.2 (b), this material hardens differently depending on the strain rate and does not start to deviate from the linear prediction for the same value of ϵ_H . The large strain behavior can only be captured with a viscoelastic component which depends on strain and strain rate.

A possible strategy could be to use a multimode viscoelastic fluid model combined with a finite extensibility hyperelastic model to catch both the linear regime and the strain hardening behavior for the range of strain rates of our data, i.e. using one mode for each strain rate. This physically based approach would clearly lead to a proliferation of fitting parameters that would be useful for accurate 3-D simulations but would remove any physical meaning from the different modes and their respective parameters.

In two recent studies, Padding *et al.* were able to model the A1570 material at the mesoscopic scale (Padding *et al.*, 2011, 2012). Numerical simulations with the Responsive Particle Dynamics (RaPiD) method Briels (2009) gave quantitative predictions of the nonlinear rheology of pressure sensitive adhesives after fitting several model parameters from data obtained with linear rheology experiments. The RaPiD formalism introduces transient forces related to the degrees of freedom that have been eliminated by the coarse-graining procedure. In (Padding *et al.*, 2011, 2012) the authors show that transient forces due to slow chain intermixing and changes in the number of sticker groups shared

among particles are key factors in order to describe correctly the experimental rheology of PSAs. Moreover, these forces act at two separate time scales, with a difference between their relaxation times of three orders of magnitude. This approach shows that our materials have two different dynamics, and could thus be modeled using a 2-modes viscoelastic model.

As discussed in section 1.5.3 (44), the Upper-Convected Maxwell is a good candidate to model materials with non-linear dependence of stress and strain. However in order to avoid computing issues due to the divergence of the UCM model, we will use a variation of the UCM which was proposed in the late 70's, the Phan-Thien-Tanner (PTT) model (Phan-Thien and Tanner, 1977; Phan-Thien, 1978) with two modes.

4.4 The PTT Model : Mathematical aspects

The one-mode PTT model is characterized by four parameters. Two of them have a direct physical meaning, i.e. the relaxation time τ and the viscosity η , while the other two, ϵ and ξ , are derived from the response of the entangled structure to the external flow. The strength of the nonlinear response of the network to large perturbations is tuned by the value of ϵ . Finally, ξ captures the non-affine motion of the network with respect to the superimposed flow. Although this is a relevant parameter for shear flows, in the case of a shear-free flow, such as the uniaxial elongation tests taken into account here, it loses its relevance. Typically, ϵ ranges between 0.01 and 0.1.

4.4.1 Application of the PTT model to the uniaxial flow

We consider here a form of the PTT model using the Bird's notation for stress tensors (Bird et al., 1977), which gives for the time evolution of the stress tensor $\boldsymbol{\sigma}$:

$$\boldsymbol{\sigma} e^{-\epsilon\tau\hat{E}\text{Tr}(\boldsymbol{\sigma})/\eta} + \tau \left[\boldsymbol{\sigma}_{(1)} + \frac{\xi}{2} (\dot{\boldsymbol{\gamma}} \cdot \boldsymbol{\sigma} + \boldsymbol{\sigma} \cdot \dot{\boldsymbol{\gamma}}) \right] = -\eta \dot{\boldsymbol{\gamma}}. \quad (4.6)$$

In this equation the notation $\boldsymbol{\sigma}_{(1)}$ stands for the Upper Convected Maxwell derivative of the stress tensor

$$\boldsymbol{\sigma}_{(1)} = \partial_t \boldsymbol{\sigma} + \vec{v} \cdot \nabla \boldsymbol{\sigma} - \nabla \vec{v}^T \cdot \boldsymbol{\sigma} - \boldsymbol{\sigma} \cdot \nabla \vec{v}, \quad (4.7)$$

and $\text{Tr}(\cdot)$ is the trace operator.

The system (4.6) is a system of partial differential equations that requires a full space-time integration to get the history of the stresses in case of a complex flow. For a simple flow it reduces to a system of ordinary differential equations. In fact, in our case the flow in uniaxial elongation (4.1) satisfies the condition $\nabla \vec{v} = \nabla \vec{v}^T$. Moreover, in this particular circumstance, the model preserves any isotropic initial condition, i.e. for any $t > 0$, $\nabla \boldsymbol{\sigma}(t) = 0$ if $\nabla \boldsymbol{\sigma}(0) = 0$. Eq. (4.6) simplifies to

$$\boldsymbol{\sigma} e^{-\epsilon\tau\text{Tr}(\boldsymbol{\sigma})/\eta} + \tau [\dot{\boldsymbol{\sigma}} + \dot{\epsilon}_0(\xi - 1) \boldsymbol{\sigma} \cdot \mathbf{A}] = -\eta \dot{\epsilon}_0 \mathbf{A}, \quad (4.8)$$

where $\dot{\sigma}$ is the time derivative of the stress tensor. Note that due to the flow structure there are only two independent components of the stress tensor ($\sigma_{33} = \sigma_{22}$)

$$\tau \dot{\sigma}_{11} = \left[2\tau \dot{\epsilon}_0 (1 - \xi) - e^{-\epsilon\tau(\sigma_{11} + 2\sigma_{22})/\eta} \right] \sigma_{11} - 2\eta \dot{\epsilon}_0, \quad (4.9)$$

$$\tau \dot{\sigma}_{22} = - \left[\tau \dot{\epsilon}_0 (1 - \xi) + e^{-\epsilon\tau(\sigma_{11} + 2\sigma_{22})/\eta} \right] \sigma_{22} + \eta \dot{\epsilon}_0. \quad (4.10)$$

These differential equations are coupled (see $(\sigma_{11} + 2\sigma_{22})$ in each exponential term) leading to a system that does not have an analytical solution. Nevertheless, numerical integration of Eqs. (4.9)-(4.10) can be straightforwardly performed with standard solvers such as a fourth order Runge-Kutta routine (Press et al., 2007).

4.4.2 Asymptotic behavior

Before working on a numerical solution, we can study the asymptotic behavior at short and long times by developing our model in a rather simple case : uniaxial deformation at a constant strain rate, i.e. $\dot{\epsilon}_H = \dot{\epsilon}_0$ (elongational rheology experiment).

Linear part

The Eqs. (4.9)-(4.10) contain a non-linear part in the exponential term. If we neglect this term, the model can be simplified. We will show later that this term can effectively be neglected at short times, i.e small strain, and that its contribution can be easily studied at large strain. In this case, Eqs. (4.9)-(4.10) can be simplified as

$$\tau \dot{\sigma}_{11} = [2\tau \dot{\epsilon}_0 (1 - \xi) - 1] \sigma_{11} - 2\eta \dot{\epsilon}_0, \quad (4.11)$$

$$\tau \dot{\sigma}_{22} = - [\tau \dot{\epsilon}_0 (1 - \xi) + 1] \sigma_{22} + \eta \dot{\epsilon}_0, \quad (4.12)$$

This set of uncoupled linear differential equations is easily solved for a constant strain rate $\dot{\epsilon}_0(t) = \dot{\epsilon}_0$, taking into account the general solution of the equation

$$\dot{f}(t) = af(t) + b \quad \rightarrow \quad f(t) = C_1 e^{at} - \frac{b}{a}, \quad (4.13)$$

with initial condition $f(0) = 0$, so that $C_1 = b/a$. we obtain an analytical solution :

$$\sigma_{11} = \frac{2\eta \dot{\epsilon}_0}{1 - 2w} \left[e^{(1-2w)t/\tau} - 1 \right], \quad (4.14)$$

$$\sigma_{22} = \frac{\eta \dot{\epsilon}_0}{1 + w} \left[1 - e^{-(w+1)t/\tau} \right], \quad (4.15)$$

where we have introduced a reduced Deborah number $w = \tau \dot{\epsilon}_0 (1 - \xi)$ that accounts for the non-affine motion of the network with respect to the imposed external flow. We can note that the σ_{11} solution is singular for $w = 1/2$ due to the cancellation of the first term of the right side of Eq. (4.11), and, for this value of w , the solution is $\sigma_{11} = -2\eta \dot{\epsilon}_0 t / \tau$ provided $\sigma_{11}(0) = 0$. We will study the behavior of the solutions for $w < 1/2$ and $w > 1/2$. σ_{22} is singular for $w = -1$, which can only occur for a uniaxial compression. We will not discuss this singularity as we only study uniaxial extension.

From the definition of the elongational viscosity following Bird's notation (Bird et al., 1977) $\eta^+ = -(\sigma_{11} - \sigma_{22})/\dot{\epsilon}_0$, we get

$$\eta^+ = \hat{\eta} \left[3 + \frac{2w - 1 - 2e^{3wt/\tau}(w + 1)}{e^{(w+1)t/\tau}} \right], \quad (4.16)$$

with $\hat{\eta} = \eta/(1 - \omega - 2\omega^2)$.

The true stress is simply obtained by $\sigma_T = -(\sigma_{11} - \sigma_{22})$, giving

$$\sigma_T = \hat{\eta} \dot{\epsilon}_0 \left[3 + \frac{2w - 1 - 2e^{3wt/\tau}(w + 1)}{e^{(w+1)t/\tau}} \right], \quad (4.17)$$

The linear part of the PTT model is exactly the Upper Convected Maxwell model when $\xi = 0$.

We will now use the elongational viscosity defined in Eq. (4.16) to study the limiting behavior at short and long times noting that the true stress σ_T has the same behavior as it is related to η^+ by $\sigma_T = \eta^+ \dot{\epsilon}_0$.

Eq. (4.16) can be rewritten to let appear more clearly the two exponential terms and examine their limiting behavior :

$$\eta^+ = \hat{\eta} \left[3 + \frac{2w - 1}{e^{(w+1)t/\tau}} - 2e^{(2w-1)t/\tau}(w + 1) \right], \quad (4.18)$$

Asymptote for short times

We study now the linearized PTT model for small values of t/τ . Expanding the exponentials up to first order we have

$$e^{-(w+1)t/\tau} \sim 1 - (w + 1)\frac{t}{\tau}, \quad \text{and} \quad e^{(2w-1)t/\tau} \sim 1 + (2w - 1)\frac{t}{\tau}, \quad (4.19)$$

so that for $t/\tau \ll 1$ we obtain

$$\eta^+ \sim \hat{\eta} \left[3 + (2w - 1)\left(1 - (w + 1)\frac{t}{\tau}\right) - 2\left(1 + (2w - 1)(w + 1)\frac{t}{\tau}\right) \right], \quad (4.20)$$

so that

$$\eta^+ \sim \hat{\eta} \left[3 - 3w - 6w^2 \right] \frac{t}{\tau}, \quad (4.21)$$

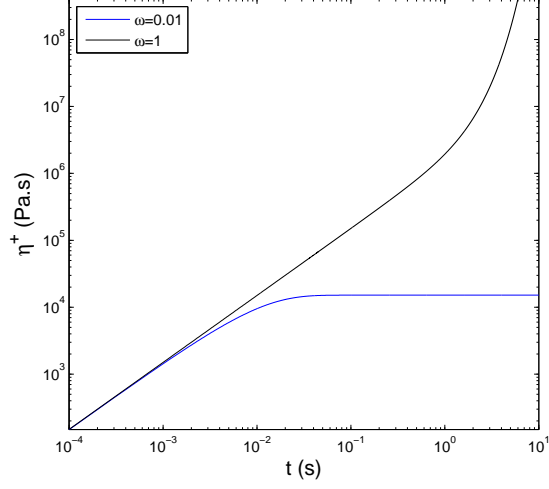


FIGURE 4.3 – Linear part of the PTT model for $\dot{\epsilon}_0 = 10$, $G = \eta/\tau = 5.0 \cdot 10^6 \text{ Pa}$ and $\tau = 0.01$ or $\tau = 1$, leading respectively to $\omega = 0.1 < 1/2$ and $\omega = 10 > 1/2$

and finally

$$\eta^+ \sim 3\eta \frac{t}{\tau}. \quad (4.22)$$

We conclude that, under the assumption that the non-linear part of the model can be neglected at short times, η^+ increases linearly with time with a $3G$ slope, with G the modulus defined as $G = \eta/\tau$.

Limiting behavior at long times

In our case $w > 0$, so for the first exponential term of (4.18) :

$$\lim_{t \rightarrow \infty} \frac{2w-1}{e^{(w+1)t/\tau}} = 0, \quad \forall w. \quad (4.23)$$

The second exponential contribution in (4.18) has two possible limits :

$$\lim_{t \rightarrow \infty} e^{(2w-1)t/\tau} (w+1) = 0, \quad \forall w < 1/2, \quad (4.24)$$

and

$$\lim_{t \rightarrow \infty} e^{(2w-1)t/\tau} (w+1) = \infty, \quad \forall w > 1/2. \quad (4.25)$$

Therefore the elongational viscosity has two possible limits :

$$\lim_{t \rightarrow \infty} \eta^+ = 3\hat{\eta}, \quad \forall w < 1/2, \quad (4.26)$$

and

$$\lim_{t \rightarrow \infty} \eta^+ = \infty, \quad \forall w > 1/2. \quad (4.27)$$

The limiting behaviors discussed above are confirmed when we plot the linear part of this model, see Fig. 4.3. At short times, The slope is equal to $3G$ ($G = 5.0 \cdot 10^6 Pa$ for both curves) and the viscosity at long times is either infinite when $\omega > 1/2$ or a constant value equal to $3\hat{\eta}$ when $\omega < 1/2$.

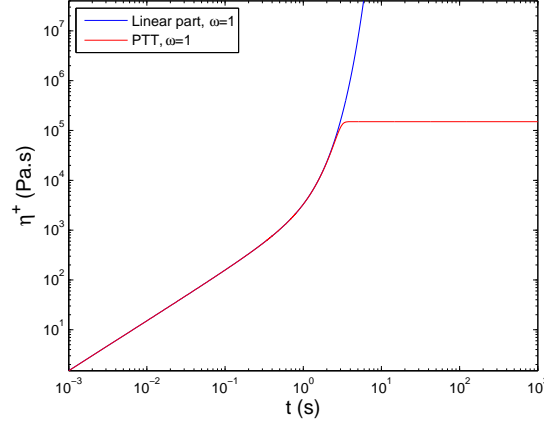


FIGURE 4.4 – Linear part of the PTT model for $\dot{\epsilon}_0 = 10$, $G = \eta/\tau = 5.0 \cdot 10^6 Pa$ and $\tau = 0.01$ or $\tau = 1$, leading respectively to $\omega = 0.1 < 1/2$ and $\omega = 10 > 1/2$

Contribution of the non-linear term

While we do not have an analytic solution for the PTT model, we can observe that the non-linear term neglected in the previous section is a negative exponential that will tend toward 0 for high values of $\epsilon\tau(\sigma_{11} + 2\sigma_{22})$, avoiding the divergence of the solution when $w > 1/2$ and having no contribution when $w < 1/2$. Hence, we can deduce that the parameter ϵ tunes the nonlinear response of the model, and is responsible for the divergence of the model from the behavior predicted by the linearized PTT model.

This is shown on Fig. 4.4 where the linear part of the model is plotted together with the full PTT model (solved by numerical integration). When the viscosity reaches a given value during the exponential growth, the non-linear term compensates it to saturate the solution. We will confirm this when studying the influence of the parameter ϵ . This figure shows that, since the linearized version of the model is equivalent to the full nonlinear PTT for short times, we can use it to fit the initial slope and thus adjust the value of the modulus G .

4.4.3 PTT model under constant $\dot{\epsilon}_H$ or varying $\dot{\epsilon}_H$

As discussed in the experimental section, $\dot{\epsilon}_H$ is not constant during a conventional tensile test. The numerical integration method used for the case of a constant $\dot{\epsilon}_H$ is still valid, as long as in Eqs. (4.9)-(4.10), $\dot{\epsilon}_H$ is considered as a time-dependent variable expressed as in Eq. (4.5). Fig. 4.5 shows the predictions obtained for the same model for the two loading histories. Due to the decrease in $\dot{\epsilon}_H$ as a function of time, the resulting η^+ is similar to the case where a constant $\dot{\epsilon}_H$ is applied at short times, when the difference in $\dot{\epsilon}_H$ are negligible, and then η^+ goes through a maximum and decreases continuously. As the varying $\dot{\epsilon}_H$ illustrates a typical tensile test, we plotted the same curve in a linear scale as $\sigma_N = f(\lambda)$. In both cases, σ_N decreases continuously, but the maximal stress reached before the decrease is higher at constant strain rate, as the effective strain rate at large strain is higher.

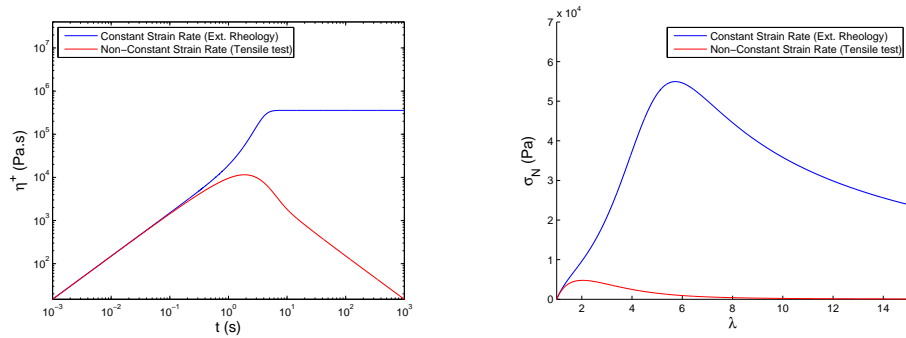


FIGURE 4.5 – PTT model for a constant $\dot{\epsilon}_H$ and $\dot{\epsilon}_H$ varying as in a tensile test, plotted as $\eta^+ = f(t)$ in log scale (left, extensional rheology), and as $\sigma_N = f(\lambda)$ (right, tensile tests).

4.4.4 Influence of the parameters on the PTT Model

Let us study the influence of the main parameters in the case of $w < 1/2$, where no exponential divergence is observed. ϵ and ξ will not be studied as the equations show that in the case of $w < 1/2$, ϵ has no impact and $(1 - \xi)$ only multiplies the linear part. The remaining factors are τ and η , their ratio being the modulus G , proportional to the slope observed at short times.

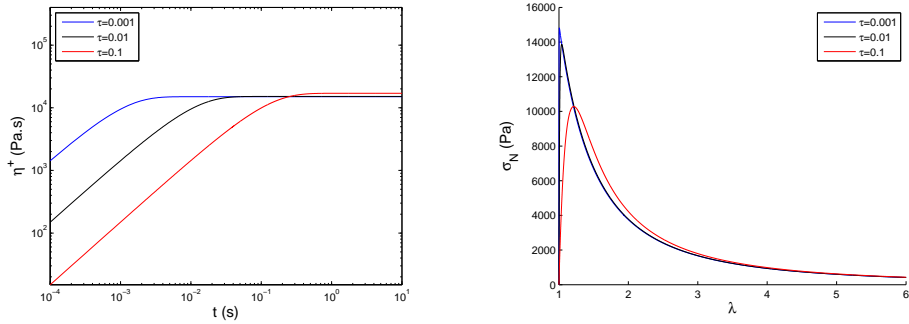
Influence of τ 

FIGURE 4.6 – Influence of τ on the PTT model for $\omega = 0.01$. On the left side, $\eta^+ = f(t)$ in a log scale, as conventionally represented in extensional rheology plots. On the right side, $\sigma_N = f(\lambda)$, as conventionally represented in tensile tests plots.

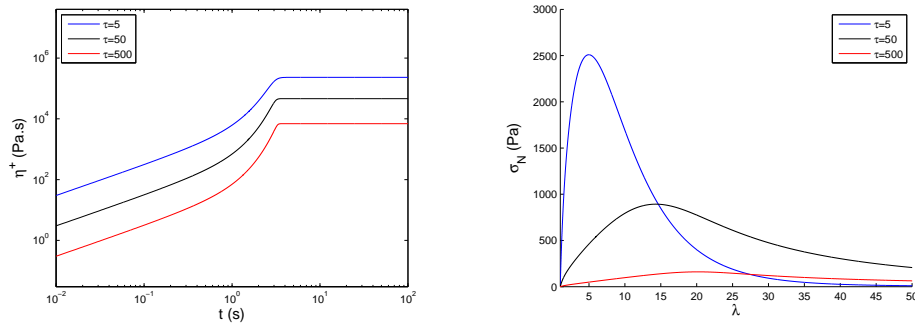


FIGURE 4.7 – Influence of τ on the PTT model for $\omega = 1$ (bottom). On the left side, $\eta^+ = f(t)$ in a log scale, as conventionally represented in extensional rheology plots. On the right side, $\sigma_N = f(\lambda)$, as conventionally represented in tensile tests plots.

Fig.4.6 shows the influence of τ for $\omega = 0.01$, in simulated curves at a constant $\dot{\epsilon}_H = 1$ and in simulated tensile test plots with $\dot{\epsilon}_H(t), \dot{\epsilon}_H(0) = 1$. When $\omega < 1/2$, the model behaves like a viscous fluid and τ dictates the time when a plateau is reached. When $\omega > 1/2$ (cf Fig. 4.7), the tensile plot shows well that τ still dictates the time of switch in the regime : the higher is τ , the latter the switch is observed. Thus, τ controls as expected the characteristic time of the system. Moreover, as $G = \eta/\tau$, the higher is τ , the lower the modulus is, as we

can observe in both cases.

Influence of η

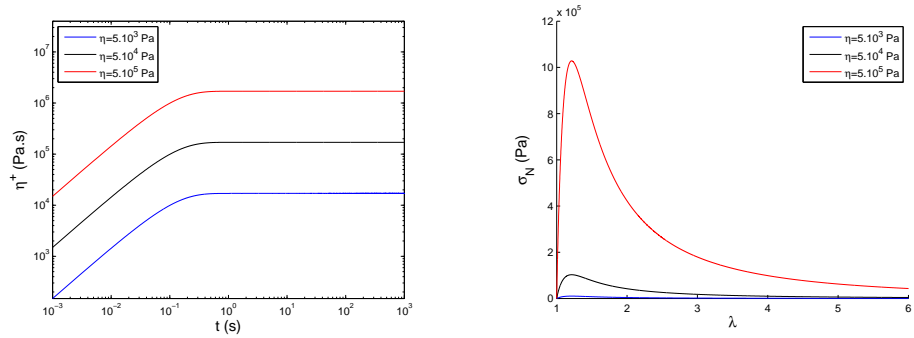


FIGURE 4.8 – Influence of η on the PTT model for $\omega = 0.01$. On the left, $\eta^+ = f(t)$ in log scale, conventional of extensional rheology plots. On the right, $\sigma_N = f(\lambda)$, conventional of tensile tests plots.

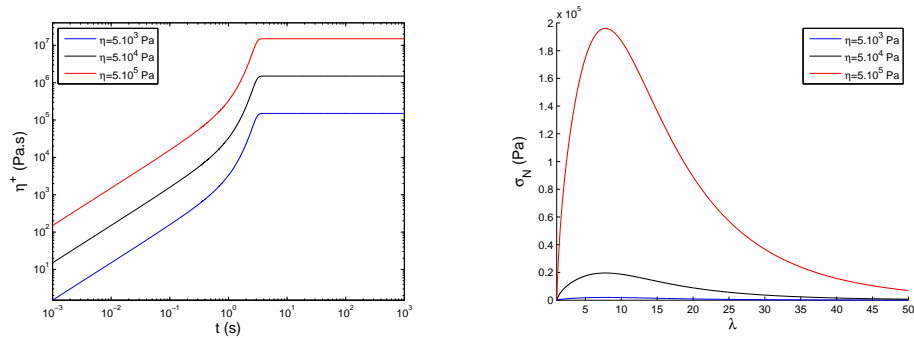


FIGURE 4.9 – Influence of η on the PTT model for $\omega = 1$. On the left, $\eta^+ = f(t)$ in log scale, conventional of extensional rheology plots. On the right, $\sigma_N = f(\lambda)$, conventional of tensile tests plots.

Fig. 4.8 and 4.8 shows the influence of η for a fixed value of ω . In the case of $\omega < 1/2$ as for $\omega > 1/2$, η influences the modulus observable in the linear part and the limiting viscosity at high strain in extensional rheology. This can be mathematically explained by its role of multiplying factor in the linearized Eqs. (4.16)-(4.17).

From the observations on the influence of η and τ , we can conclude that the initial slope observable in extensional rheology plot is dictated as expected by the ratio η/τ and that τ dictates the characteristic time.

Influence of ϵ

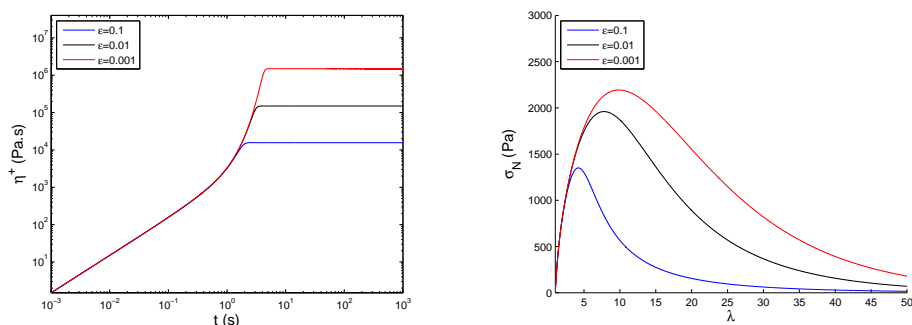


FIGURE 4.10 – Influence of τ on the PTT model for $\omega = 1$ (bottom). On the left, $\eta^+ = f(t)$ in log scale, conventional of extensional rheology plots. On the right, $\sigma_N = f(\lambda)$, conventional of tensile tests plots.

As discussed above, ϵ only appears in the non-linear exponential factor which saturates the extensional viscosity at a given value. ϵ tunes this value of saturation independently from the viscosity and the relaxation time, see Fig. 4.10.

4.5 2-modes PTT model

The PTT model presented in Eq. (4.6) can be generalized to n -modes through the principle of linear superposition

$$\boldsymbol{\sigma} = \sum_{i=1}^n \boldsymbol{\sigma}_i, \quad (4.28)$$

where the evolution of each mode does not depend on the other modes. For this reason, for every mode, its evolution equation is obtained from Eq. (4.6) by replacing $\boldsymbol{\sigma}$ for $\boldsymbol{\sigma}_i$ and the pair of parameters (τ, η) for (τ_i, η_i) . ϵ and ξ take a constant value that does not change for each mode.

Based on the experience with the coarse grained model (Padding et al., 2011, 2012) and also on the structure of our polymers which contain both entanglements and sticker groups, we decided to limit our model to two modes (cf Section 4.3.1) leading to a six parameters model.

4.5.1 Fitting strategy

The numerical integration of Eqs. (4.9)-(4.10) can be performed with standard numerical solving algorithms, such as a fourth order Runge-Kutta scheme. The parameters of the PTT model are estimated through a least squares minimization which compares the model prediction for the two types of tests (elongational rheology and tensile test) and the experimental data reported in Chapter 2. An important issue in the fitting procedure is the size of the parameter space : it grows linearly with the number of modes included in the PTT model. That is, a 2-modes PTT model lives in a parameter space with 6 dimensions. This linear dependence will limit any real possibility to straightforwardly find a global minimum.

In addition, even for the simplest one-mode model, a four dimensional space typically contains many local minima in which the numerical routine can get stuck. Hence, there are only two possibilities for the fitting procedure : i) start the fitting from a point of the parameter space picked randomly and use an algorithm that can escape from local minima or ii) employ a minimization algorithm but exploit the mathematical structure of the model and the physical knowledge of the materials to locate a starting point which is, hopefully, inside the area of attraction of the global minimum. We decided to use the second option because it requires less code development and calculation time compared to the first one.

Fitting was done by numerically solving the equations (4.9)-(4.10) and using a classical minimization procedure by defining the objective function :

$$f(x) = \frac{|\eta_{PTT}^+ - \eta_{exp}^+|}{\eta_{exp}^+}. \quad (4.29)$$

The procedure used was to first fit together two tensile tests experiments with two different initial Hencky strain $\dot{\epsilon}_H$, using as a starting point an estimate of the modulus obtained directly from the linear part. Then, parameters were adjusted on extensional rheology experiments, by fitting with the three experiments at the same time again. It was decided to neglect the role of ξ ($\xi = 0$), as this parameter plays a major role in more complex flows than uniaxial deformation and is here only a proportional contribution to $\tau\dot{\epsilon}_0$. Moreover, we decided to fix $\epsilon = 0.01$. the fitting parameters were then only eta and tao for the two modes.

4.5.2 Results and discussion

The fitting procedure was carried out on the five model materials : A1570, A1070, A650, B1080 and Bg1110 presented in Chapter 2. The parameters obtained are summarized in Table 4.1. Fig.4.13 shows experimental results and simulations curves. A good agreement is obtained for the five materials for the strain hardening part, but with a systematic under-estimate of the viscosity in the linear regime. This may be due to the focus of our strategy on the non-linear behavior by initiating the fits on the tensile test curves (left figures).

Material	τ_1 (s)	η_1 (Pa.s)	G_1 (Pa)	τ_2 (s)	η_2 (Pa.s)	G_2 (Pa)
Bg1110	494.29	1.89E+07	3.82E+04	7.37	2.26E+05	3.07E+04
B1080	2035.31	3.72E+07	1.83E+04	4.55	1.65E+05	3.64E+04
A1570	940.62	2.04E+07	2.17E+04	4.90	1.92E+05	3.91E+04
A1070	750.00	9.00E+06	1.20E+04	2.80	1.12E+05	4.00E+04
A650	490.32	5.50E+06	1.12E+04	1.75	6.94E+04	3.97E+04

TABLE 4.1 – Parameters obtained by fitting the PTT-2modes model with experimental results from tensile tests and extensional rheology.

For the five materials characterized, we obtain two characteristic times, $\tau_1 > 490s$ and $\tau_2 < 8s$. These two times can be attributed to two different dynamic processes occurring during the deformation of the polymers and which are responsible for the storage of elastic energy and for the viscoelastic behavior and strain hardening, the entanglements and the stickers. As mentioned in section 4.3.1, these two dynamics are in agreement with our knowledge of the structure of the material and with other studies realized in the MODIFY project (Padding et al., 2011, 2012). In our case, τ_2 is the characteristic time triggering elasticity due to entanglements. This is confirmed by the constant value of the modulus G_2 associated to this mode for a same family ($3.9 \cdot 10^4 Pa$ for the A series). Moreover, the value of the modulus is in semi-quantitative agreement with the values observed in the linear regime, where the stickers dynamics is negligible, see section ?? (??) : $G'(\omega)$ varies from $3 \cdot 10^{-4} Pa$ to $1 \cdot 10^{-5} Pa$ in this range of frequency, see Fig. 2.14 from Chapter 2, 68. Depending on the strain rate at which this experiment was carried out, this modulus will result in a value of ω superior or inferior to the critical value $1/2$, characterizing the transition from the linear to the non-linear regime in elongation. At high strain rates, the entanglements hinder the flow, leading to storage of elastic energy and a more solid behavior. The other characteristic time, τ_1 , describes the stickers dynamics, with a much longer characteristic time, making it relevant for high strains or low strain rates. For this mode, ω is superior to $1/2$ in all cases : this mode never flows but always renders the mechanical response more solid when in its corresponding time range.

We can make some additional comments on the values of the parameters. For the A series where we have a series of molecular weights with presumably a self similar molecular structure, G_2 is nearly constant, while G_1 is smaller and increases with molecular weight, see Fig. 4.11. This suggests indeed that the elasticity due to entanglements is the same regardless of molecular weight while the contribution due to stickers is dependent of the molecular weight at the same sticker weight concentration. The characteristic times where the elasticity kicks in depends on M_w for both characteristic times but for the strain rates that we use, τ_2 has the most influence on the behavior of the PSA.

Finally, we analyzed the viscosity η_2 linked to the entanglements dynamics,

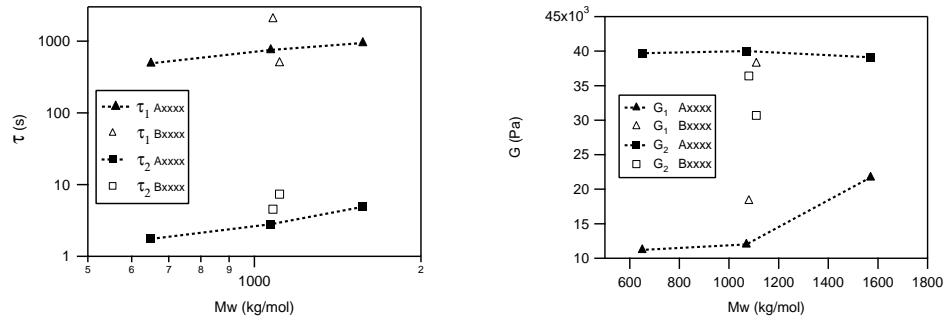


FIGURE 4.11 – Left : τ_1 and τ_2 versus M_w in log-log scale. Right : G_1 and G_2 versus M_w .

see Fig. 4.12. Interestingly, this mode roughly follows the experimental relation (Colby et al., 1987) :

$$\eta \propto M_w^{3.4} \quad (4.30)$$

derived from the tube model from Doi and Edwards (1978). This confirms that reptation dynamics of the chains are described by this mode. The viscosity of this mode is quite similar with viscosity measured by Jullian et al. (2010) on monodisperse Poly(n-Butyl acrylate) of $M_w = 220 \text{ kg/mol}$, $1.35 \cdot 10^5 \text{ Pa.s}$, especially for A1070. This mode captures the dynamics of entanglements of shorter chains than the ones constituting our polymer, while the other mode captures the sticker dynamics due to the AA functions coupled with the contribution of very long chains.

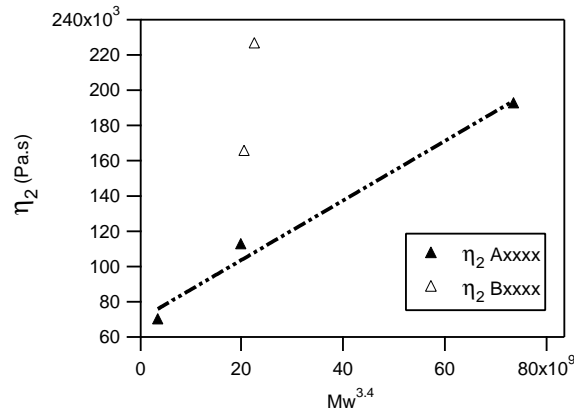


FIGURE 4.12 – η_2 versus $M_w^{3.4}$ for the A series (full triangles) and the B series (empty triangles).

4.6 Prediction of the adhesive/cohesive debonding transition of PSAs

In addition to examining the values of the fitting parameters as a function of the molecular structure of the PSA, we are also able to use the PTT model to simulate tensile tests at any strain rate. We will use this opportunity to simulate the tensile behavior of our materials at a rate equivalent to the probe-tack experiments carried out at $1\mu m.s^{-1}$, $10\mu m.s^{-1}$, $100\mu m.s^{-1}$ and $1000\mu m.s^{-1}$. Since the films used in Chapter 2 have a thickness of $100\mu m$, the approximate equivalent nominal strain rate is respectively $0.01s^{-1}$, $0.1s^{-1}$, $1s^{-1}$ and $10s^{-1}$. An example of simulation is given in Fig. 4.14, with $\sigma_N = f(\lambda)$ on the left and the Mooney representation on the right $\sigma_R = f(1/\lambda)$, with

$$\sigma_R = \frac{\sigma_N}{\lambda - \frac{1}{\lambda^2}}. \quad (4.31)$$

We find a characteristic relaxation of the stress of our materials at low strain rates and a mild hardening at higher strain rates due to the presence of the sticker groups on the polymer chains.

We saw in section 2.6.1, 69 that the C_{hard} that can be extracted from the Mooney representation could not be used for most of our materials due to the absence of strong hardening in our materials. Thus, the criterion C_{soft}/C_{hard} cannot be used as defined for our set of model materials. Yet, the Mooney plot can be used to calculate C_{soft} . Since there is no hardening part due to cross-linking on these representation for our materials (which would be seen as an upturn in σ_R with decreasing values of $1/\lambda$), we can define C_{soft} as the slope between $1/\lambda = 0.2$ and $1/\lambda = 0.99$:

$$C_{soft} = \frac{\sigma_R(0.99) - \sigma_R(0.2)}{0.99 - 0.2} \quad (4.32)$$

Although the absence of minimum in σ_R does not allow us to calculate unambiguously a value for C_{hard} , we can introduce a parameter characterizing the reduced stress at high deformation. We will call it C_{LS} for stress at large strain and we define it as :

$$C_{LS} = \sigma_R(0.2) \quad (4.33)$$

This parameter has the significance of a high strain modulus and physically represents approximately the level of elasticity left in the sample at that strain level for a test carried out at that particular strain rate. Since this is the level of strain that one expects to find in PSA fibrils near the ultimate failure of the bond, such a parameter should have a predictive value. .

C_{LS} and C_{soft} were calculated from the simulated tensile curves at the four nominal strain rates for the five materials. All the values are summarized in Fig. 4.15 where C_{soft} is plotted as a function of C_{LS} . All experiments carried out

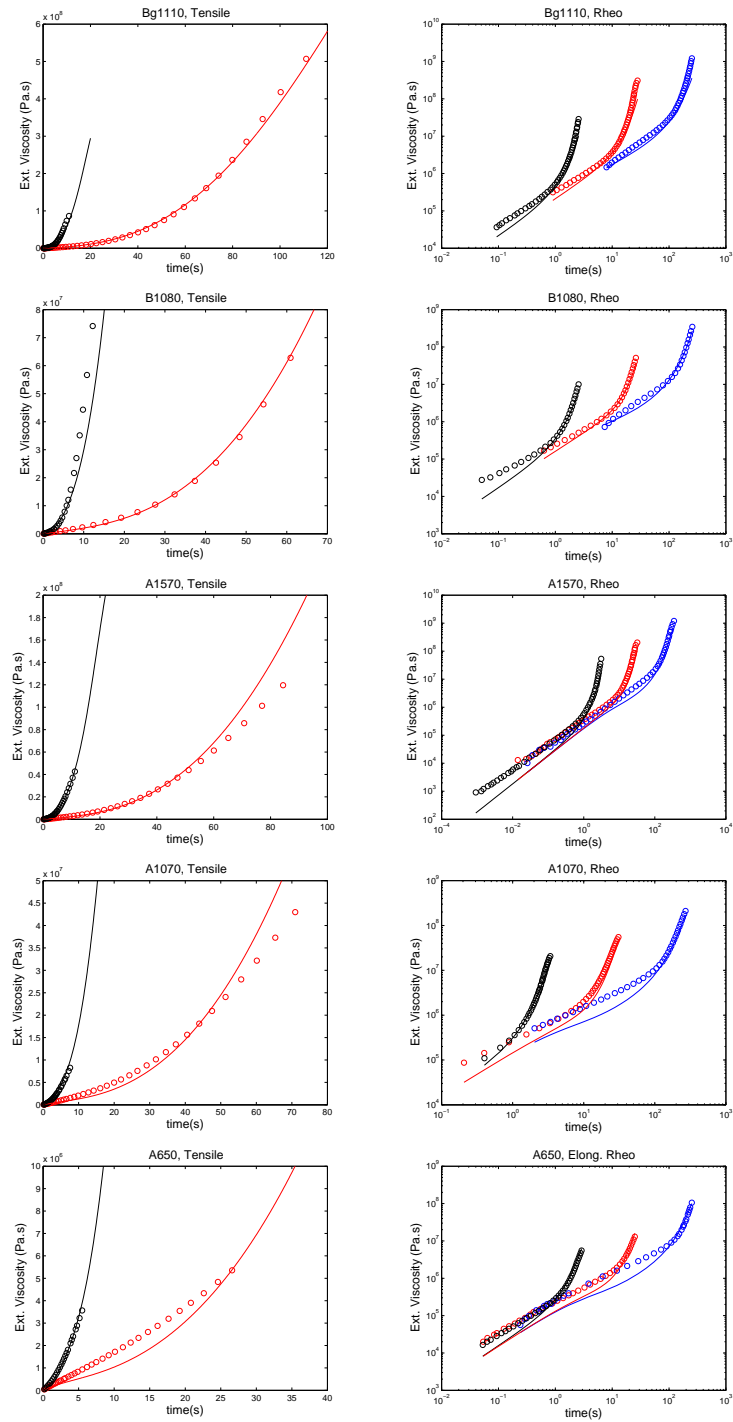


FIGURE 4.13 – Experimental curves (dots) obtained by fitting the PTT-2modes model with experimental results from tensile tests and extensional rheology.

4.6. PREDICTION OF THE ADHESIVE/COHESIVE DEBONDING TRANSITION OF PSAS129

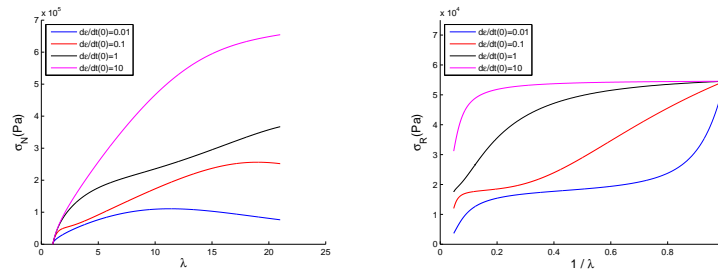


FIGURE 4.14 – Tensile curves using the 2-modes PTT model on B1080, plotted as $\sigma_N = f(\lambda)$ (left) and $\sigma_R = f(1/\lambda)$ (right) at four nominal strain rates.

on our materials at different strain rates are shown on the plot : White markers indicate cohesive debonding, black markers represent adhesive debonding and greyed for a mixed debonding. We observe that $C_{soft}/C_{LS} = 2.36$ separates very well the debonding modes, only one experiment being in the wrong area, Bg1110 at $0.01 s^{-1}$, where cohesive debonding is predicted but adhesive debonding is observed. All the other transitions for the materials are well predicted by this criterion, calculated from simulations using our 2-modes PTT model.

The 2-modes PTT model allowed us to simulate tensile tests at all equivalent rates as the probe-tack experiments and give us a new empirical criterion C_{soft}/C_{LS} to separate adhesive debonding from cohesive debonding. This criterion is equal to 2.36 for stainless steel.

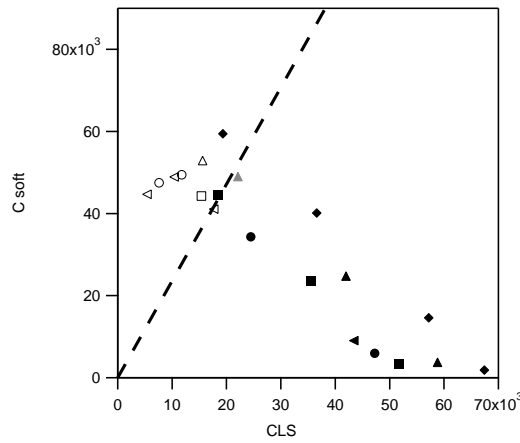


FIGURE 4.15 – C_{soft} vs C_{LS} for A1570, A1070, A650, Bg1110 and B1080. Adhesive debonding is represented by black markers, cohesive debonding by white markers and mixed debonding by grey marker.

4.7 Conclusion

In this chapter, we showed why a 2-modes PTT model was a good choice for describing the acrylic acid functionalized poly n-butyl acrylate polymers presented in Chapter 2 and we explicitly derived this model for a uniaxial deformation, being able to describe extensional rheology (constant Hencky strain rate) or tensile test (varying Hencky strain rate), the latter requiring the Hencky strain rate to vary over time. While a UCM model could have been used to describe our materials, the saturation brought by the PTT better catches the inflexion observed in extensional rheology in the non-linear part and the absence of exponential growth allows a simpler implementation of this model for simulations.

This model proved to fit well all our materials in uniaxial deformation at constant and varying $\dot{\epsilon}_H$. The two modes have been clearly linked to two dynamics of our materials previously observed by [citetPadding2011,Padding2012](#) : one describing the entanglement dynamics and the other one the stickers from acrylic acid groups.

Using the parameters obtained from the fits, we were able to simulate tensile tests over a wide range of strain rates not accessible by experiments. This allowed us to calculate C_{soft} and C_{LS} parameters, the former describing the softness of the material at a given strain rate, the latter being a high strain modulus of the material at a given strain rate. These parameters were calculated in all equivalent conditions as the probe-tack experiments presented in Chapter 2. A value of $C_{soft}/C_{LS} = 2.36$ clearly separates adhesive and cohesive failure observed in tack experiments. When the value is higher, the material is not elastic enough, leading to cohesive failure. When $C_{soft}/C_{LS} < 2.36$, the debonding is adhesive.

In this chapter, we showed by using our model that the debonding mode of homogeneous materials is directed by an equilibrium between softening and high strain at large scale. In the next two chapters of this thesis, we will make heterogeneous adhesives by introducing a gradient in viscoelastic properties along the thickness and show that good adhesive performances can be obtained while controlling the debonding mode.

Bibliographie

- Bird, R. B., Armstrong, R. C., and Hassager, O. (1977). *Dynamics of Polymeric Liquids*. John Wiley Sons, London.
- Briels, W. (2009). Transient forces in flowing soft matter. *Soft Matter*, 5(22) :4401–4411.
- Christensen, S. F. and Carlyleflint, S. (2000). A practical criterion for rheological modeling of the peeling of pressure sensitive adhesives. *The Journal of Adhesion*, 72(2) :177–207.
- Christensen, S. F. and McKinley, G. H. (1998). Rheological modelling of the peeling of pressure-sensitive adhesives and other elastomers. *International Journal of Adhesion and Adhesives*, 18(5) :333 – 343.
- Colby, R. H., Fetters, L. J., and Graessley, W. W. (1987). The melt viscosity-molecular weight relationship for linear polymers. *Macromolecules*, 20(9) :2226–2237.
- Deplace, F., Rabjohns, M. A., Yamaguchi, T., Foster, A. B., Carelli, C., Lei, C.-H., Ouzineb, K., Keddie, J. L., Lovell, P. A., and Creton, C. (2009). Deformation and adhesion of a periodic soft-soft nanocomposite designed with structured polymer colloid particles. *Soft Matter*, 5(7) :1440.
- Doi, M. and Edwards, S. F. (1978). Dynamics of concentrated polymer systems. part 2.-molecular motion under flow. *J. Chem. Soc., Faraday Trans. 2*, 74 :1802–1817.
- Du, J., Lindeman, D. D., and Yarusso, D. J. (2004). Modeling the peel performance of pressure-sensitive adhesives. *The Journal of Adhesion*, 80(7) :601–612.
- Gent, A. N. (1996). A new constitutive relation for rubber. *Rubber Chemistry and Technology*, 69(1) :59.
- Jensen, M. K., Bach, A., Hassager, O., and Skov, A. L. (2009a). Linear rheology of cross-linked polypropylene oxide as a pressure sensitive adhesive. *International Journal of Adhesion and Adhesives*, 29 :687–693.
- Jensen, M. K., Hassager, O., Rasmussen, H. K., Skov, A. L., Bach, A., and Koldbech, H. (2009b). Planar elongation of soft polymeric networks. *Rheologica Acta*, 49(1) :1–13.
- Jullian, N., Leonardi, F., Grassi, B., Peyrelasse, J., and Derail, C. (2010). Rheological characterization and molecular modeling of poly(n-butyl acrylate). *Applied Rheology*, 20(3) :33685–33696.
- Padding, J. T., Mohite, L., Auhl, D., Briels, W. J., and Bailly, C. (2011). Mesoscale modeling of the rheology of pressure sensitive adhesives through inclusion of transient forces. *Soft Matter*, 7 :5036.

Padding, J. T., Mohite, L. V., Auhl, D., Schweizer, T., Briels, W. J., and Bailly, C. (2012). Quantitative mesoscale modeling of the oscillatory and transient shear rheology and the extensional rheology of pressure sensitive adhesives. *Soft Matter*, 8 :7967–7981.

Phan-Thien, N. (1978). A nonlinear network viscoelastic model. *Journal of Rheology*, 22(3) :259.

Phan-Thien, N. and Tanner, R. I. (1977). A new constitutive equation derived from network theory. *Journal of Non-Newtonian Fluid Mechanics*, 2(4) :353–365.

Press, W. H., Teukolsky, S. A., Vetterling, W. T., and Flannery, B. P. (2007). *Numerical Recipes, The Art of Scientific Computing*. Cambridge University Press, New York.

Chapitre 5

Multi-layer adhesives

Contents

4.1	Introduction	111
4.2	Experimental section	111
4.3	Modeling uniaxial deformation of PSAs : choice of a convenient model	113
4.3.1	Choice of a convenient model for PSAs under uniaxial deformation	113
4.4	The PTT Model : Mathematical aspects	115
4.4.1	Application of the PTT model to the uniaxial flow	115
4.4.2	Asymptotic behavior	116
4.4.3	PTT model under constant $\dot{\epsilon}_H$ or varying $\dot{\epsilon}_H$	120
4.4.4	Influence of the parameters on the PTT Model	120
4.5	2-modes PTT model	123
4.5.1	Fitting strategy	124
4.5.2	Results and discussion	124
4.6	Prediction of the adhesive/cohesive debonding transition of PSAs	127
4.7	Conclusion	130

5.1 Introduction

As discussed in the general introduction, in order to obtain soft adhesives showing good PSA properties, one must strike a balance between a liquid-like behavior to easily create a molecular contact and dissipate energy upon debonding, and an elastic behavior to resist shear forces over long periods of time and obtain an interfacial debonding. This combination of apparently incompatible properties should be especially fine tuned when the adhesive is applied on rough surfaces and low energy surfaces. As seen in chapter 4, the deformation process during debonding is complex and does not deform the PSA in a homogeneous way (cavity nucleation at the interface, growth in the bulk and eventual debonding from the interface). It is therefore reasonable to think that a homogeneous layer of adhesive is not the best solution to reach the combination of macroscopic properties that are needed. There are several ways to introduce heterogeneities in an adhesive. It can be done at the level of the polymer structure (block copolymers, (Brown et al., 2002)) at the particle structure (films made from latex particles, (Deplace et al., 2009a; Pinprayoon et al., 2011)) and at the layer structure (multilayer structures, (Carelli et al., 2007)). In chapters 2 to 4 we have explored the effect of molecular structure of the polymer and used a method to make adhesive films which involves the coalescence of particles. In these later chapters we explore a different strategy, which is to create a gradient in viscoelastic properties through the thickness of the adhesives. When the PSA is detached from low energy surfaces such as polyethylene, silicone or release surfaces, the target is usually to increase the adhesion energy, i.e. the dissipation of energy during the process of debonding, with the constraint that the adhesive should still debond cleanly from the surface. At the more microscopic and material level, we target a more dissipative behavior near the adhesive/adherend interface to influence the debonding mechanisms and the contact angle (Nase et al., 2010) while keeping a more elastic behavior in the bulk of the adhesive. When the PSA is debonded from high energy surfaces such as glass or steel, introducing a less dissipative behavior at the interface and a more viscous in the bulk should combine higher deformability in the bulk with a higher contact angle at the interface and less stress relaxation at the foot of the fibril and hence an easier detachment of the fibrils at very high strains (Glassmaker et al., 2008). Preliminary studies on bi-layer adhesives have already been carried out and show interesting adhesive properties relative to their homogeneous counterparts (Carelli et al., 2007). However the system used by Carelli *et al.* was close to industrially used latexes and it was difficult to extract a systematic trend. In the current study we benefit from our model PSA materials with a well controlled and characterized molecular structure to investigate the effect of this multi-layer structure on the debonding mechanisms and level of adherence of the PSA. We focused here on this strategy by making a systematic study of the adhesive properties of bi-layer adhesives on high and low adhesion surfaces.

5.2 Making multi-layer adhesives

Materials used to make the multi-layer systems were provided by DOW Chemical Company and were presented in details in Chapter 2. We focused on the first generation of adhesives, e.g. A1570, A1070 and A650 (see 5.1). We have shown in Chapter 2 that these materials show a wide range of viscoelastic properties, with a viscous component increasing with decreasing M_w . We remind that these materials are fully soluble in polar organic solvents and therefore uncross-linked. As a result their rheological and mechanical properties in general are highly dependent on the test frequency.

Polymer	CTA (%)	Mn (kg/mol)	Mw (kg/mol)	PDI (-)	$d_{particles}$ (nm)	Gel content (%)
A1570	-	611	1572	2.57	400	-
A1070	0.05	466	1065	2.28	403	-
A650	0.1	298	651	2.18	400	-

TABLE 5.1 – Molecular weights, polydispersity index (PDI), diameter of latex particles and gel content for the A series.

Thin films prepared from latex particles of individual polymers described in Table 5.1 were prepared with the collaboration of Isabelle Uhl and Natacha Cisowski from DOW Chemical Company. Films were prepared at high speed, blowing hot air during two minutes on a 20cm x 10cm siliconized substrate offering low adhesion with the PSA. In order to wet the low surface energy siliconized substrate, the viscosity of the latex solution and its wetting properties were adjusted. ACRY SOL RM-2020 thickener (0.2 wt%) and OT-75 wetting agent (0.3 wt%) were added and the pH of the solution was adjusted to 8.5. Films were obtained with a final thickness of 20-25 μm . After drying, the top of the films were protected with another siliconized paper showing a lower adhesion than the one on the bottom side.

Once these films were obtained, small strips adapted to the two tests were cut from the sheets : 7cm x 2cm for tack tests and 8cm x 3cm for shear tests. The technique used to make multi-layers is summarized in Fig 5.1. After removing one of the siliconized papers, a first strip was put on a rigid substrate, glass treated with plasma in the case of probe-tack tests or treated PET films in the case of shear experiments. In both cases, the surface pre-treatment was made to enhance adhesion between the rigid substrate and the first layer. The second siliconized paper was then removed, leading to an adhesive layer deposited on the substrate. Supplementary layers were just added on top of the first, one by one, by removing the first siliconized paper and carefully sticking it. In all the systems, four layers were added to reach a final thickness between 80 and 100 μm . In order to ensure a good interpenetration of the polymer chains between the layers and hence a good adhesion, films were annealed at 80°C under load for 10 hours.

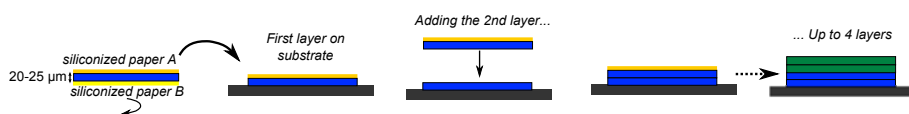


FIGURE 5.1 – Making multi-layer materials

In the following, multi-layer materials will be referred to by using a nomenclature indicating the number of layers of each material. For example, 2A1570-2A1070 indicates two layers of A1570 under two layers of A1070. Thus, A1070 will be in contact with the probe and A1570 with the rigid substrate (PET or glass).

In order to get a reference adhesive without the influence of the multi-layered structure, we prepared blend materials by mixing latexes in the same proportions and using the same formulation. Films of 20-25 μm were prepared exactly the same way as the 20-25 μm films of our other materials. Using the same protocol, four layers were put on top of each other to make the blend adhesive.

5.3 Experimental Techniques

5.3.1 Probe-tack Test

The Probe-tack apparatus was similar to the one presented in Chapter 2, section ??, ??. The tests in this chapter were carried at room temperature with the following parameters : approach velocity = 30 $\mu\text{m}/\text{s}$; contact force = 70 N; contact time = 10 s; debonding velocity = 10 or 100 $\mu\text{m}/\text{s}$. In order to vary the surface, a polished stainless steel probe and a polyethylene probe were used.

5.3.2 Shear test

Resistance to shear was measured with a set-up using the standardized *PTSC-107 Shear Adhesion of Pressure Sensitive Tape* specifications. Adhesives were carefully pressured on an aluminium surface. Contact area was 25mm x 25mm and a load of 1kg was fixed at the bottom of the film (see Fig. 5.2). A camera was installed and configured with a movement detector in order to record the time when the adhesive failed.

5.4 Results and Discussions

5.4.1 Multi-layer materials on low adhesion surface

On surfaces forming weak interactions with the acrylic adhesive, such as HDPE, the main issue to obtain optimized adhesive properties is to have a

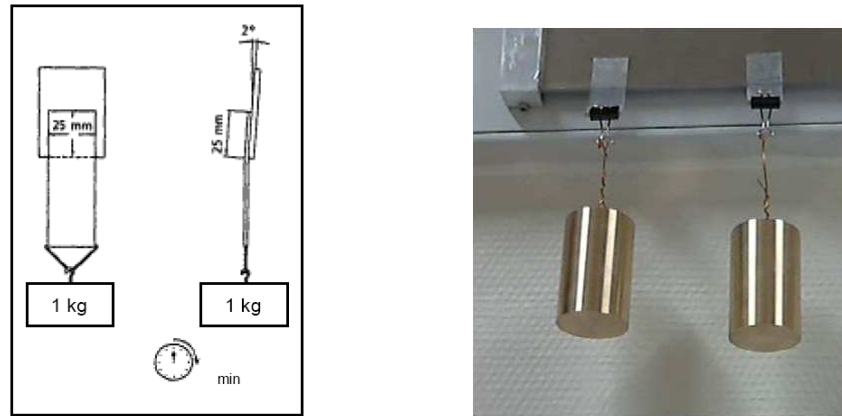


FIGURE 5.2 – Figure of the shear test (left) and picture of the set-up developed in the lab (right)

good level of energy dissipation during the debonding process without reducing cross-linking to the point that the PSA is no longer resistant to shear. A typical cross-linked PSA, optimized to stick well on glass or steel, does not dissipate enough energy on HDPE, leading to interfacial crack propagation and low values of W_{adh} . On the other hand one would expect, a fully uncross-linked material to show better dissipation.

A first approach to design this kind of multi-layer material was to make bi-layers by coupling a $50 \mu m$ more viscous layer of A650 (2 layers of $25 \mu m$) near the interface with a more elastic backing (A1570, 2 layers of $25 \mu m$). This material was compared with a homogeneous material of the pure components made in the same way, e.g. by four layers of $25 \mu m$ of A1570 (4A1570) and four layers of A650 (4A650).

Representative probe tack stress-strain curves for all three materials at $V_{deb} = 10 \mu m.s^{-1}$ are shown on Fig 5.3-a. Even on polyethylene, the 4A650 adhesive shows a liquid-like debonding, confirmed by the presence of a stress-strain curve with a double-plateau and an eventual cohesive failure. At the same debonding velocity, 4A1570 shows a curve with only a characteristic peak due to cavitation and then a fast drop of the stress to zero. This type of curve is characteristic of an interfacial crack propagation without formation of fibrils as discussed in section 1.4.2, p.31 (Deplace et al., 2009b). The bi-layer system does not really show an intermediate behavior as expected, but instead one very similar to 4A650. This composite material acts as if only the viscous layer was deformed. To confirm that, we represented the probe test curves of the 4A650 and of the the bi-layer with the hypothesis that the thickness of the bi-layer was $50 \mu m$, in other words we normalize the displacement of the probe for the bi-layer by the thickness of the soft layer only. As shown on Fig 5.3-b, the two curves are now nearly identical, the small difference between the two curves being due to

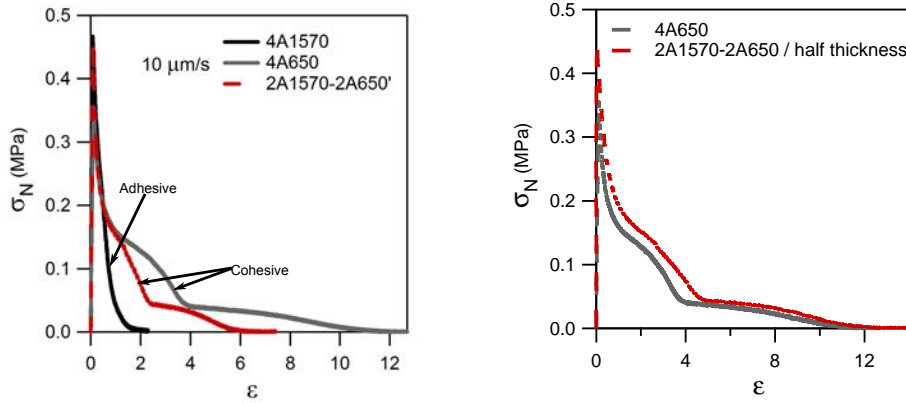


FIGURE 5.3 – Left (a) : Probe-tack curves of A1570, the more elastic film, A650 the more viscous one and a bi-layer with a viscous layer and an elastic backing. The probe used is polyethylene, $V_{deb} = 10\mu m.s^{-1}$. Right (b) : Probe-tack curves for A650 and for the bi-layer, considering an initial thickness of $40\mu m$ instead of $80\mu m$. As a consequence, the strain is doubled.

the small amount of deformation of the A1570 backing layer. This result can be explained by the relatively high difference in viscoelasticity between the two layers : if the stiffness of the two layers is too different, only the more viscous layer will be deformed.

In order to obtain a better synergy between the two materials, A650 was replaced by A1070. Results from probe tests at $V_{deb} = 10\mu m.s^{-1}$ are shown on Fig 5.4 : while the 4A1070 assembly shows a cohesive failure upon debonding, the bi-layer 2A1570-2A1070 still debonds with formation of fibrils confirmed by the presence of a plateau, but detaches now without residues from the surface. The contribution of the elastic backing layer during the extension of the fibrils is also shown by the higher plateau stress obtained compared to 4A1070. By making a bi-layer system, we are thus able to obtain high dissipation with an adhesive failure on a surface interacting weakly with the adhesive.

The same system was tested at a higher V_{deb} of $100\mu m/s$, see Fig. 5.5. In that case, while the synergy is maintained and adhesive failure is obtained despite the presence of A1070 at the interface, the adhesion energy is lower and only a limited improvement is obtained when compared with the homogeneous 4A1570. This can be explained by the high sensitivity of our materials to the strain rate. At $100\mu m/s$, the fine balance that we found at $10\mu m/s$ between elasticity of the backing and dissipation of the interfacial layer is not reached anymore. In this case, the layer assembly is too elastic and cannot dissipate enough energy during the debonding.

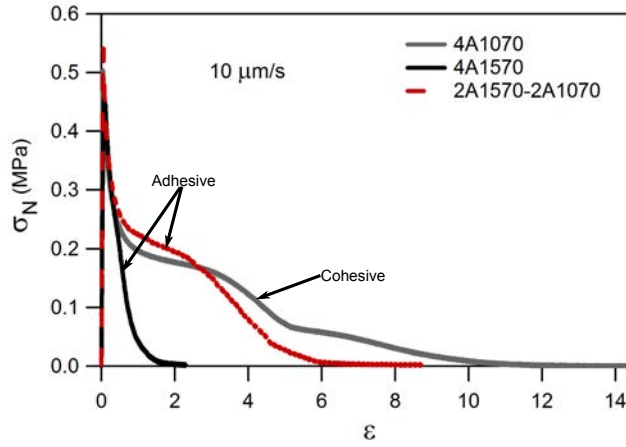


FIGURE 5.4 – Stress-strain curves for 2A1570-2A1070, 4A1570 and 4A1070. The probe used is polyethylene, $V_{deb} = 10\mu m.s^{-1}$.

5.4.2 Multi-layer materials on high adhesion surface

On surfaces with stronger interactions, such as stainless steel or glass, the goal is to maintain an adhesive failure, while maximizing the adhesion energy. In this case a more elastic behavior is needed at the interface with the substrate. Uncross-linked materials, while showing high dissipation during debonding, fail cohesively : to obtain adhesive failure, one has to reach a sufficiently high level of cross-linking, losing therefore in deformability of the layer and therefore reducing the adhesion energy. In order to avoid this cohesive debonding, an elastic layer has to be put on top of a viscous backing.

Bi-layers composed of a backing of A1070 (2 layers of $25\mu m$) and an interfacial layer of A1570 (2 layers of $25\mu m$) were tested. Results for $V_{deb} = 10\mu m/s$ are presented on Fig 5.6 left. The pure 4A1070 shows a liquid-like behavior upon debonding at that velocity with a cohesive failure while 4A1570 shows high dissipation and adhesive failure, close to an optimized PSA. However the bi-layer system increases adhesion energy by 36.8% when compared to 4A1570 and still shows an adhesive failure (see Table 5.2).

At $V_{deb} = 100\mu m/s$, (Fig. 5.6 right), 4A1070 shows now an important increase in adhesion energy but failure remains cohesive. The behavior observed for the bi-layer is still very interesting : the adhesive failure is maintained and an increase of 36% in the adhesion energy is observed relative to the A1570.

The similarity between the debonding mechanisms of the bi-layer and the 4A1570 system is due to the presence of the same material at the interface. The failure mode is controlled by the material at the interface, while σ_{fib} , the stress at the plateau and the maximal elongation ϵ_{max} are influenced by both layers

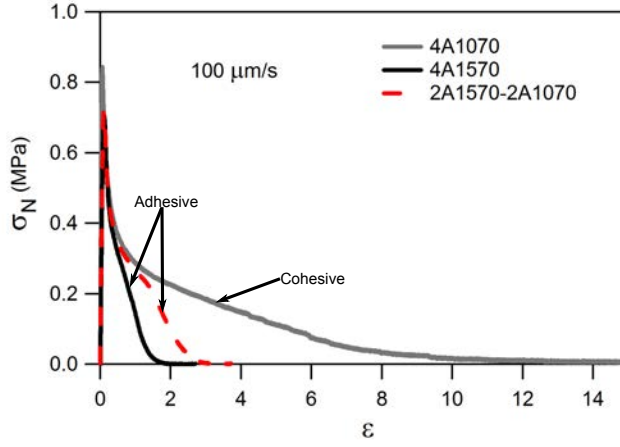


FIGURE 5.5 – Stress-strain curves for 2A1570-2A1070, 4A1570 and 4A1070. The probe used is polyethylene, $V_{deb} = 100\mu m.s^{-1}$.

$V_{deb}(\mu m/s)$	$W_{adh}(J/m^2)$		$\sigma_{fib}(MPa)$		$\epsilon_{max}(MPa)$	
	10	100	10	100	10	100
4A1570	117.8 (A)	86.8 (A)	0.242	0.355	14.9	4.89
2A1070-2A1570	161.2 (A)	118.2 (A)	0.225	0.31	8.75	9.43
4A1070	69.2 (C)	222.7 (C)	0.213	0.262	10.3	36.3

TABLE 5.2 – Adhesion energy, σ_{fib} and ϵ_{max} for homogeneous systems and bi-layer system at two debonding rates. Failure modes are precised : (A) : Adhesive Failure, (C) : Cohesive Failure

(see Table 5.2) For the bi-layer material :

$$\sigma_{fib} \approx \frac{1}{2} (\sigma_{fib}^{A1570} + \sigma_{fib}^{A1070}) \quad (5.1)$$

The value of ϵ_{max} is difficult to predict quantitatively from viscoelastic properties of the materials, as this parameter depends on the details of the large strain behavior of the two materials in a subtle way. As a consequence, no clear scaling has been found for this parameter.

We checked these interesting effects of the adhesive architecture with a control experiment. We inverted the two layers, putting this time the A1070 layer at the interface and A1570 as a backing, as was done earlier in this chapter for the adhesive debonded from polyethylene. In that case, a cohesive debonding is obtained (because of the A1070 layer at the interface with the steel probe), while σ_{fib} remains nearly the same but the maximal elongation is increased. When compared to 4A1070, the adhesion energy increased by 21.3%.

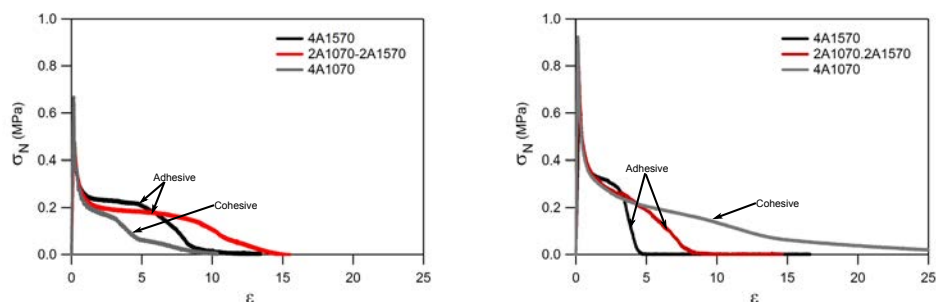


FIGURE 5.6 – Stress-strain curves for 2A1070-2A1570, 4A1570 and 4A1070. The probe used is stainless steel. Left : $V_{deb} = 10\mu m.s^{-1}$, right : $V_{deb} = 100\mu m.s^{-1}$

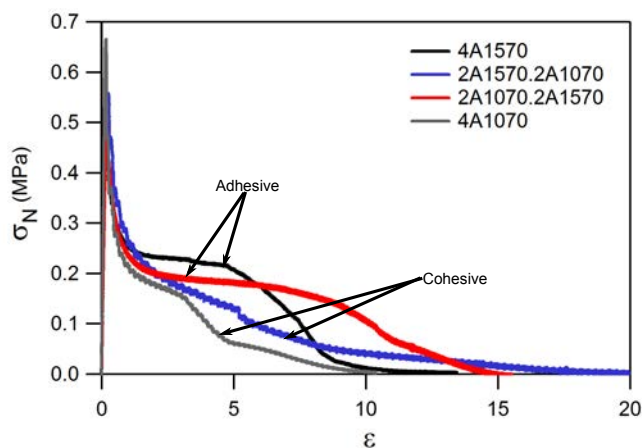


FIGURE 5.7 – Making multi-layer materials

5.4.3 Comparison with blend systems

Since the results obtained show a synergy between the two polymers used, one can object that it could be due to the effect of blending these two polymers in the material and not to its layered structure. To discuss this point, we prepared a system composed of four layers of blended A1570 and A1070 (50wt% of each of the latex particles). We compared the bi-layer with this system on PE.

Results are shown for $V_{deb} = 10\mu m.s^{-1}$ and $V_{deb} = 100\mu m.s^{-1}$ on Fig. 5.8. At both strain rates, blends show a more liquid-like behavior leading to higher dissipation but cohesive failure. Surprisingly, the presence of A1570 in the blend has little influence on the elasticity, as the debonding is still similar to a viscous system, as 4A1070 shows. This result shows unambiguously that the composition alone cannot be a good predictor of the adhesive properties. For heterogeneous systems the spatial distribution of the particles is undoubtedly

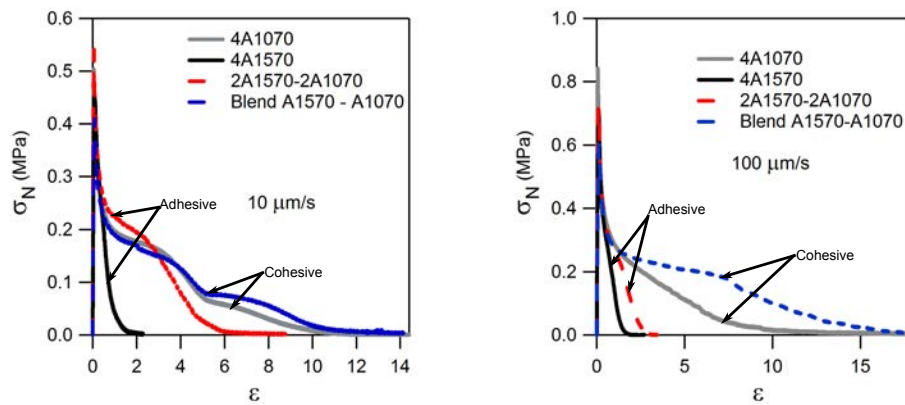


FIGURE 5.8 – Stress-strain curves for 2A1570-2A1070, 4 layers of blend, 4A1570 and 4A1070. The probe used is polyethylene. Left : $V_{deb} = 10\mu m s^{-1}$, right : $V_{deb} = 100\mu m s^{-1}$

important and in the case of blends the softer particles seem to dominate the behavior.

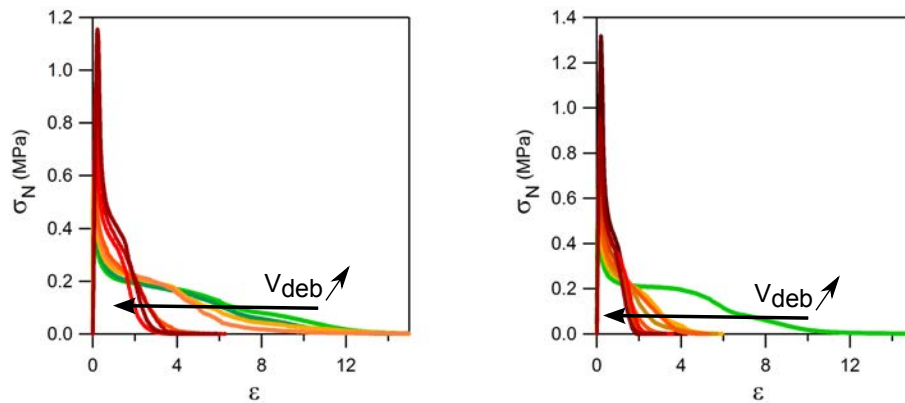


FIGURE 5.9 – Stress-strain curves for 4 layers of blend (left) and 2A1570-2A1070 (right) on a wide range of debonding velocities : 5 ; 10 ; 31.6 ; 56.2 ; 100 ; 177.8 ; 316.2 ; 562.3 ; 1000 $\mu m s^{-1}$. The probe used is polyethylene.

Yet the materials we used are very strain rate dependent. In order to better understand the differences between the two systems, we studied these materials over a range of debonding velocities. The objective was to observe the effect of the viscoelastic properties of the materials composing the layers on the adhesive behavior of the multi-layer adhesive. Nine different probe debonding velocities were used, ranging between 10 and 1000 $\mu m .s^{-1}$, see Fig. 5.9. The debonding

mechanisms were determined in each case : bi-layer materials change from cohesive debonding to adhesive debonding when V_{deb} becomes larger than $5\mu m.s^{-1}$ while blends change for a value $V_{deb} > 60\mu m.s^{-1}$. We can conclude that the layered structure with an elastic homogeneous backing allows an adhesive debonding at the interface for a lower probe velocity than the homogeneous system. Interestingly for both cases there is a clear transition in the layer deformation at failure between adhesive and cohesive debonding. This is due to the absence of strain hardening so that if the deformation occurs in the bulk it is difficult to have adhesive failure.

5.4.4 Effect of the thickness of the layers

The systems discussed above were only composed of two layers of each material. To better understand the synergy between both layers, we varied the composition of the system, always keeping four total layers, but using three layers of one material and one of the other. Following the nomenclature used until now, 3A1570-1A1070 describes a system with three layers of A1570 and one layer of A1070 on top, A1070 being the material in contact with the probe.

We did these experiments using both systems tested on polyethylene probe, e.g A1570-A650 and A1570-A1070 at $100\mu m.s^{-1}$, see Fig. 5.10. Interestingly, we see only a very small difference between 4A650 and 1A1570-3A650, indicating that in these conditions, one layer of A1570 hardly matters. The $75\mu m$ thick layer of A650 seems to deform in the same way in both cases. A thicker layer of the more elastic material seems to slightly increase σ_{fib} , see 3A1570-1A650. But as with the 2A1570-2A650 system discussed above, no synergy is observed between both materials. The results are more complex when a clear synergy occurs between the layers, as for A1570 and A1070 on the PE probe. Adding a layer of A1570 from 2A1570-2A1070 to 3A1570-1A1070 interestingly increases ϵ_{max} while keeping the same global behavior. This may be explained by stronger fibrils that break later and suggests that the additional dissipation to prevent interfacial crack propagation is only required very close to the probe surface. The adhesive debonding is logically maintained. On the other hand, adding more soft material does not help : 1A1570-3A1070 follows the same initial behavior as 2A1570-2A1070, but fibrils fail to debond adhesively, and a second plateau is observed.

The same study on the effect of layer thickness was carried out on the stainless steel probe too, using the system 2A1070-2A1570. Interestingly we observe the same behavior as the 2A1570-2A1070 on polyethylene, cf Fig. 5.11 : the thicker the elastic layer is, the higher ϵ_{max} . On steel, adhesive debonding is obtained in each case, so if we aim at a maximal energy while keeping adhesive debonding, the 1A1070-3A1570 seems the most promising. More generally, the thickness of the layers seems to determine the maximal elongation of the system, with a smaller influence on the debonding mechanism than the nature of the material itself.

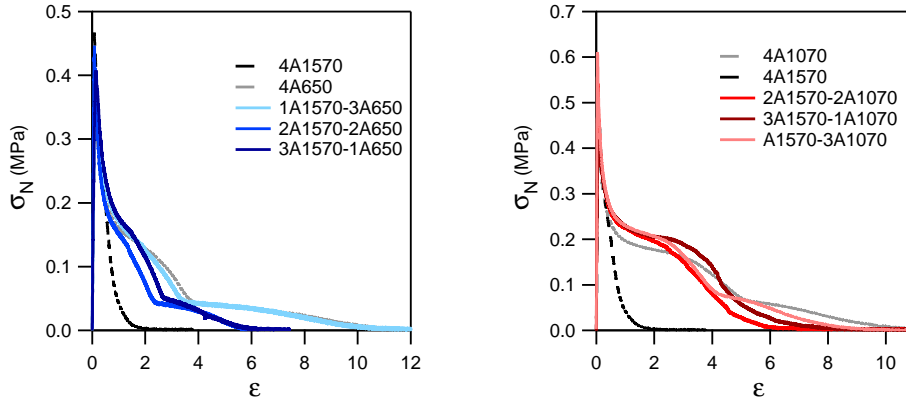


FIGURE 5.10 – Stress-strain curves for x A1570- y A650 (left) and x A1570- y 1070 (right). The probe used is polyethylene, $V_{deb} = 100 \mu m s^{-1}$. TO ADD : Cohesive / Adhesive mode

5.4.5 Shear properties

To confirm the good interpenetration of the layers and the efficiency of our bi-layer systems, we realized shear experiments using 4A650, 4A1070, 4A1570, 2A1570-2A1070 and 2A1070-2A1570 on a PET backing. The substrate was aluminium. Results obtained from this experiment, e.g the time before the adhesive fails, are reported in Table 5.3. All failures were cohesive. This experiment shows very well the difference between 4A650, 4A1070 and 4A1570, as their resistance in time goes from 11min for 4A650 to more than 7200min for 4A1570, when we decided to stop the experiment. Bi-layers composed by two layers of A1570 and A1070 show an intermediate behavior between 4A1070 and 4A1570, showing that adding an elastic backing to a more viscous layer indeed improves the overall shear resistance of the system : a synergy is well present between A1570 and A1070 in this geometry also. We find a difference between 2A1570-2A1070 (A1070 on aluminium) and 2A1070-2A1570 (A1570 on aluminium) that cannot be simply explained by the experimental error, as the difference seems higher than the standard deviation. Supplementary experiments could not be realized because of the lack of material, and we cannot at this point explain the difference between these two systems.

	4A650	4A1070	4A1570	2A1570-2A1070	2A1070-2A1570
Resistance (min)	11.33	276.67	7200.00*	1015.67	620.00
Standard Dev	306	45.09	-	252.24	141.42

TABLE 5.3 – Results of shear experiments. For 4A1570, Experiment was stopped after no failure was observed after 7200 min.

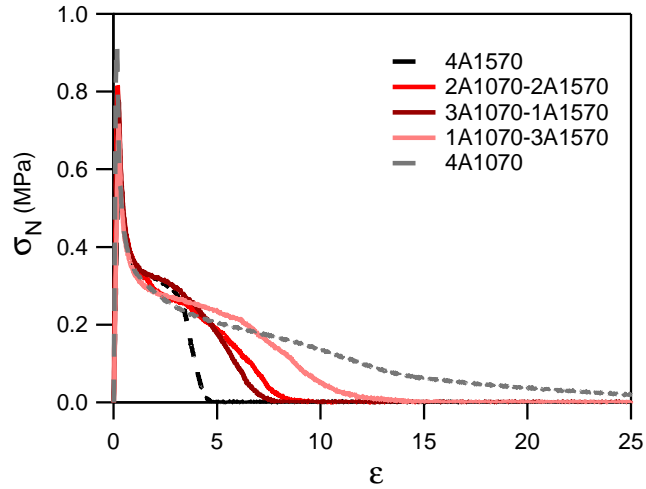


FIGURE 5.11 – Stress-strain curves for 2A1070-2A1570, 3A1070-1A1570, 1A1070-3A1570, 4A1570 and 4A1070. The probe used is stainless steel, $V_{deb} = 100\mu\text{ms}^{-1}$.

5.5 Conclusion

In this chapter we have explored in a systematic way how a layering of the adhesive can influence its debonding mechanisms (adhesive or cohesive) and modify its adhesion energy. The effect of the layering demonstrates that even the debonding mechanism of a very soft adhesive such as a PSA is always very heterogeneous with most of the dissipation occurring near the interface. Hence an optimization of the composition and therefore of the viscoelastic properties of the adhesive along its thickness seems a viable option. Nevertheless the optimization of the composition to obtain a real improvement over homogeneous layers is far from trivial.

Using model materials with varying molecular weights, we have been able to explore two ways of improvement by layering. On weakly adhering surfaces such as PE, the main factor limiting the performance is the low adhesion energy due to insufficient viscoelastic dissipation near the interface. Therefore it makes sense to increase the dissipation of the layer in direct contact with the adherend, while keeping a material of higher molecular weight further away from the interface. This strategy is interesting since it permits to shift the strain rate level at which the debonding changes from cohesive to adhesive to lower values. The case of adhesion on strongly adhering surfaces such as steel and glass leads to very interesting results. In this case an increase in deformability of the layer is desired without cohesive debonding. It is therefore useful to intro-

duce a lower molecular weight layer as a backing. The higher molecular weight layer remains in contact with the adherend and the adhesive debonding is maintained. However the more viscous backing layer increases the deformability and in our case increases the adhesion energy by 20-30% which is far from negligible.

The influence of the thickness of the layers was studied and showed that, while the thickness has a clear influence on the maximal elongation, the consequence on the debonding mode was quite limited. This can lead to interesting applications, as the control of the thickness of a bi-layer system can control the deformation of the system without impacting too much the debonding mechanism.

Although we performed these experiments with model materials which are uncross-linked and hence different relative to most commercial PSA, we feel that the concept should work also for weakly cross-linked systems, i.e. on PE and similar surfaces, a softer less cross-linked layer in direct contact with the surface is needed, while on steel or glass a softer layer can be used as a backing.

Bibliographie

- Brown, K., Hooker, J. C., and Creton, C. (2002). Micromechanisms of Tack of Soft Adhesives Based on Styrenic Block Copolymers. *Macromol. Mater. Eng.*, 287 :163–179.
- Carelli, C., Deplacé, F., Boissonnet, L., and Creton, C. (2007). Effect of a gradient in viscoelastic properties on the debonding mechanisms of soft adhesives. *The Journal of Adhesion*, 83(5) :491.
- Deplacé, F., Carelli, C., Langenfeld, A., Rabjohns, M. A., Foster, A. B., Lovell, P. A., and Creton, C. (2009a). Controlled sparse and percolating cross-linking in waterborne soft adhesives. *ACS Appl. Mater. Interfaces*, 1(9) :2021–2029.
- Deplacé, F., Carelli, C., Mariot, S., Retsos, H., Chateauminois, A., Ouzineb, K., and Creton, C. (2009b). Fine tuning the adhesive properties of a soft nanostructured adhesive with rheological measurements. *The Journal of Adhesion*, 85(1) :18–54.
- Glassmaker, N., Hui, C., Yamaguchi, T., and Creton, C. (2008). Detachment of stretched viscoelastic fibrils. *The European Physical Journal E*, 25(3) :253–266.
- Nase, J., Creton, C., Ramos, O., Sonnenberg, L., Yamaguchi, T., and Lindner, A. (2010). Measurement of the receding contact angle at the interface between a viscoelastic material and a rigid surface. *Soft Matter*, 6 :2685–2691.
- Pinprayoon, O., Groves, R., Lovell, P. A., Tungchaiwattana, S., and Saunders, B. R. (2011). Polymer films prepared using ionically crosslinked soft core-shell nanoparticles : a new class of nanostructured ionomers. *Soft Matter*, 7(1) :247–257.

Chapitre 6

PSAs with a continuous gradient

Contents

5.1	Introduction	135
5.2	Making multi-layer adhesives	136
5.3	Experimental Techniques	137
5.3.1	Probe-tack Test	137
5.3.2	Shear test	137
5.4	Results and Discussions	137
5.4.1	Multi-layer materials on low adhesion surface	137
5.4.2	Multi-layer materials on high adhesion surface	140
5.4.3	Comparison with blend systems	142
5.4.4	Effect of the thickness of the layers	144
5.4.5	Shear properties	145
5.5	Conclusion	146

6.1 Introduction

During the previous chapters of this thesis, we have studied well-defined acrylic model PSA and showed that, by making bi-layer systems, we could tune to a certain extent the failure mode (at the interface or in the bulk) while increasing the dissipation and the resistance to shear. This fine tuning depends on the substrate on which the PSA should be used. To go further in this direction, one can think of a more efficient way compared to multi-layers to introduce a gradient of viscoelastic properties through the thickness of the adhesive. In particular, it would be interesting to tune the viscoelastic properties in a continuous way by having a continuously varying crosslink density as a function of position along the thickness.

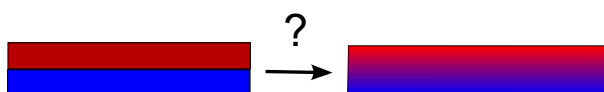


FIGURE 6.1 – Bi-layer system presented in Chapter 5 on the left compared to one with a continuous gradient discussed in this chapter

In this chapter, we will present a method to obtain films with a continuous gradient in viscoelastic properties along the thickness of the adhesive. We synthesized acrylic adhesive films similar in chemical structure to those used in the previous chapter of this thesis, but synthesized in solution and not in emulsion. These materials will then be cross-linked by a molecule that can be added post-synthesis and will react during the drying of the adhesive film. Using this method, we will produce layers with a gradient in cross-links density.

6.2 Preparation of Solvent-based model acrylic polymers

We synthesized a solvent-based model acrylic polymer : contrary to water-based polymers made by emulsion polymerization used previously in the thesis, the solvent-based polymers is dissolved in an organic solvent and not dispersed in water. This modifies the average molecular weight of the starting polymer, which is typically lower than what can be obtained in emulsion where the polymerization process occurs without solvent. Therefore PSA made by that method are invariably cross-linked after the film is cast on the substrate.

6.2.1 Synthesis

System used

We targeted solvent-based polymers with a similar monomer composition than those presented in the previous chapters, e.g. 98.1 wt% in butyl acrylate (BA) and 1.90% in acrylic acid (AA), equivalent to a molar composition of 96.6%

in BA and 3.4% in AA, with the objective to obtain a polymer with long chains able to be cross-linked after synthesis in a controlled way. In order to obtain random copolymers, we carried out a semi-continuous thermally activated free radical polymerization in solution, based on the protocol described by Tobing and Klein (2001). Poly (Butyl Acrylate - co - acrylic acid) was obtained, and will be referred to as Poly(BA-co-AA) thereafter. The thermal activator used for this synthesis was azobisisobutyronitrile (AIBN). For the cross-linking reaction, we selected Aluminium Acetyl Acetate, which can react with acrylic acid functions and act as a cross-linker. This cross-linker does not react if Acetyl Acetone is present (see below for details of the mechanism). Thus, elimination of the retarding agent will activate a fast cross-linking reaction.

Chemicals

Reagents and solvents used here are commercial products purchased from Aldrich or SDS. We used butyl acrylate (BA, CAS 141-32-2) acrylic acid (AA, CAS 79-10-7) as monomers, Aluminium Acetyl Acetate (AlAcAc, CAS 13963-57-0) as a cross-linker and Acetyl Acetone (AcAc) as a retarding agent. Hexane (CAS 110-54-3) was used as the main solvent and Toluene (CAS 108-88-3) as a co-solvent. See Table 6.1 for more information on the chemicals used.

All the monomers were passed through a column of basic activated alumina, to remove the inhibitor. Solvents were used with no further purification.

Synthesis protocol of the uncross-linked polymer

100g of Hexane were filled in a three-neck round bottom flask. On top of the flask were put a mechanical mixer, a cooling column and a dropping funnel were added. To avoid side reactions due to the presence of oxygen, the hexane was mixed in contact with nitrogen during 45 min. Also, a chloride calcium barrier was put on top of the cooling column to avoid any introduction of oxygen from the air in the flask.

A monomer solution (named solution A) was prepared by mixing 55.7g of BA, 1.08g of AA and 0.136g of AIBN. The solution was mixed during 20 min to allow AIBN dissolution and then mixed in contact with nitrogen during 30 min. Besides, a solution of 7g of toluene and 0.062g of AIBN (solution B) was mixed and put in contact with nitrogen for 15 min.

Hexane was then heated to reflux (boiling temperature of Hexane : 68.73° C) by using a thermostatically-controlled oil bath. Once the reflux was stable, solution A was introduced in the dropping funnel (no contact with air). Then, the dropping funnel was set-up to ensure a drop by drop flow for a total introduction time of 1 hour (average introduction time : 0.95g/min). The mix of solvents and monomers was left to react for three hours. Finally, solution B, playing the role of a catalyst ensuring a maximal conversion, was introduced in the dropping funnel with the same precautions as for the solution A and was introduced in the solution dropwise for 30 min. The solution was then left to react under stirring during 1 hour before the reaction was stopped by cooling

6.2. PREPARATION OF SOLVENT-BASED MODEL ACRYLIC POLYMERS 153

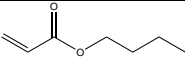
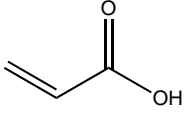
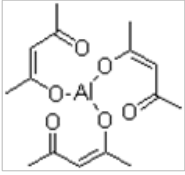
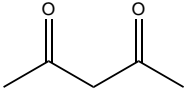
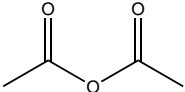
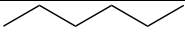
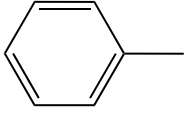
Notation	Chemical name	Semi-developed formula	Molar mass <i>g.mol</i> ⁻¹	Purity	Origin
BA	Butyl Acrylate		128.17	≥ 99%	Aldrich
AA	Acrylic Acid		72.06	99%	Aldrich
AlAcAc	Aluminium Acetylacetonate		324.31	99.9%	Aldrich
AcAc	Acetylacetone		100.12	99%	Aldrich
Acetyl acetate	Acetylacetate		102.09	99%	Aldrich
Hexane	Hexane		86.18	99%	Aldrich or SDS
Toluene	Toluene		92.14	99%	Aldrich or SDS

TABLE 6.1 – Chemical components used for the synthesis and cross-linking of Poly(BA-co-AA)

the solution in an ice bath and adding 25g of toluene. The solution was then stocked in a freezer.

This synthesis was realized five times in the same operating conditions to ensure reproducibility of the protocol and to obtain enough material for the planned studies.

Synthesis Reference	Mn (kg/mol)	Mw (kg/mol)	PDI
1	232.3	624.6	2.689
2	237.44	622.2	2.621
3	277.0	590.7	2.133
4	283.7	640.2	2.257
5	288.0	570.2	1.980
Average	263.7	609.6	2.336
Std Deviation	26.7	28.4	0.308

TABLE 6.2 – GPC results for different synthesis following the same protocol of Poly(BA-co-AA)

6.2.2 Chemical Characterization

The solutions obtained were characterized by GPC in order to determine the average molecular weight and the polydispersity of the polymer obtained. The polymer was dried and dissolved in THF. This characterization was done on the five syntheses and led to the results given in the Table 6.2.

We observe good reproducibility between the five different syntheses, with a PDI >2 as it can be expected for a conventional free radical solution polymerization. The molecular weight is high and given the final viscosity of the solution obtained, we cannot expect to reach higher Mw by using a conventional radical solution polymerization. The PDI is higher for the syntheses 1 and 2, as the mixer was better configured for the following reactions. As a consequence, we decided to use only polymers from the syntheses 3, 4 and 5 for the studies described here.

Fig. 6.2 shows the results of GPC on one of our synthesis. During a GPC test, the bigger molecules go out of the column first, so for a lower retention volume. The refractive index is proportional to the quantity of molecules, giving the population of molecular weights in the solution. These results indicate the presence of a classical polydisperse solution with a supplementary small population of larger molecules (small peak at 9.5mL retention volume). We attribute this high molecular weight tail to a termination reaction by recombination between long chains, provoked by the catalyst solution introduced at the end of our protocol. This high molecular weight tail can have an influence on the mechanical properties of our polymers.

H^1 NMR analysis of the polymer solutions were done on all syntheses realized. Good reproducibility was obtained and the structure of the Poly(BA-co-

6.2. PREPARATION OF SOLVENT-BASED MODEL ACRYLIC POLYMERS 155

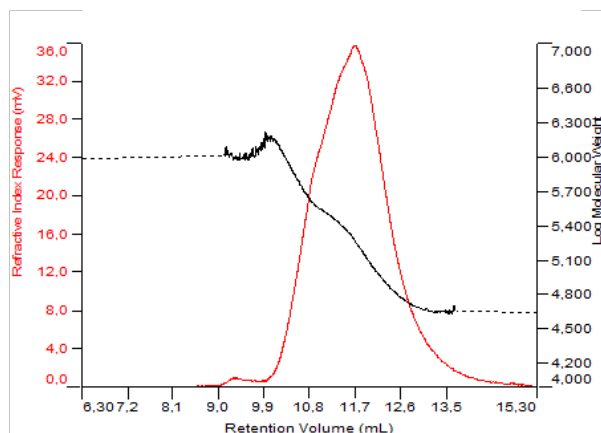


FIGURE 6.2 – Results from GPC : Refractive Index vs Retention Volume (red) and $\text{Log}(M_w)$ vs Retention volume.

AA) was confirmed by the presence of the H from the acid function and the -CH₂ and -CH₃ functions from the butyl acrylate long chain, see Fig 6.3. Moreover, by comparing the integrations of the signals from the acrylic acid protons and the ones from the butyl acrylate protons, we were able to get an estimate of the incorporation of the monomers in the final polymer : 1.7% of AA and 98.3% of BA in molar ratio see Table 6.3. This is quite in good agreement with the 1.9% of AA incorporated, when taking into account the imprecision on the value of the integral of the hydrogen from the AA group.

	BA		AA
M (g/mol)	127.16		72.06
Group	CH ₃	O - CH ₂	COOH
Integral result	1.00	0.68	0.01
Integral per Hydrogen	0.333	0.34	0.05
Molar ratio	97.1%		2.9%
Weight ratio	98.3%		1.7%

TABLE 6.3 – Analysis of the integral of selected signals on NMR spectrums and ratios deducted from the integrals.

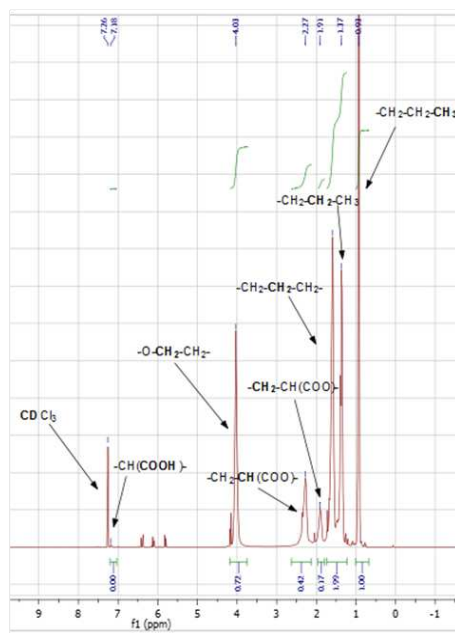


FIGURE 6.3 – H^1 NMR spectrum of Poly(BA-co-AA) obtained by solution polymerization

6.3 Characterization of uncross-linked and cross-linked networks

6.3.1 Corss-linking reaction

Cross-linking reaction versus retarding agent

Aluminium acetylacetonate (AlAcAc) reacts with carboxylic acid functions of the acrylic acid of the Poly(BA-co-AA) by a simple complexation reaction between the ligands and the acid functions (see Fig 6.4). This reaction is quantitative at room temperature and creates 3 enol forms of Acetylacetonate. The enol form of AcAc is in equilibrium with its keto form, see Fig 6.5.

The ligand exchange is possible between the acid protons of the polymer as well as with the AcAc present in the solution under its enol form, see Fig 6.6.

Introducing acetylacetonate in excess in the solution will play two major roles inhibiting the effective cross-linking reaction : it will enter in competition with the carboxylic acid functions of the Poly (BA-co-AA) and when added in excess, will push the equilibrium between AlAcAc and the cross-linked polymer described in the Fig 3 to the reactant side and will block the cross-linking reaction.

As a consequence, as long as the polymer is in presence of both AlAcAc and acetylacetonate, no cross-linking reaction will occur. The elimination of the

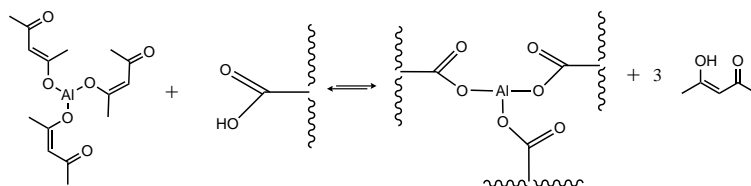


FIGURE 6.4 – Chemical reaction between AlAcAc and carboxylic acid functions of the Poly (BA-co-AA)

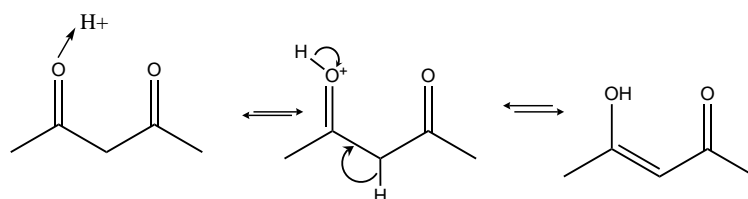


FIGURE 6.5 – Tautomeric equilibrium of Acetylacetone

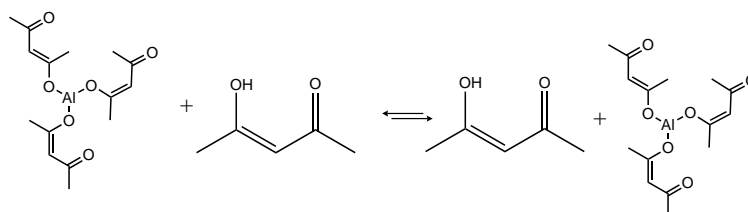


FIGURE 6.6 – Chemical reaction between AlAcAc and carboxylic acid functions of the Poly (BA-co-AA)

acetylacetone by evaporation will however lead to a quantitative cross-linking reaction and the formation of a gel inside the polymer solution.

The role of the retarding agent played by the acetylacetone has been confirmed by a simple test : if the cross-linking solution is prepared with acetylacetate as the sole solvent, a gel is instantaneously obtained when the solution is mixed with the polymer. The introduction of the retarding agent leads to a stable solution which can be kept in a freezer for long periods without any evolution of the system.

Preparation of homogeneously cross-linked films

AlAcAc was dissolved in a solution containing 50 wt% of Acetylacetate (co-solvent) and 50 wt% Acetylacetone (retarding agent) in order to reach 1-2% of cross-linker weight content. The solution was mixed with a given quantity of polymer solution as prepared above in order to reach a cross-linker/polymer

weight content of 0.05% to 1.00% until the solution was homogeneous. The cross-linker/ polymer ratio, noted PX , is then defined as :

$$PX = \frac{m_{AlAcAc}}{m_{P(BA-co-AA)}} \quad (6.1)$$

We also define a molar ratio as :

$$NX = \frac{n_{AlAcAc}}{n_{P(BA-co-AA)}} \quad (6.2)$$

Where n is the number of moles of the constituent in the solution. Finally, we can define the ratio between the cross-linker and the number of potential cross-linking sites on the polymer, *i.e* the number of AA present in the solution divided by 3, as each cross-linker can react with 3 functional sites :

$$NX/AA = \frac{3n_{AlAcAc}}{n_{AA}} \quad (6.3)$$

The equivalence between PX , NX and NX/AA is given in Table 6.4

PX	0.05%	0.1%	0.2%	0.3%	0.4%	1.0%
NX	0.02%	0.04%	0.08%	0.12%	0.15%	0.38%
NX/AA	1.91%	3.8%	7.6%	11.4%	15.2%	38%

TABLE 6.4 – Equivalence between weight ratio and mole ratios for cross-linker ratios used

In order to obtain the relatively thick films ($\approx 500\mu m$) necessary for mechanical characterization, the solution was cast in silicone molds as for latexes (see section 2.4.1 p.61). The samples were left to dry under the hood for 48 hours, covered by a glass cap to limit air flow near the surface. The drying was completed by a final step of one hour in an oven at $80^{\circ}C$ at ambient pressure, followed by 5 minutes under vacuum.

For the adhesive tests, a solution was cast on the glass slides in order to reach a final thickness of $100\mu m$, also following the same protocol as for the latexes (see section 2.5.1 p.64). The solution was carefully deposited with a coating blade adapted to the viscosity of the solution obtained. The glass slides were left to dry under the hood for 48 hours, again covered by a glass cap to limit air flow near the surface. The drying was completed by a final step of one hour in an oven at $80^{\circ}C$ at ambient pressure, followed by 5 minutes under vacuum.

6.3.2 Mechanical characterization

The different polymers obtained were characterized by measuring their gel content and their linear rheological properties.

Gel content

The gel content was measured by weighing a sample of dried cross-linked polymer and putting it in an excess of THF for one week to dissolve all uncross-linked polymer. The swollen insoluble fraction of the polymer was then removed from the solution and dried at room temperature under the hood for 6 hours and then at 80°C under vacuum for 5 minutes. After this step, the sample was weighed. The gel content is defined by the ratio between the weight of the insoluble fraction of the polymer and the initial weight of the polymer :

$$\Phi = \frac{m_f}{m_0} \quad (6.4)$$

Results obtained for different levels of cross-linker with the polymer from the synthesis IV are represented in Fig. 6.7. Other synthesis showed similar results. A fast increase of the gel content can be observed for PX increasing from 0 to 0.4% with a saturation at 80% gel content. We can conclude that some chains remain uncross-linked even when a high quantity of cross-linker is added and migrate in the solvent during the swelling step. This could be due to the nature of the cross-linking agent : the AlAcAc is small and offers three functions. As a consequence, when fixed with a first acid function, it can only create cross-links with neighboring acid functions : as the AA is only present as 3.4 mol%, its presence around other AA groups is limited. Moreover, some smaller chains may have only a few acrylic acid functions that do not react with the cross-linker and as a consequence are not part of the network. As the optimum gel content for a PSA is usually below 30% (Creton, 2003), we can conclude that effective PSAs for our system should have a PX below 0.3%.

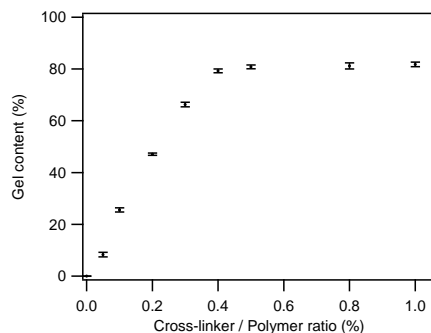


FIGURE 6.7 – Gel content as a function of cross-linker / polymer ratio (PX) for Poly(BA-co-AA)

Small Amplitude Oscillatory Shear rheology

Small Amplitude Oscillatory Shear rheology was realized on a MCR-301 from Anton Paar with a standard parallel plate geometry at 25°C and at frequencies between 0.01 and 50 rad.s⁻¹ on samples with $PX = 0.05\%$, 0.1% , 0.2% and 0.3% .

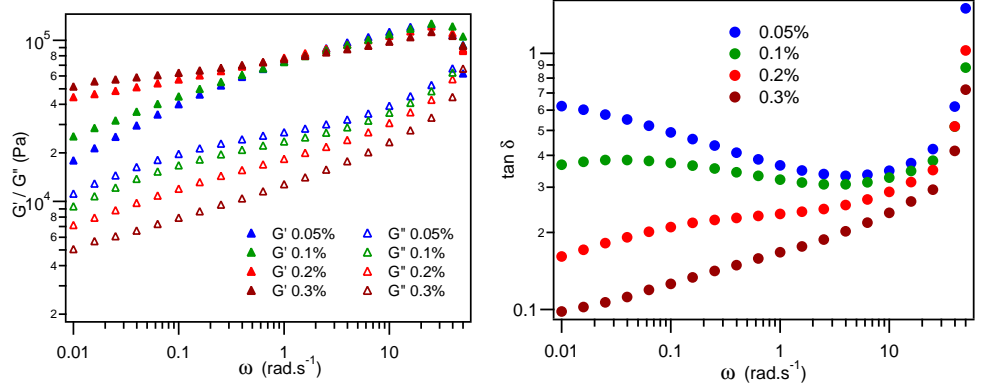


FIGURE 6.8 – G' and G'' (left) and $\tan \delta$ (right) as a function of frequency for $PX=0.05\%$, 0.1% , 0.2% and 0.3% .

The results are shown on Fig. 6.8 : for all cross-linked materials, we observe solid-like behavior, with values of moduli in the same range as for the water-borne materials discussed in the previous sections (see section 2.6.1 p.68). G' is below the Dahlquist criterion of 0.1 MPa (Dahlquist, 1969), confirming that the storage modulus reached with our polymers is in the good range for PSA applications. We observe that the storage modulus G' is quite similar for all materials for frequencies $> 1 \text{ s}^{-1}$. For lower frequencies, G' is only weakly dependent on frequency for high PX , confirming the formation of a network structure, while for $PX=0.05\%$, G' clearly decreases at low frequencies. The loss modulus G'' decreases when PX increases, confirming the transition from a more dissipative to a more elastic system. This result is well shown by plotting $\tan \delta$ as a function of the frequency (Fig. 2.6 right). $\tan \delta$ varies from 0.4 to 0.15 at 1 Hz : since an optimized PSA usually has a $\tan \delta$ around 0.3, we can expect systems with PX at 0.2% or above to be too cross-linked.

6.3.3 Adhesive properties

The adhesive properties were characterized using the probe-tack test already discussed in section 1.4 p.28. Our setup has been described in section 2.5.2, p.65. In this chapter, the probe is always made of polished stainless steel. The approach velocity is $30 \mu\text{m}\cdot\text{s}^{-1}$, the contact time 10 s and the debonding velocity will be maintained at $V_{deb} = 100 \mu\text{m}\cdot\text{s}^{-1}$.

Probe-tack tests were realized for materials with $PX=0\%$, 0.05% , 0.1% , 0.2% , 0.3% and 0.4% and are presented on Fig. 6.9. We can observe a transition in the debonding mechanisms already discussed in section 1.4.2 (p.31 : for the less crosslinked materials, the material deforms by forming fibrils, leading to a high maximal deformation ($PX=0.05\%$ and 0.1%) and then fails cohesively ($PX=0.05\%$) or at the interface ($PX=0.1\%$). At higher PX , the interfacial G_c is not high enough to prevent growth at the interface. The cavities formed in

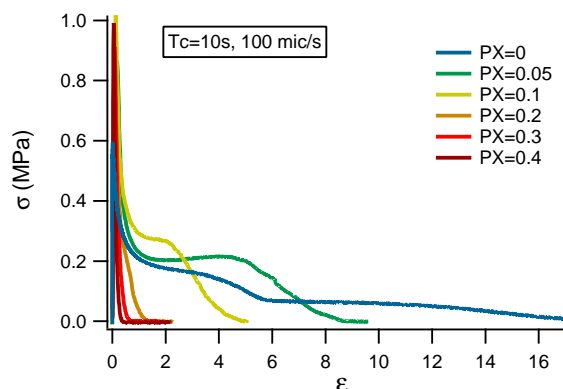


FIGURE 6.9 – Stress-Strain curves of probe-tack tests on model solvent-based Poly(BA-co-AA) with no cross-linker (blue), or cross-linker from PX=0.05 to 0.4. For PX=0 and 0.05 we observe a cohesive failure, while an adhesive failure is observed for all the other materials.

the early stages of the debonding process and the fibrils never form, leading to an interfacial failure after a low level of deformation (PX=0.2-0.4%). At the opposite, a total absence of cross-linker (PX=0%) leads to a characteristic double plateau curve with soft fibrils that break cohesively after a very high elongation ($\epsilon_{max} = 17$).

The system used show a clear transition from interfacial crack propagation (PX > 0.1%) to bulk deformation. This bulk deformation will occur if $\tan \delta / G > 0.45 \cdot 10^{-5} Pa$, which is in quite good agreement with the value of Deplace (2008) of $0.5 \cdot 10^{-5} Pa$ determined for nano-structured cross-linked acrylic PSAs. The boundary determined in Chapter 2 (inferior to $0.1 \cdot 10^{-5} Pa$ for SS) seems to correspond to uncross-linked systems, confirming that this criterion varies if the system is cross-linked or not.

6.4 Making films with a continuous gradient in viscoelastic properties

As discussed in the introduction, our goal is to make films with a continuous gradient in viscoelastic properties along their thickness. We have shown in the previous section that we were able to obtain very different behaviors by controlling the cross-linking ratio in the matrix. Thus, our strategy here will be to introduce cross-linker in excess on one side of the material and let it diffuse to the other side. A front of diffusion will be created. If the diffusion is well controlled, we should obtain systems highly cross-linked on one side and weakly cross-linked on the other one. Our goal here is to investigate the effect of such a gradient in viscoelastic properties on the adhesive properties of the film relative

to the properties of the homogeneous film.

6.4.1 Modus operandi to obtain films with continuous gradients

In order to obtain a film with a continuous gradient, the initial strategy we had thought of, was to prepare one layer containing the cross-linker and put it on top of a layer without cross-linker as presented in Fig 6.10.

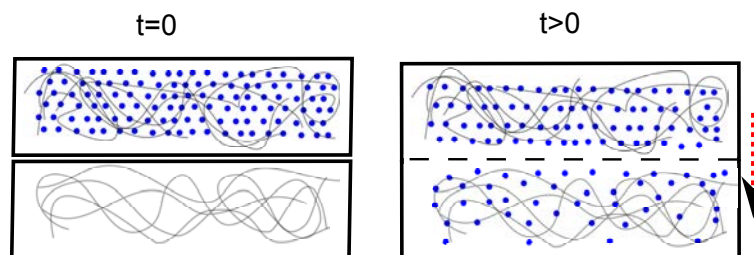


FIGURE 6.10 – Method used to obtain continuous gradient : at $t=0$, a layer containing cross-linker is put in contact with a layer without cross-linker. The diffusion of the cross-linker leads to a gradient in its concentration, which will create a gradient in viscoelastic properties

The difficulties encountered to define this protocol were that the excess of solvent needs to be eliminated to obtain solid films, while the retarding agent should not evaporate to avoid cross-linking. Moreover, a too high evaporation rate will lead to the formation of bubbles, leading to craters on the surface of the material. We therefore had to adjust this initial strategy and the successful protocol is given below :

1. Prepare two layers of adhesives with a thickness of $100 \mu m$, one containing a retarding agent but no cross-linker (layer A) one containing cross-linker at 0.3% and retarding agent (layer B). The layer which will be in contact with the substrate is coated on a silicone coated release paper, the other on a glass slide.
2. Evaporate the most volatile solvent : leave the films at room temperature for 3 hours under the hood while being covered by a cap to slow down the evaporation rate.
3. Put the two layers on top of each other (if the solvents have not been evaporated in the previous step, the system is too liquid to put two layers on top of each other).
4. Let the mobile components diffuse for a given time while avoiding any evaporation of the retarding agent : in order to achieve that, the films were put in a dessiccator under acetylacetone vapor.
5. Remove the film from the dessiccator and finish the drying in order to evaporate the remaining solvent and the retarding agent by leaving the

6.5. ADHESIVE PROPERTIES OF A FILMS WITH A CONTINUOUS GRADIENT IN VISCOELASTIC PROPERTIES

films under the hood at room temperature for 5 minutes, then at 80°C for 10 minutes, and finish with 2 mins at 80°C under vacuum.

To work at a diffusion time equal to zero, step (4) is omitted.

6.5 Adhesive properties of a films with a continuous gradient in viscoelastic properties

Several methods to measure the cross-linking profile of our layers were explored without success (AFM and Solid NMR particularly), as the difficult drying process and the adhesive properties of the sample limited the available techniques. Thus, it was decided to directly test its adhesion properties to evaluate the properties of the two faces of the film prepared.

In order to characterize the adhesive films obtained with this continuous gradient method, each system was made twice (see Fig. 6.11) :

- one with the layer A (containing initially no cross-linker) on a removable silicone-coated paper in order to be in contact with the substrate during adhesion tests,
- one with this layer A on the glass slide, letting the initially saturated layer B in contact with the substrate during adhesion tests.

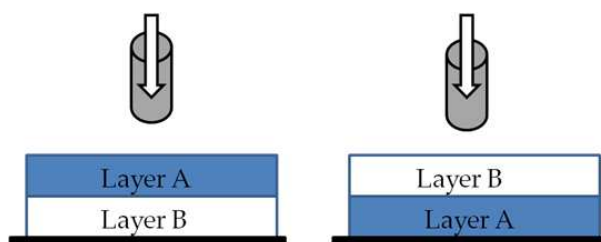


FIGURE 6.11 – Sketch of both systems made for each diffusion time : Layer A and Layer B are inverted, letting the possibility to characterize both sides of the system by adhesion tests.

By using this strategy, we were able to characterize the general behavior on both sides. The characterization used was the classical probe-tack test already described in section 6.3.3 with a probe velocity of $100 \mu\text{m}\cdot\text{s}^{-1}$ for each test. An example is given in Fig. 6.12 where a system containing 0.3% of AlAcAc in layer B initially was characterized on both sides without diffusion step. In this case this is equivalent to testing a bi-layer as in chapter 5. We clearly see that when the probe comes in contact with the side containing the cross-linker, the measured stress-strain curve is identical to that obtained with a homogeneous layer containing 0.3% cross-linker. The cross-linker is clearly in excess in layer B, as the material shows an elastic behavior with interfacial crack propagation. On the other hand when the probe comes in contact with layer A, the stress-strain curve is similar to what would have been obtained with 0% cross-linker with a

very high elongation at break and a cohesive failure. This experiment shows that the cross-linker reacted fast enough to observe any significant diffusion between layer A and B during the drying step.

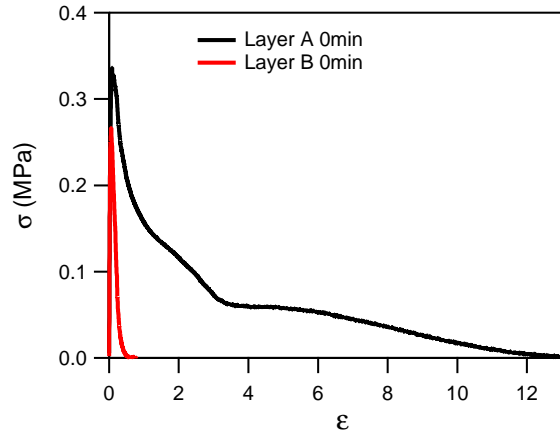


FIGURE 6.12 – Stress-Strain curves for a system without diffusion, $V_{deb} = 100 \mu m.s^{-1}$. The black curve shows the test done with the probe in contact with the surface without AlAcAc (layer A) while the red curve shows the test done with the probe in contact with the surface containing an excess of AlAcAc (layer B).

Using exactly the same protocol, the system was now annealed for a diffusion step of 30 minutes before letting it dry and cross-link. The resulting probe tack curves are shown in Fig. 6.13. We see a clear change in the experiment where the probe contacts layer A that contained no cross-linker initially. This time, the stress-strain curve shows a debonding mechanism with only a limited dissipation before debonding. This is a proof that the cross-linker has migrated from layer B to layer A, leading to a partially cross-linked system. When the probe was put in contact with the other side, layer B, which contained initially 0.3% of cross-linker, the debonding remained elastic like, but with an increased dissipation. This was probably due to a decrease in the cross-link density on this side. These results indicate that the diffusion protocol is working. But the diffusion time is too long, leading to a material that is too elastic on both sides to adhere well on stainless steel.

Another way to present the results is to show the curves at 30 minutes where layer A is in contact with the probe or layer B is in contact with the probe, see Fig. 6.14. The two curves show only small differences, indicating a nearly homogeneous layer. The elastic behavior of both layers seems to indicate that PX is superior at 0.1% at both interfaces.

The idea is thus to reduce the diffusion time to 15 minutes. Results for $t=0min$, $t=15min$ and $t=30min$ are shown in Fig. 6.15 : in this case, we obtain a maximal dissipation with a high plateau and an adhesive failure (near the

6.5. ADHESIVE PROPERTIES OF A FILMS WITH A CONTINUOUS GRADIENT IN VISCOELASTIC PROPERTIES

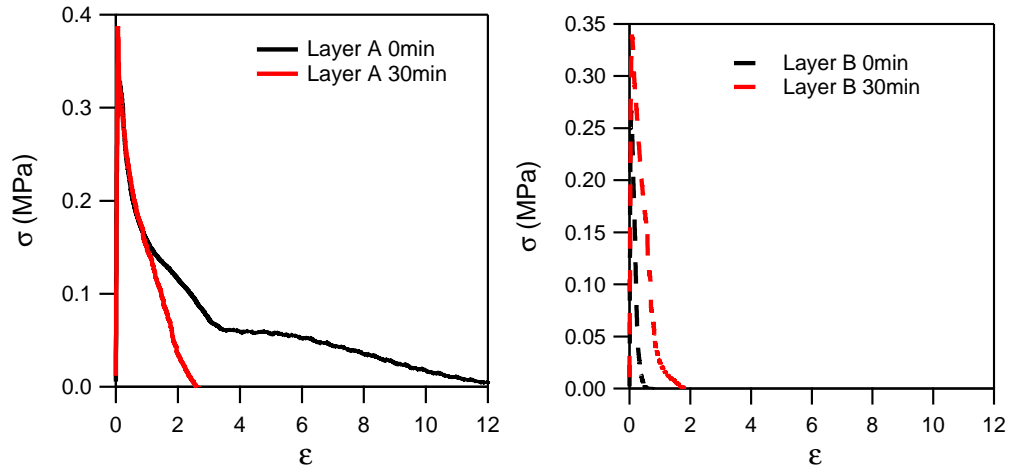


FIGURE 6.13 – Stress-Strain curves ($V_{deb} = 100 \mu m.s^{-1}$) on surface of layer A (left) and B (right) with no diffusion time and a diffusion time of 30 minutes.

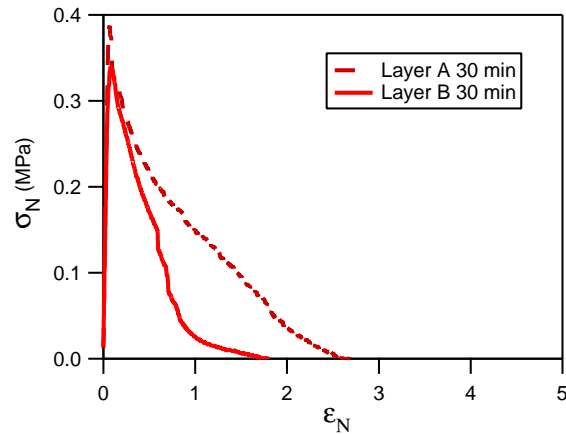


FIGURE 6.14 – Stress-Strain curves ($V_{deb} = 100 \mu m.s^{-1}$) on surface of layer A and B for a diffusion time of 30 minutes

adhesive/cohesive transition) when layer A is in contact with the probe, while as expected, a level of dissipation in between the case with no diffusion and the case with a diffusion time of 30 minutes is found when layer B is in contact. We observe that the maximal elongation is quite high ($\epsilon_{max} \sim 10$), leading to the assumption that PX is inferior to <0.05 at the interface, see Fig. ?? discussed for homogeneous materials.

As we did for 30 minutes, we can plot the two curves of the stress-strain curves obtained on each interface for a diffusion time of 15 minutes, see Fig.

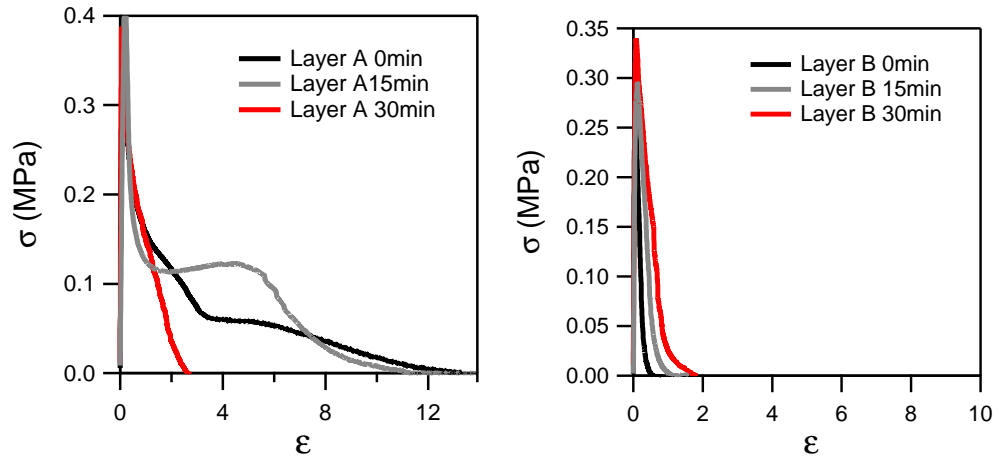


FIGURE 6.15 – Stress-Strain curves ($V_{deb} = 100 \mu m.s^{-1}$) on surface of layer A (left) and B (right) with no diffusion time and a diffusion time of 15 or 30 minutes.

6.16. We clearly see the heterogeneity of the system with two interfaces of our materials showing different adhesion energy and debonding mechanisms.

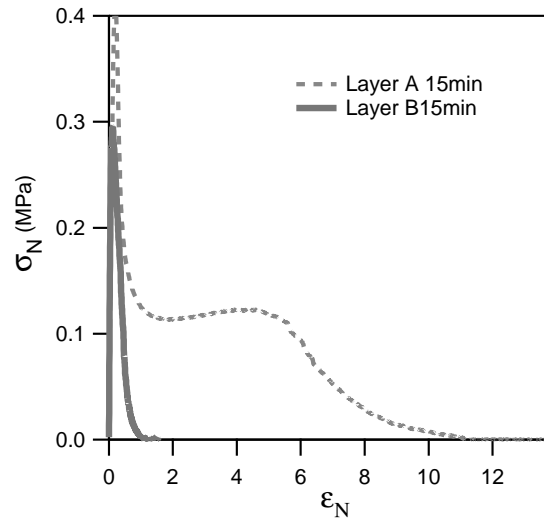


FIGURE 6.16 – Stress-Strain curves ($V_{deb} = 100 \mu m.s^{-1}$) on surface of layer A and B for a diffusion time of 30 minutes

In summary, by letting our cross-linker diffuse for 15 minutes, we were able

to design an adhesive layer with a continuous gradient in properties. This "optimized" adhesive behaves like a highly elastic adhesive if it is adhered to the probe on its B side but behaves more like a PSA, with a significant fibrillar structure and adhesive debonding when it is adhered (and debonded) from the A side.

6.6 Diffusion theory applied to our system

Our system can be approximated by a cell full of a diffusive component diffusing into an empty cell at t_0 . Fig. 6.17 represents the situation.

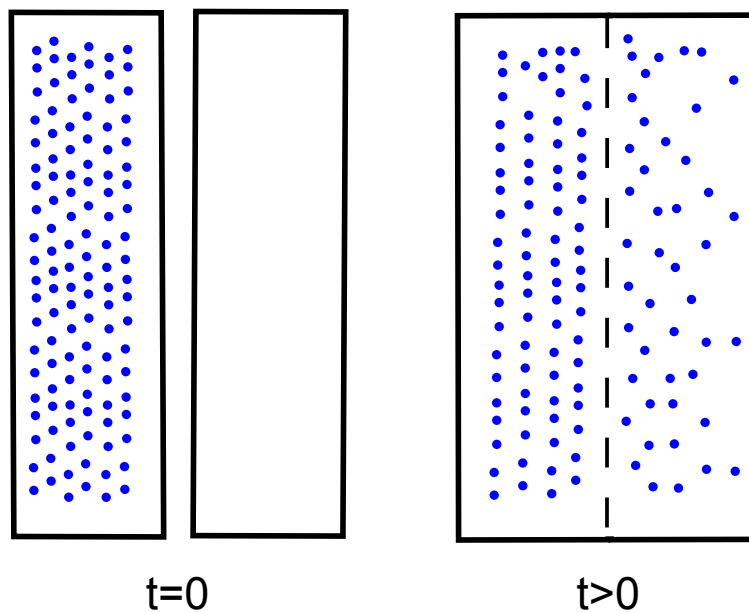


FIGURE 6.17 – Diffusion occurring between the layer A and the layer B. At t_0 , the left layer contains C_0 diffusing molecule and the right layer none.

As our film of adhesive is very long and wide compared to the thickness $\tilde{\Delta}x$, we will consider our problem as 1D-diffusion problem along the thickness of the layer. To characterize quantitatively the diffusion phenomena, we can use Fick's law in 1 dimension :

$$\frac{\partial C}{\partial t} = D \frac{\partial^2 C}{\partial x^2} \quad (6.5)$$

where D is the diffusion coefficient in cm^2/s and C is the concentration in diffusive component (in our case the cross-linker AlAcAc). Our system is composed of the two cells joined together. We will note " x " the thickness in mm, $x = 0$ being the limit between the two layers. As the two layers have a

thickness of 0.1 mm, $x = -0.1$ is the left boundary and $x = 0.1$ is the right boundary. The initial conditions are :

$$C(x \in [-0.1 : 0], t_0) = C_0 \quad \text{and} \quad C(x \in [-0.1 : 0], t_0) = 0. \quad (6.6)$$

We are in a case of closed boundaries, so we will use the Neumann boundary conditions : the derivative is null at the boundaries (Press et al., 2007). As a consequence, the boundary conditions are :

$$C(x = -0.1, t) = C(x = -0.1 + dx, t) \quad \text{and} \quad C(x = 0.1, t) = C(x = 0.1 - dx, t). \quad (6.7)$$

This equation is a partial differential equation that can be solved using a finite differences method. In order to do that, we can mesh time and thickness by defining an interval dx and dt . Then we define "r" the ratio :

$$r = D \frac{dt}{dx^2} \quad (6.8)$$

we calculate $c(x, t + dt)$ by using :

$$dc(x, t + dt) = x(x + dx, t) + c(x - dx, t) - 2c(x, t) \quad (6.9)$$

$$icoc(x, t + dt) = c(x, t) + r dc(x, t + dt) \quad (6.10)$$

For our calculations, we will take

- $C_0=0.3\text{wt}\%$,
- $M=160000$,
- $N=2000$,

where M is the number of meshes in space, N the number of meshes in time..

The last parameter to evaluate is the diffusion coefficient D . D is not known in the literature for AlAcAc in Poly(Ba-co-AA), but we can estimate D knowing that :

- at 30 minutes, the material will have an elastic behavior on both sides
- at 15 min, the gradient is such that dissipation is high at the interface with layer A.

Using the mechanical characterization done on homogeneous materials, we can make the hypothesis that :

- $PX > 0.1$ everywhere in the material at $t=30$ minutes
- $PX < 0.05$ at $x = 0.1$ at $t=15$ minutes

The resulting coefficient leading to these results is $D = 3.0 \cdot 10^{-8} \text{cm}^2/\text{s}$. Interestingly, this diffusion coefficient is of the same order of magnitude as diffusion coefficients of small organic molecules in Polyethyl Methacrylate available in the literature (Crank and Park, 1978).

Simulations done with $D = 3.0 \cdot 10^{-8} \text{cm}^2/\text{s}$ are given in Fig. 6.18. At t_0 , the layer A ($x > 0$) is full of cross-linker while the layer B is empty. As time goes on, the cross-linker diffuses from the left to the right, until equilibrium is reached, where the wt% in AlAcAc is 0.15% in all the material. We can calculate that

the right boundary has reached 95% of the maximal value 0.15% after 71 min. Results at 15min and 30 min are logically in agreement with the hypothesis we did just above.

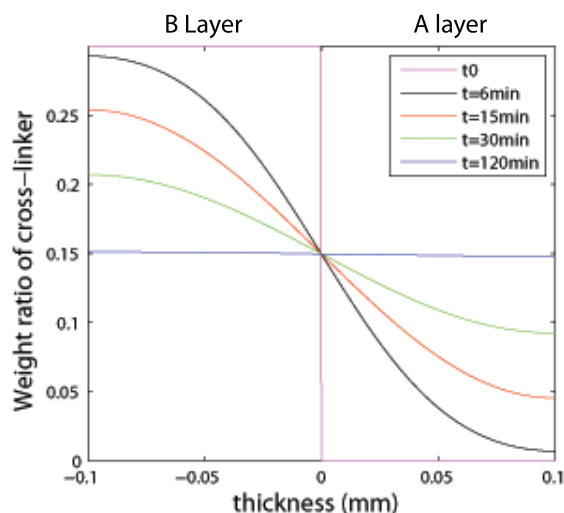


FIGURE 6.18 – Concentration profile along the thickness at $t=0$, 6min, 15min, 30min and 120 min.

At $t=15$ min, the cross-linker is logically less present in layer B, with ~ 0.05 wt% at the free surface of layer B, in agreement with what was targeted.

Using a coefficient of diffusion of our simulation $D = 3.0 \cdot 10^{-8} \text{ cm}^2/\text{sn}$ explains well the differences observed between experiments for a diffusion time of $t=15$ min and $t=30$ min. If our diffusion coefficient is correct, a diffusion time > 70 min should show no difference between the behavior of the layer A and the layer B.

6.7 Conclusion

In this chapter, we have shown how to synthesize random copolymers of poly(BA-co-AA) by solution polymerization, and have characterized the molecular weight distribution and monomer composition of the resulting polymers. Adhesive films were made cross-linked or uncross-linked. The cross-linking reaction selected is a complexation between AlAcAc and the acid functions of the polymer chain which can be controlled by the presence of a retarding agent AcAc. We developed the equilibrium in play between the polymer, the cross-linker and the retarding agent. These films were characterized to get information on their structure, their mechanical and adhesive properties. We then used this cross-linking system to make adhesive layers with a continuous gradient in viscoelastic properties along their thickness and showed the influence of the

presence of such a gradient on their adhesive properties. As we showed in Chapter 5, a new range of properties can be obtained with these gradient materials, with a high viscoelastic dissipation at the interface between the adhesive and the adherend combined with a high mechanical resistance closer to the backing. Furthermore only one starting concentration and two diffusion times were used in these preliminary experiments but a more systematic study could be carried out with a similar chemistry to optimize the properties. Similarly to the bi-layer systems investigated in Chapter 5, an improvement in the shear properties could also be expected from these gradient adhesives but a more systematic study is clearly necessary to confirm the results obtained. The simple 1-D diffusion model developed in the last section is consistent with the adhesive properties observed experimentally if one assumes a diffusion coefficient $D = 3.0 \cdot 10^{-8} \text{cm}^2/\text{s}$. This diffusion coefficient could be experimentally determined by fitting this model with experimental data if a way to directly measure the concentration of cross-linker as a function of position was available. Other systems, easier to use, may be considered to make adhesives with a gradient in viscoelasticity. In this chapter, the reaction was activated by the elimination of a retarding agent. A cross-linking reaction activated by temperature could alternatively be used in the same way, or even more practically a UV polymerization using a UV cross-linker. With a well tuned UV intensity and cross-linker concentration, the absorption of UV from the material could lead to a gradient in cross-link density even for a homogeneous composition in cross-linker, but the theoretical study of these phenomena would be difficult.

Bibliographie

- Crank, J. and Park, G. (1978). *Diffusion in Polymers*. Academic Press.
- Creton, C. (2003). Pressure-sensitive adhesives : an introductory course. *MRS bulletin*, 28(6) :434–439.
- Dahlquist, C. (1969). *Pressure-sensitive adhesives*. Marcel Dekker : New York.
- Deplace, F. (2008). *Waterborne nanostructured Adhesives*. PhD thesis, Université Pierre et Marie Curie.
- Press, W. H., Teukolsky, S. A., Vetterling, W. T., and Flannery, B. P. (2007). *Numerical Recipes, The Art of Scientific Computing*. Cambridge University Press, New York.
- Tobing, S. D. and Klein, A. (2001). Molecular parameters and their relation to the adhesive performance of acrylic pressure-sensitive adhesives. *Journal of Applied Polymer Science*, 79(7) :2230–2244.

Chapitre 7

General Conclusion and Outlook

In this thesis we have studied model acrylic polymers for Pressure Sensitive Adhesives applications. We first characterized in detail the model acrylic polymers that have been designed to represent PSA covering a wide range of viscoelastic properties, from viscoelastic liquids to soft viscoelastic solids. A rate-dependent hardening when compared to linear viscosity was observed for all materials, which can be explained by the presence of acrylic acid co-monomers interacting with each other and acting as stickers and felt only at high strain rates. Thus, two dynamics control the mechanical response of this material : the entangled polymer network dynamics and the sticker dynamics. Adhesive properties of the materials were studied with a probe-tack test over a range of debonding rates and with two probes showing different interfacial interactions. This led us to observe the three characteristic debonding mechanisms of PSAs. Using the experiments on PE, we were able to characterize the transition occurring at small strain between interfacial crack propagation and bulk deformation, determined by a value of $\tan \delta(\omega)/G(\omega) = 0.35 \cdot 10^5 Pa^{-1}$. At larger strains, we were also able to characterize the transition between adhesive failure (of the fibrils at the interface) or cohesive failure (failure of the fibrils in the bulk). On stainless steel this transition was observed at a high enough strain rate for all materials except one, while nearly all materials showed an adhesive debonding on PE. This transition which is inherently due to the strain hardening cannot be predicted easily by the linear viscoelastic properties. In cross-linked PSAs the ratio C_{soft}/C_{hard} discriminates between soft viscoelastic solids, cannot be used for materials showing no hardening compared to Neo-Hookean behavior since C_{hard} as defined by Deplace et al. is effectively zero.

We then carried a systematic quantitative analysis of probe-tack experiments on three of our model materials showing different viscoelastic behaviors. The kinematics of the deformation of the cavities formed during the debonding were characterized by image analysis. The average shape of the cavities nucleating

during debonding and the total projected area of the cavities in the plane of the adhesive film were characterized quantitatively. An estimate of the local tensile strain in the plane of observation showed that the local tensile strain systematically exceeded the nominal strain and diverged for the lowest molecular weight (leading to cohesive debonding) and the most elastic adhesive (leading to interfacial failure by crack propagation) and was only stable for the intermediate adhesive showing the best PSA properties. The kinematic information was used to determine an effective stress in the adhesive layer, by deducting the contributions of pressure due to the void in cavities and normalizing by the area of material instead of the total area including cavities. This effective stress shows a clear different trend whether the material forms stable fibrils or crack propagation at the interface. These results show that small differences in rheological and mechanical properties lead to significant changes in the kinematics of deformation, which then has a great influence on the work of adhesion. This coupling between rheological properties and kinematics is a great challenge for modeling soft materials and we hope that our results will be the base of comparison with simulations of computational fluid mechanics using realistic material properties.

We also developed a two-mode Phan-Thien and Tanner model and wrote it explicitly for uniaxial deformation, to fit an extensional rheology curve or a tensile test, the latter requiring the Hencky strain rate to vary over time. This model proved to fit well all our materials for the two types of uniaxial experiments. The two modes have been clearly linked to two separate dynamic processes of our materials observed in the mechanical characterization of these materials and studied in more details in our EU project MODIFY. Using the parameters obtained from the fits, we were able to simulate tensile tests over a wide range of strain rates not accessible by experiments. This allowed us to calculate C_{soft} and C_{LS} parameters, the former describing the strain dependent softening of the material relative to the neo-Hookean prediction at a given strain rate, the latter being a high strain residual modulus of the material at a given strain rate. A value of $C_{soft}/C_{LS} = 2.36$ clearly separates adhesive and cohesive failure observed in tack experiments. When the value is higher, the material is not elastic enough, leading to cohesive failure. When $C_{soft}/C_{LS} < 2.36$, the debonding is adhesive. This criterion should stay viable for weakly cross-linked PSAs such as industrial ones. The model developed offers perspectives to simply characterize soft viscoelastic adhesives in uniaxial deformations and could help chemists to have a feed-back on the properties of their materials. We encourage the use of this model to other PSAs or other similar highly viscoelastic soft materials.

We then studied two ways to introduce a gradient in viscoelastic properties along the thickness of an adhesive. We first explored in a systematic way how a layering of the adhesive can influence its debonding mechanisms (adhesive or cohesive) and modify its adhesion energy. The effect of the layering demonstrates that even the debonding mechanism of a very soft adhesive such as a PSA is always very heterogeneous spatially with most of the dissipation occurring near the interface with the adherend. Using model materials at our disposal, we were able to explore two ways of improvement. On weakly adhering surfaces such as

Polyethylene, we increased the dissipation of the layer in direct contact with the adherend, while keeping a material of higher molecular weight further away from the interface. The result obtained was a beneficial shift to lower debonding velocities when the transition from cohesive to adhesive debonding was observed. On high adhesion surface such as stainless steel, we introduced a lower molecular weight layer as a backing and let a more elastic layer at the interface. The viscous backing layer increased the deformability leading in our case to an increase of the adhesion energy by 20-30%. The influence of the thickness of the layers was studied and showed that its consequence on the debonding mode was quite limited. This can lead to interesting applications, as the control of the thickness of a bi-layer system can control the deformation of the system without impacting too much the debonding mechanism. Although we performed these experiments with model materials, we feel that the concept should work with commercial weakly cross-linked PSA. Finally, we synthesized acrylic polymers in solvent in order to introduce a continuous gradient in viscoelastic properties along the thickness of the material. In order to obtain this innovative material, we let a cross-linker diffuse from a concentrated layer to a layer without cross-linker. The cross-linking, activated by the evaporation of a retardant, led to materials showing the targeted gradient. This result was confirmed by probe-tack experiments on both surfaces of the adhesive and backed-up by a modeling of the diffusion of the cross-linker in the layer. Only one starting concentration and two diffusion times could be tested in these preliminary experiments but a more systematic study could be carried out with a similar chemistry to optimize the properties and gather more information of the benefits of a continuous gradient versus a multi-layer system. The diffusion coefficient could be experimentally determined by fitting this model with experimental data if a way to characterize the concentration of the cross-linker is found. Direct characterization detecting the Aluminium of the cross-linker or indirect characterization measuring the viscosity along the thickness such as solid-state NMR could be used. Nevertheless, the adhesive nature of the material and the very sensitive drying process to obtain this material limits the use of these techniques. Other systems, easier to use, may be used to make adhesives with a gradient in viscoelasticity. A cross-linking reaction activated by temperature could alternatively be used in the same way, or even more practically a UV polymerization using a UV cross-linker. With a well tuned UV intensity and cross-linker concentration, the absorption of UV from the material could lead to a gradient in thickness even for a homogeneous composition in cross-linker, but the theoretical study of these phenomena and their modeling would be difficult.

Chapitre 8

Résumé Long en Français

Introduction

Les Adhésifs Sensibles à la Pression sont des films fins qui adhèrent à un substrat en appliquant une légère pression et peuvent idéalement se détacher du substrat sans laisser de résidus. Ces adhésifs ont un rôle important dans notre vie, puisqu'on les trouve dans les rubans adhésifs, les étiquettes autocollantes, les pansements ou les fameux Post-It. Une bonne adhésion est obtenue avec des matériaux à la fois liquides qui forment facilement un contact moléculaire, et élastiques pour résister à la contrainte. C'est pourquoi les adhésifs sont typiquement à base de polymères : un réseau de points de réticulation empêche les chaînes polymères de s'écouler et est responsable du caractère solide des matériaux. Les monomères composant les chaînes polymères sont eux très mobiles et ont toutes les caractéristiques d'un liquide. Un bon adhésif doit donc montrer à la fois les propriétés d'un solide et celles d'un liquide : l'équilibre entre ces deux propriétés est essentiel.

Selon le matériau utilisé, le mécanisme de décollement variera. Lors de l'initiation du décollement, des cavités se forment à l'interface. Si le matériau est très élastique, ces cavités se propageront le long de l'interface substrat/adhésif, conduisant à un décollement interfacial (mécanisme I). Si le matériau peut dissiper assez d'énergie, ces cavités grandiront perpendiculairement à l'interface, formant de longs fibrilles caractéristiques de ce type d'adhésifs. Si le matériau est trop liquide, la rupture sera localisée dans l'épaisseur de l'adhésif (au centre des fibrilles), conduisant à un décollement adhésif (mécanisme II). Si le matériau est bien optimisé, les fibrilles se détacheront de l'interface conduisant à une rupture adhésive (mécanisme III).

Dans cette thèse, nous nous intéressons à la transition entre ces mécanismes à partir de matériaux modèles synthétisés par un partenaire au sein d'un projet européen MODIFY. Par ailleurs, les transitions entre ces mécanismes sont dépendantes des propriétés du matériau à l'interface et dans son épaisseur. En introduisant un gradient de propriétés viscoélastiques le long de l'épaisseur de

l'adhésif, nous montrons qu'il est possible de contrôler la transition entre ces mécanismes, en adaptant notre stratégie à différents substrats.

Lors du premier chapitre, un état de l'art de la physique et de la chimie des adhésifs sensibles à la pression ainsi que des modèles qui peuvent être utilisés pour modéliser des matériaux viscoélastiques. Le deuxième chapitre décrit les matériaux modèles utilisés, notamment leurs propriétés mécaniques à haute déformation et leurs propriétés adhésives. Le troisième chapitre présente des expériences de probe-tack synchronisées avec un système de capture d'image de haute performance qui permet d'obtenir des mesures quantitatives sur l'aire totale projetée, la forme des cavités et leur vitesse de croissance. Ces mesures permettent notamment de remonter à une contrainte vraie lors de ces expériences que l'on peut comparer à des tests classiques de traction uniaxiale. Dans le quatrième chapitre, nous présentons un modèle à 2 modes dérivés du modèle de Phan-Thien et Tanner (PTT). Une discussion est présentée sur les aspects mathématiques de ce modèle. Un fit entre ce modèle et des expériences de déformation uniaxiale est réalisé, ce qui nous permet ensuite de réaliser des simulations sur de larges gammes de vitesse pour cinq matériaux différents. La transition entre les mécanismes de décollement adhésif et cohésif peut ainsi être prédite via des paramètres obtenus par ces simulations. Dans le chapitre 5, nous nous intéressons à une stratégie pour réaliser des adhésifs bi-couches avec une variation de viscoélasticité entre ces deux couches et montrons que nous pouvons modifier le mécanisme de décollement via ce système. Enfin, le chapitre 6 présente une méthode innovante pour réaliser des adhésifs à gradient de viscoélasticité, en utilisant un front de diffusion d'un réticulant dans la matrice polymère dans l'épaisseur.

Matériaux modèles

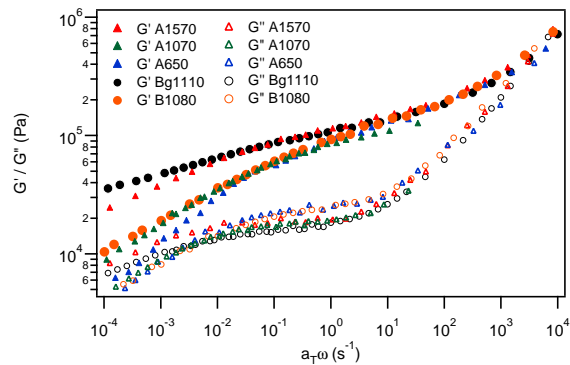


FIGURE 8.1 – Mastercurves of dynamic storage (G') and loss (G'') modulus as function of angular frequency ($a_T\omega$) for the five different materials at a reference temperature of $30^\circ C$.

Les matériaux utilisés dans cette thèse sont des PSA modèles constitués de latex préparés par polymérisation en émulsion, non réticulés pour l'essentiels d'entre eux, et qui sont des copolymères statistiques comprenant 98,1 % de N-butyl-acrylate et 1,9 % d'acide acrylique. Ces matériaux ont été synthétisés par Dow Corning avec des caractéristiques moléculaires variables.

Une caractérisation globale de la rhéologie des matériaux a été effectuée en obtenant les courbes maitresses des 5 matériaux étudiés à $30^{\circ}C$, voir voir Fig. ??.

Les tests de traction sont réalisés sur des éprouvettes rectangulaires d'environ $500 \mu m$ d'épaisseur et 5 mm de largeur. Ils sont placés entre les mors d'une machine de traction INSTRON 5565 éloignés de 15 mm. Des marques blanches permettent de mesurer la longueur initiale et la déformation via un extensomètre vidéo. Les tests de traction sont effectués à différentes vitesses de déformation initiales ($0.1 s^{-1}$ et $1 s^{-1}$), à température ambiante. Les résultats sont présentés Fig. ??.

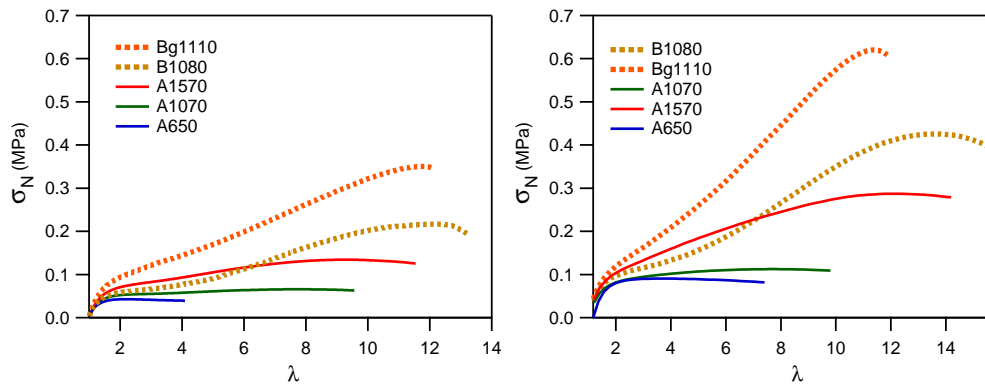


FIGURE 8.2 – Nominal Stress versus λ for the five different materials, at $\dot{\lambda} = 0.1 s^{-1}$ (left) and $\dot{\lambda} = 1.0 s^{-1}$ (right).

Les matériaux synthétisés présentent ainsi des comportements variés allant de liquides viscoélastiques à des solides viscoélastiques.

Les propriétés adhésives des films de latex sont évaluées à travers un test de probe-tack. Dans ce test, un poinçon est approché à vitesse constante lame de verre sur laquelle est séchée le film adhésif. Le poinçon est approché jusqu'à entrer en contact avec le film adhésif, avec une force déterminée ainsi qu'un temps de contact fixe. contrôlés. Le poinçon est ensuite décollé à vitesse constante. La force nécessaire au décollage du poinçon et le déplacement de celui-ci sont enregistrés.

Les matériaux utilisés permettent de décrire tous les types de décollage, comme le montrent les courbes obtenues, cf Fig. ?? avec une vitesse de décollage de $100 \mu m.s^{-1}$: les courbes présentées montrent un décollage interfacial (Bg1110), des décollages adhésifs (A1570 et B1080) et des décollages co-

hésifs (A1070 et A650).

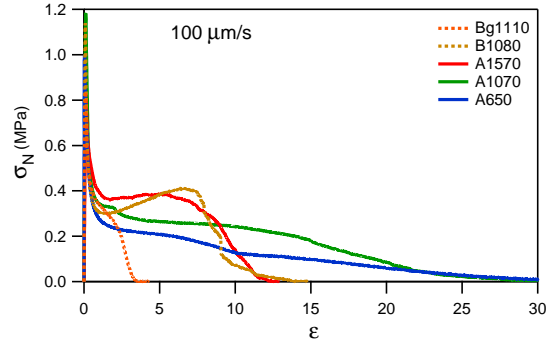


FIGURE 8.3 – Stress-Strain tack curves for the five different materials at debonding velocity of $100\mu\text{m/s}$ against a stainless steel probe.

En analysant les résultats obtenus, nous remarquons que la transition entre le décollement interfacial ou la déformation dans l'épaisseur peuvent être prédites par un critère précédemment développé au laboratoire, $\tan \delta/G'$. Dans notre cas, une valeur de $0.35 \cdot 10^{-5} \text{Pa}^{-1}$ est discriminante et semble être caractéristique de polymères non réticulés.

Analyse de la Croissance des Cavités à l'interface

Grâce à un système de probe-tack synchronisé avec un système de capture d'image de haute performance, nous avons pu obtenir des mesures quantitatives sur l'aire totale projetée, la forme des cavités et leur vitesse de croissance. Les images obtenues lors des expériences de probe-tack sont traitées numériquement, permettant d'obtenir la surface couverte par les bulles dans un plan, et donc leur croissance avec le temps. Un exemple d'image traitée est présentée Fig. ??.

Grâce à ces analyses, nous avons notamment pu remonter à la surface réellement occupée par le matériau, et ainsi obtenir une contrainte effective en divisant la force de traction, une fois la contribution de la pression atmosphérique déduite, par l'aire effective. Nous pouvons ainsi comparer cette contrainte vraie à celle obtenue lors d'un test de traction uniaxiale, comme montré Fig. ??.

Cette figure nous montre que le profil de cette contrainte effective diffère selon la nature du matériau. Pour les deux matériaux non réticulés (A650 et A1070), la contrainte effective chute après un pic alors qu'elle continue de croître après une inflexion pour le matériau réticulé (Bg1110). Cette différence conduit à des mécanismes de décollement totalement différents comme il a été présenté plus tôt.

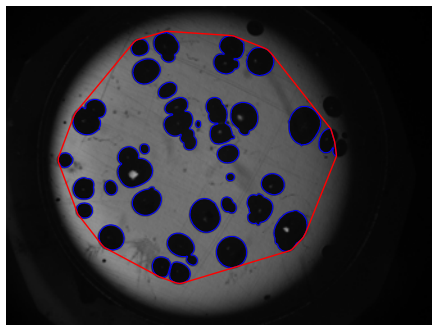


FIGURE 8.4 – Convex envelope of the region occupied by cavities (red solid line) with area A_c . Cavities with area smaller than the threshold $\epsilon_A = 50$ pixels are not taken into account. Also cavities nucleated at the border of the illuminated region are discarded because they lie outside the area our algorithm set as safe region for detection.

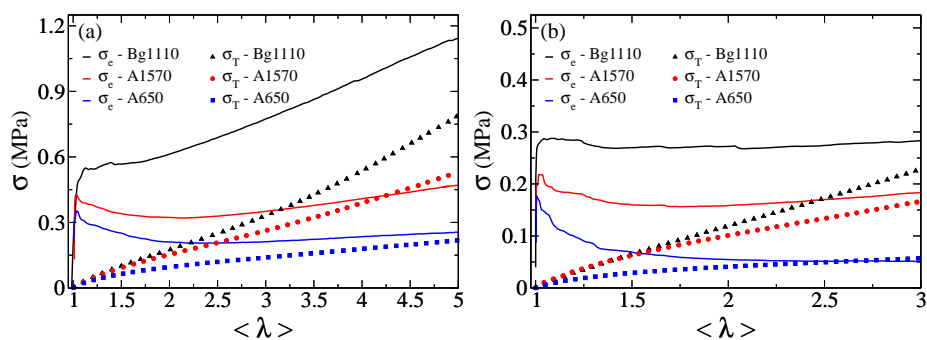


FIGURE 8.5 – Effective σ_e and true tensile σ_T stresses for the three materials at a pulling velocity of $10 \mu\text{m s}^{-1}$ (a) and $1 \mu\text{m s}^{-1}$ (b).

Modélisation de Matériaux Viscoélastiques utilisés en tant que PSA

Les matériaux utilisés possèdent une dynamique lors de la déformation complexe, laissant apparaître deux dynamiques possédant des temps de relaxation différents, l'une pouvant être associée aux enchevêtrements, l'autre à des stickers formés par les groupes acide acrylique. Nous avons développé un modèle à deux modes dérivé du modèle PTT pour fitter les données obtenues par traction uniaxiale, que ce soit par rhéologie élongationnelle (taux de déformation de Hencky constant) ou par traction (taux de déformation Hencky non constant). Les résultats pour un des matériaux est présenté Fig. ??.

A partir des paramètres obtenus par ces fits, nous avons simulé des tests de

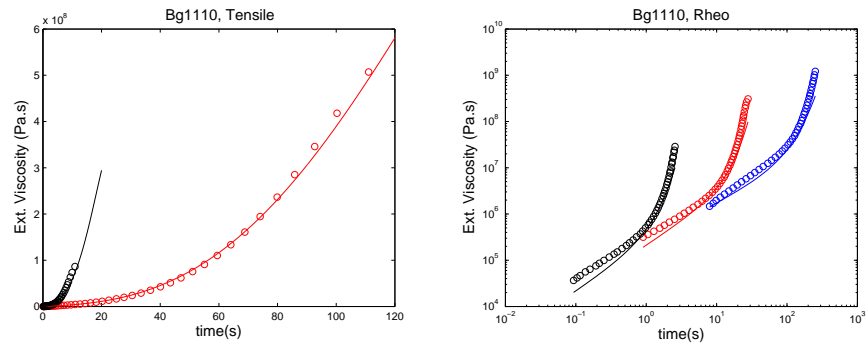


FIGURE 8.6 – Experimental curves (dots) obtained by fitting the PTT-2modes model with experimental results from tensile tests and extensional rheology.

traction pour quatre vitesses de déformation différentes, certaines étant non accessibles par des tests réels (vitesse non accessible par les machines). A partir de ces courbes, nous avons extrait un paramètre caractéristique de l'adoucissement du matériau, C_{soft} ainsi qu'un paramètre qui caractérise la contrainte à haute déformation, C_{LS} . Le ratio entre ces deux paramètres permet de discriminer de manière extrêmement effective un décollement adhésif d'un décollement cohésif et pourrait donc être utilisé pour prédire le décollement de PSA et ainsi aider à leur formulation par des chimistes ou des industriels.

Adhésifs Multi-Couches

Afin de contrôler les mécanismes de décollement, nous avons réalisé des systèmes bi-couches à partir des matériaux utilisés auparavant. Sur des surface à faible énergie comme le polyéthylène, le matériau doit être très liquide à l'interface pour mouiller le substrat et permettre une déformation dans l'épaisseur. Mais si le matériau est trop liquide, on obtient une rupture cohésive. En associant une couche liquide à l'interface et une couche plus élastique au-dessus, nous avons pu obtenir un décollement adhésif tout en obtenant une dissipation d'énergie élevée, comme le montre la figure ??

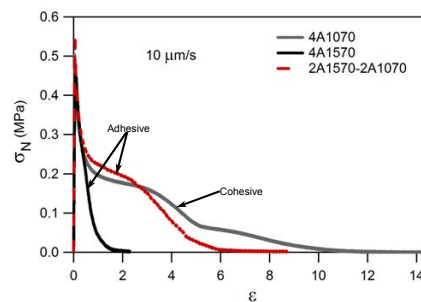


FIGURE 8.7 – Stress-strain curves for 2A1570-2A1070, 4A1570 and 4A1070. The probe used is polyethylene, $V_{deb} = 10\mu m.s^{-1}$.

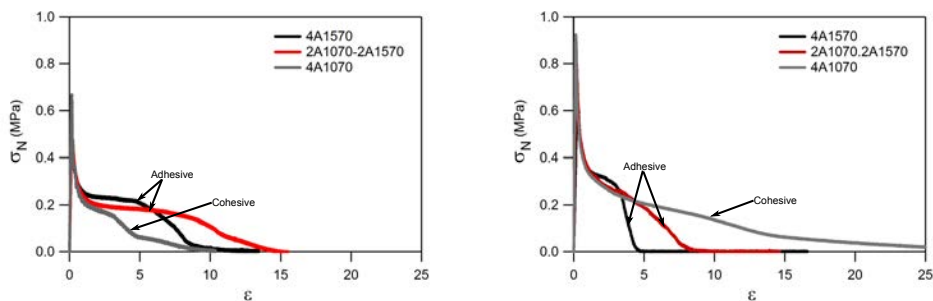


FIGURE 8.8 – Stress-strain curves for 2A1070-2A1570, 4A1570 and 4A1070. The probe used is stainless steel. Left : $V_{deb} = 10\mu m.s^{-1}$, right : $V_{deb} = 100\mu m.s^{-1}$

Sur une surface à énergie haute comme l'acier inox, la difficulté n'est cette fois pas d'obtenir une déformation dans le volume, l'interaction avec le substrat étant forte. Néanmoins, cette forte interaction conduit facilement à un décollement cohésif. Dans ce cas, nous avons utilisé un système où un matériau élastique à l'interface est associé à un matériau dissipatif à l'interface. Dans ce cas, nous augmentons la dissipation lors du mécanisme de décollement en comparaison à

un système homogène élastique, et nous obtenons un décollement adhésif, voir Fig. ??.

PSA à gradient continu

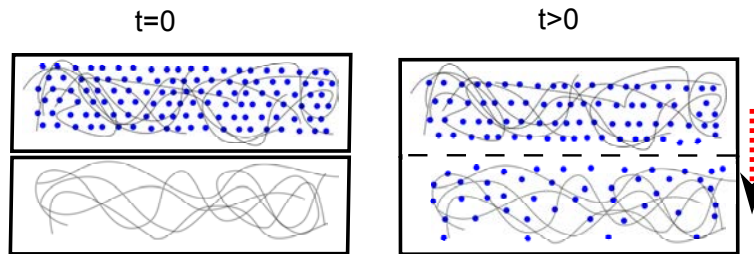


FIGURE 8.9 – Method used to obtain continuous gradient : at $t=0$, a layer containing cross-linker is put in contact with a layer without cross-linker. The diffusion of the cross-linker leads to a gradient in its concentration, which will create a gradient in viscoelastic properties

Finalement, nous avons synthétisé et caractérisé un PSA par polymérisation en solution pour obtenir un polymère sans structuration interne, au contraire des latex utilisés précédemment. Ensuite, via un protocole développé au laboratoire, nous avons introduit un gradient continu dans les propriétés viscoélastiques du matériau en introduisant une couche contenant un réticulant au contact d'une couche n'en contenant pas, voir Fig. ??.

Au contact l'une de l'autre, le gradient diffuse, introduisant un profil de concentration le long de l'épaisseur. Nous avons caractérisé les deux surfaces de ces systèmes et montré qu'un gradient avait été introduit et que le temps de diffusion contrôlait finement ce profil. Dans notre cas, un temps de diffusion de trente minutes conduit à un système quasi homogène en termes de propriétés adhésives, alors qu'un temps de diffusion de 15 minutes permet d'obtenir des propriétés proches des systèmes discutés dans le chapitre précédent.

Nous avons appliqué la théorie de la diffusion au système utilisé : un coefficient de diffusion de $3.10^{-8} \text{cm}^2/\text{s}$ permet d'expliquer les résultats obtenus, ce qui est en accord avec un coefficient de diffusion d'une molécule organique dans une matrice acrylique selon la littérature.

Lors du décollement d'un adhésif mou (tels que les adhésifs sensibles à la pression, dits PSA), des mécanismes complexes entrent en jeu à l'interface et dans l'épaisseur du film d'adhésif. Afin d'optimiser ces adhésifs, il convient de maîtriser les transitions entre les différents modes de décollement. Nous avons étudié ces transitions grâce à des matériaux modèles. Nous avons réalisé une analyse quantitative d'expériences de décollement, en nous appuyant notamment sur une nouvelle technique d'analyse d'image. Nous avons également modélisé le comportement mécanique de nos matériaux en traction uniaxiale grâce à un modèle viscoélastique de Phan-Thien et Tanner (PTT) à deux modes. Ces études ont montré la forte hétérogénéité des mécanismes de décollement où des processus à l'interface et dans l'épaisseur de l'adhésif sont en compétition. Pour obtenir des PSA plus efficaces, nous avons donc optimisé leurs propriétés en introduisant un gradient dans les propriétés viscoélastiques du film selon leur épaisseur. Des systèmes bi-couches optimisés montrent d'intéressantes propriétés, sur surface de forte ou de faible adhésion. Enfin, des adhésifs à gradient continu ont été réalisés et caractérisés via la diffusion d'un réticulant dans un film de polymère puis activation à un instant précis de la réaction de réticulation.

Mots clés : PSA, viscoélasticité, gradient, multi-couches, polyacrylate de butyle, propriétés mécaniques, rhéologie

During the debonding of a soft adhesive (as are Pressure Sensitive Adhesives or PSA), complex mechanisms enter in competition at the interface and in the bulk of the adhesive film. In order to optimize these adhesives, it is crucial to understand the transitions between the different debonding modes. We studied these transitions using model materials and carried out a quantitative analysis of debonding experiments with a new image analysis method. We also modeled the mechanical behavior of our materials under uniaxial deformation by using a 2-modes Phan-Thien and Tanner (PTT) viscoelastic model. These studies showed the strong heterogeneity of the debonding mechanisms where process at the interface and in the bulk are in competition. To obtain more efficient PSA, we optimized their properties by introducing a gradient in the viscoelastic properties of the film along their thickness. Bi-layer optimized systems showed interesting properties on surfaces with high or low adhesion. Finally, adhesives with a continuous gradient were realized and characterized by the diffusion of a cross-linker in a polymer film followed by an activation of the cross-linking reaction at a given time.

Keywords : PSA, viscoelasticity, gradient, multi-layers, poly(butyl acrylate), mechanical properties, rheology